Making Better Batteries
Following Electrochemistry at the Nano Scale with Electron Microscopy

Basak, Shibabrata

Important note
To cite this publication, please use the final published version (if applicable).
Please check the document version above.

Making Better Batteries:
Following Electrochemistry at the Nano Scale
with Electron Microscopy

Shibabrata Basak

Making Better Batteries: Following Electrochemistry at the Nano Scale with Electron Microscopy

Proefschrift

ter verkrijging van de graad van doctor
aan de Technische Universiteit Delft,
op gezag van de Rector Magnificus prof.ir. K.C.A.M. Luyben;
voorzitter van het College voor Promoties,
in het openbaar te verdedigen op
woensdag 26 april 2017 om 12:30 uur

door

Shibabrata BASAK

Master of Technology in Solid State Technology, Indian Institute of Technology Kharagpur,
India

Geboren te Kolkata, India

This dissertation has been approved by the promotor:

Prof.dr. H.W. Zandbergen

Composition of the doctoral committee:

Rector Magnificus Prof.dr.	Chairman
H.W. Zandbergen	Delft University of Technology, promotor

Independent members:

Prof.dr. E. Olsson	Chalmers University of Technology, Sweden
Prof.dr. J. Mayer	RWTH Aachen University & Ernst Ruska-Center Jülich, Germany
Prof.dr. M. Huijben	University of Twente, The Netherlands
Prof.dr. B. Dam	Delft University of Technology
Prof. P. French	Delft University of Technology
Dr. E.M. Kelder	Delft University of Technology

An electronic version of this dissertation is available at: http://repository.tudelft.nl

To Sarmila

CONTENTS

Chapter 5: Unveiling Mechanisms Of Li-O$_2$ Batteries Using TEM Grids

Chapter 6: Fabrication Of MEMS Devices For Operando TEM Experiments

Chapter 7: Improving Thin Film Batteries Using *In situ* TEM Studies

CHAPTER 1

INTRODUCTION TO BATTERY TECHNOLOGY

In this introductory chapter, first the basics of battery operation are discussed in a brief. This followed by brief glance into the state-of-the-art battery technologies; the main challenges are also briefly discussed. At the end of this chapter, the goal of this dissertation and the structure of the thesis are presented.

1. Energy and us

Starting from heating, cooling or lighting our houses, to operate our household appliances, powering computers, mobile phones and other electronic gadgets, driving cars and moving cargo, to manufacture the products we need in our daily lives: All these functions require energy. Energy has become an indispensable part of our lives.

1.1. Global warming vs. conventional and renewable energy

Most of the energy we use in our daily lives comes from burning coal or fossil fuel [1,2]. The downside of these energy sources is that they produce greenhouse gases [3]. The growing amount of greenhouse gases in the atmosphere is increasing the earth's absorption of the sun's radiation, which is raising the temperature of our atmosphere [4]. The melting of glacial ice mass clearly demonstrates the impact of rising temperatures around the world [5]. If the global temperature continues to rise, glaciers will melt faster, which in turn will raise sea levels. This will obviously be a devastating development, especially for coastal regions [5], not to mention the adverse health issues due to heightened air pollution levels [6].

At the 2015 Paris climate conference (COP21), 188 countries agreed on a global action plan to avoid dangerous climate changes by limiting global warming to well below 2°C above pre-industrial levels. This includes a reduction in greenhouse gases, increased use of renewable energy sources, and improved energy efficiency. By 2030, the European Union has committed to reducing greenhouse gas emissions by 40% (compared to 1990), increasing its use of renewable energy sources by at least 27% and improving energy efficiency by at least 27% [7].

Wind, solar and hydropower are the three main sources of renewable energy. These resources can provide energy with zero or nearly zero emissions of air pollutants and greenhouse gases. One drawback of renewable energy is that its supply is time-dependent. For example, solar energy can clearly only be harvested during the daytime, and wind energy obviously depends on sufficiently strong air currents. To meet minimum grid-level energy supplies, storage capabilities are essential [8–10].

Vehicles are one of the major sources of air pollution, especially in developed countries. For example, the U.S. transportation sector produces about 26% of that country's climate-changing emissions [11]. Globally, about 14% of

manmade carbon dioxide comes from cars, trucks, airplanes, ships and other vehicles [3]. As passenger vehicles become more numerous throughout the world, pollution will increase dramatically unless emission-reduction measures are put in place.

1.2. Batteries and us

Battery powered energy grids can improve utilization of renewable energy sources [8–10]. And the battery-powered all-electric vehicles powered with energy from renewable energy sources will enable truly green transport.

Batteries have already played a crucial role in the revolution of portable electronics over the past two decades. Increasing use of portable electronic devices like mobile phones, laptops, cameras in our daily life sought for better batteries. Batteries are not only used in electronic appliances but also in healthcare devices such as pacemakers. Further the performance of battery will play a vital role determining the success of the upcoming wearable circuits, which can be utilized in remote healthcare monitoring.

So, overall the need for long lasting, better performing and low cost batteries is truly evident.

2. Basics of Batteries

An electrochemical cell is a device that stores electricity in the form of chemical energy. To meet the voltage or current demands for a specific application, these cells are connected in series or parallel: series connection multiplies the voltage, whereas parallel connection multiplies the current. An array of one or more electrochemical cell(s) is called a battery [12,13].

In batteries, two different materials of different positive standard reduction potential function as electrodes, separated by an electrolyte. Electrolyte is an ionic conductor in aqueous, aprotic or solid form that allows ions but not electrons to be transported. The electrodes are connected to current collectors, thus allowing electrical input/output from the battery. Figure 1 schematically represents a simple electrochemical cell.

All the components of a battery should be abundant in nature, i.e. inexpensive, and environmentally friendly, i.e. non-toxic and non-hazardous. Furthermore, ideal cathode and anode materials should have the following characteristics: (a) high capacity, (b) high potential difference, which is set by the cathode–anode

combination, (c) good ionic and electronic conductivity to allow fast (de)insertion of ions during (dis)charge, and (d) structural and chemical stability in combination with the electrolyte for stability.
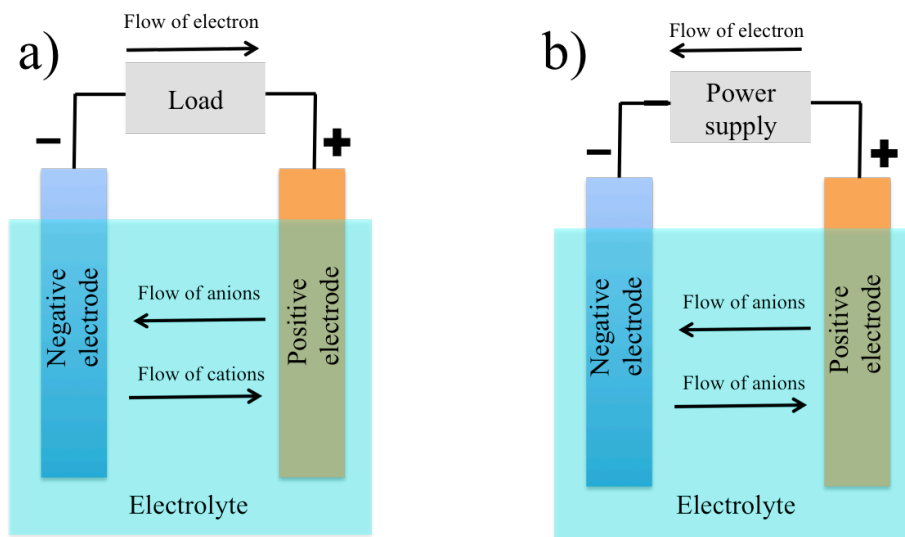
Figure 1: *Electrochemical operation of a battery (a) discharge, (b) charge.*[i]

Electrolytes should possess the following features: (a) good ionic but no electronic conductivity, (b) a wide potential window to allow electrochemical (dis)charge without degrading the electrolyte, (c) high thermal stability to prevent degrading the electrolyte in case of increased battery temperature during fast (dis)charge, and (c) nonreactivity towards the anode, cathode, separator and current collectors to prevent corrosion.

Current collectors should (a) be corrosion-resistant, (b) electrochemically stable at the working potential of the electrodes, and (c) have good adhesion properties between the electrode composite and current collectors.

2.1. Battery timeline

In 1800, Italian physicist Alessandro Volta invented the first true battery, the voltaic pile, consisting of pairs of copper and zinc disks stacked on top of each other, separated by a layer of cloth or cardboard soaked in brine, which acted as the electrolyte. Volta's battery was a primary battery. In 1804, German physicist Johann W. Ritter invented the first rechargeable battery. However, at

---

[i] *As batteries supply electrical energy during discharge, the negative electrode is often known as an anode and the positive electrode as a cathode.*

that time there was no means of recharging batteries until the generator was invented. In 1859, French inventor Gaston Planté constructed the first practical rechargeable lead acid battery, which is still used today in automobiles. Figure 2 illustrates the main events in the development of batteries.
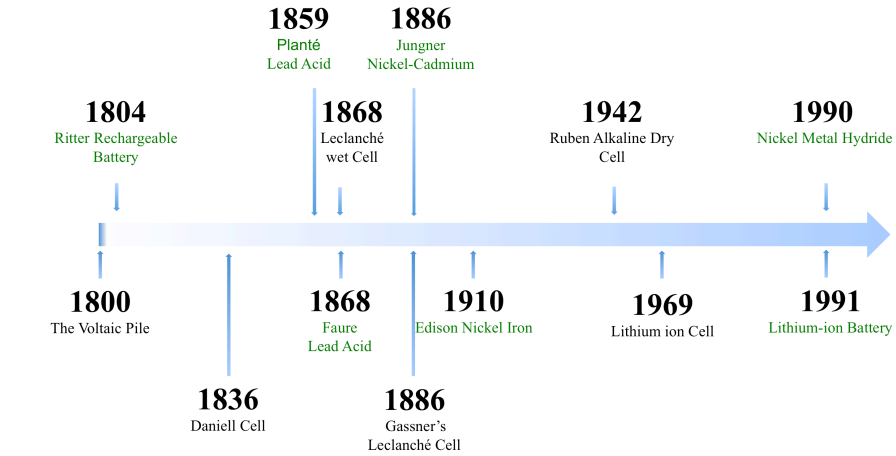
Figure 2: *Timeline of the key events in battery development, adopted from* [14] *. Green denotes rechargeable batteries.*

2.2. Thermodynamics and kinetics

The theoretical standard cell voltage (E^0), which is referred to as an open circuit or equilibrium or working potential of a cell, is defined as

$$E^0 = E^0 \text{ (cathode)} - E^0 \text{ (anode)} . \tag{1.1}$$

The Nernst equation further relates the cell potential to the standard potential and to the activities (often approximated by concentrations) of the chemical species undergoing reduction and oxidation.

In an ideal battery, all of the free energy converts to electrical energy as the battery is discharged. However in a practical battery, when current is drawn, the actual operating voltage is lower than suggested by thermodynamics because kinetic limitation of reactions and other processes must occur in order to produce a current flow during operation.

There are three different kinds of polarizations that affect kinetics: (1) activation polarization (η_a), (2) ohmic polarization or IR drop (η_o) and (3) concentration polarization (η_c). Activation polarization is related to the kinetics of the charge-transfer reactions taking place at both electrode (anode and

cathode) electrolyte interfaces. Ohmic polarization is interconnected to the resistance of individual cell components and contact resistance between the cell components. Concentration polarization is due to mass transport limitations during cell operation. Therefore the terminal voltage (E_T) with current flowing is

$$E_T = E_{OCV} - (\eta_a + \eta_o + \eta_c) = E_{OCV} - \eta, \tag{1.2}$$

where, E_{OCV} is the cell voltage at open circuit. Figure 3 schematically shows the effect of different polarizations.
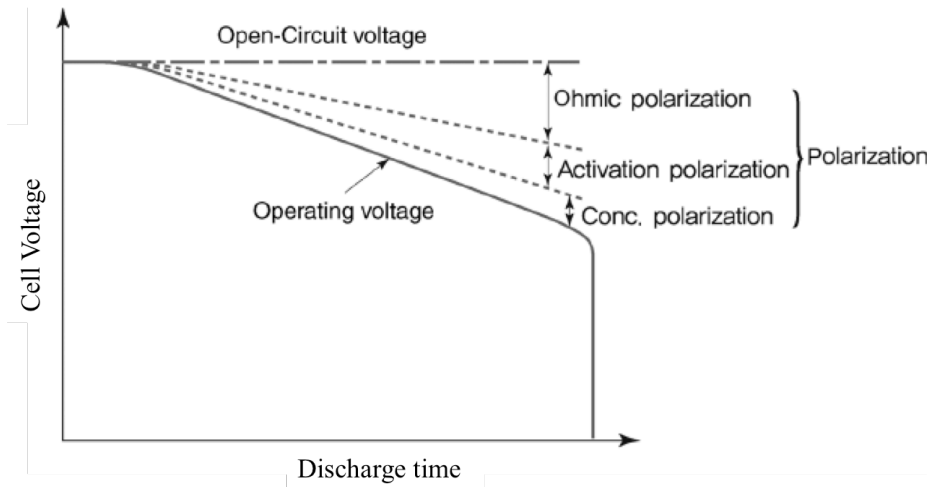
Figure 3: Typical discharge curve of a battery showing the effect of different polarizations, adopted from [15].

A low activation polarization is achieved by a high exchange current density in a battery, which is directly related to the reaction-rate constant, activities of reactants and products, or the potential drop across the electrode–electrolyte double layer. A low ohmic polarization is achieved by high electronic and ionic conducting electrodes, high ionic conducting electrolytes, and good interconnections between the current collector electrodes, electrode–electrolyte. Fast flows of mass from the electrode surfaces reduce the concentration polarization. Porous electrodes that allow better interconnectivity between the electrode and electrolyte ensure fast mass transport, thus reducing the concentration polarization [15]. Owing to the presence of polarization, the discharge voltage of a battery is less than predicted by thermodynamics; the difference is called discharge overpotential. The charging potential is higher than predicted by thermodynamics; the difference is called charge overpotential.

3. State-of-the-art battery technologies

Generally speaking, a battery should have a high specific capacity, which allows a high amount of charge to be delivered per unit of mass. This enables us to use smaller and more lightweight batteries for any given application. Furthermore, it is essential for a rechargeable battery that the specific capacity be maintained over several battery cycles. Some applications, such as electric vehicles, require high power density and thus high voltage output combined with high current output (fast discharge).

Of the battery technologies available today, lithium-ion batteries have the best energy and power density along with the best volumetric energy density, which makes them the most suitable batteries for electric vehicles and portable electronics [16]. A few other battery technologies, namely Li-air and Li-sulfur batteries, have the potential to deliver much higher capacities than today's Li-ion batteries, so they have of course attracted tremendous research attention [17,18]. On the other hand, owing to the greater abundance of sodium compared to lithium, a fair amount of research is also being done on Na-ion, Na-air and Na-sulfur batteries [19–21].

Gravimetric energy density (Wh/Kg)
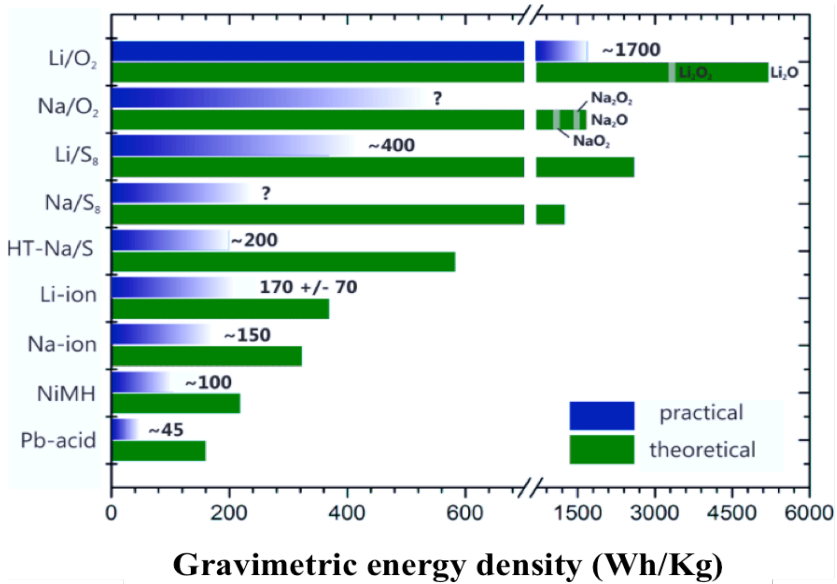
Figure 4: Comparison of battery technologies with respect to their energy densities, reproduced from [22].

To put this into perspective, Figure 4 shows a comparison of different state-of-the-art battery technologies with respect to their theoretical and (estimated) practical energy densities: Pb-acid, NiMH (nickel metal hydride), HT-Na/S_8

(high-temperature Na-sulfur), Li-ion, Li-S_8 (Li-sulfur), Li/O_2 (Li-air battery[ii]), Na-ion (Na-ion), Na-S_8 (Na-sulfur), Na/O_2 (Na-air battery[ii]). The practical energy density values for Pb-acid, NiMH, HT-Na/S_8 and Li-ion batteries are taken from commercial batteries. The energy density values of Li-S_8, Li/O_2 are taken from Ref. [22]. The values for Na-ion Na-S_8, Na/O_2 are estimated using the data from their lithium battery counterpart.

In addition to Li-ion batteries, this thesis will examine Li-O_2, Li-sulfur and Na-ion batteries. The basics of these batteries are discussed briefly in the following sections.

3.1. Lithium-ion battery

In 1991, Sony introduced the first "lithium-ion battery" with graphite as anode and lithium cobalt oxide as cathode [16]. The work of Sony triggered worldwide interest in lithium-ion batteries. Currently, several billions of units are produced every year by various battery manufacturers. These batteries power various portable electronics devices such as cellular mobile phones, notebooks, camcorders, and MP3 players. Figure 5 shows schematically the basic working principle of a lithium-ion battery.
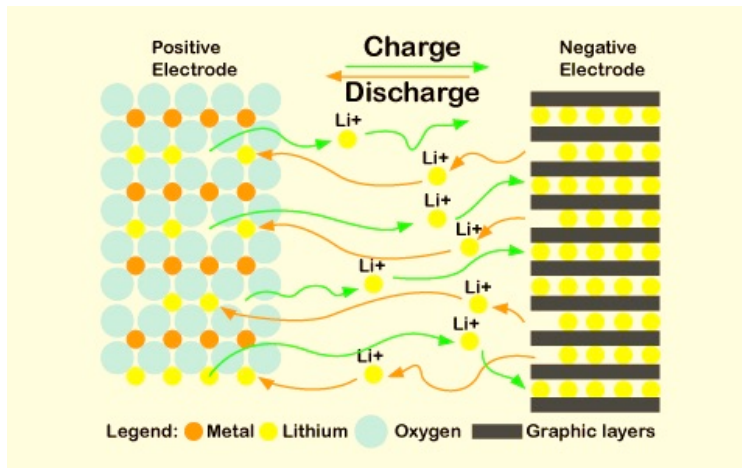
Figure 5*: In a Li-ion battery during charging, Li-ions travel from the cathode through the electrolyte and reach the negative electrode, where they are intercalated into the graphite structure. To compensate for the transfer of the ionic charges, electrons are also exchanged between the two electrodes via an external circuit. During discharge, lithium ions and electrons travel in opposite directions while performing the desired electrical work.*

[ii] *The current Li-air and Na-air battery uses pure oxygen and the performance degrade drastically in presence of other air component especially CO_2, moisture. Thus Li-air and Na-air batteries should more appropriately be termed as Li-O_2 and Na-O_2 and will be used from hereon.*

There is continuous pressure on the portable electronics industry to develop and produce ever more mobile devices, and there is equal pressure on the electric vehicle sector to develop improved lithium-ion batteries. This has resulted in extensive R&D activities on academic and industrial levels to find better cathodes, anodes and electrolytes, as well as optimizing the current materials to utilized their full potentials. Appendix A gives insight to the cathode, anode and electrolytes generally used in Li-ion battery.

3.2. Na-ion battery

Global lithium resources are estimated at 30–40 metric tons, which may prove to be insufficient to meet future demands of energy storage, especially considering a lithium recycling rate of less than 1%.

On the other hand, sodium (Na) is one of the most abundant elements in the earth's crust ($\approx$2.6%) and available in virtually unlimited amounts in seawater. The large ionic size of Na (1.02 Å) and its low standard electrochemical potential ($\approx$2.71 V vs. Na^+/Na) compared with those of Li (0.76 Å and 3.04 V vs. Li^+/Li, respectively) result in low power and energy densities. Thus, even though Na intercalation compounds were first explored in the 1980s, only a handful of studies were conducted between then and 2010, owing to the tremendous success of lithium-ion batteries [23]. Today, the increasing demand for electrochemical energy sources has prompted renewed interest in room-temperature Na-ion batteries.

The working principle of Na-ion batteries is similar to that of Li-ion batteries. The required quality of their electrodes and electrolytes is also similar. Thus, layered and polyanionic compounds have been investigated extensively as cathode materials, and carbon-based materials, metal-oxide compounds, and metals have been studied as anode materials. Some of these materials are already displaying significant capacities and recyclability [19]. Nevertheless, Na-ion battery technology is still in its infancy, and further research is required before it can be commercialized. In the course of this thesis research, we have studied ~20 nm spherical nanoparticles as anode for Na-ion battery.

3.3. Li-S batteries

As next-generation energy storage materials, lithium-sulfur (Li-S) batteries have become increasingly attractive, owing to their high gravimetric density (2600 Whkg^{-1}) and specific capacity (1670 mAhg^{-1}). In addition, sulfur is a highly cost-effective and environmentally benign element. In a typical non-

aqueous Li-S battery, sulfur mixed with carbon additives forms the cathode, and lithium metal is used as the anode [18].

The study of Li-S batteries dates back more than thirty years with the discovery of organic polar aprotic solutions in which lithium polysulfide redox reactions are reversible. However, the overall performance of current Li-S batteries is impeded by the inherently poor electronic and ionic conductivity of sulfur and the dissolution of higher-order polysulfide phases (Li_2S_n, where $8 \geq n \geq 2$) during cycling, which cause irreversible loss of active material [24]. Additionally, the fundamental problem of dendritic growth of lithium during battery cycling must be addressed for reasons of safety and battery lifetime.

One way to reduce the dissolution of higher-order polysulfide phases is to use an ionic liquid electrolyte, where the polysulfide phases are less soluble than organic electrolytes [18]. Another option is to design the composite cathode in a manner that reduces the dissolution of the polysulfide phases. Various innovative strategies are currently under development.

In the course of this thesis research, we have prepared binder-free 3-D vertically aligned few-layered graphene (FLG) electrodes filled with partially reduced graphene oxide-sulfur nanocomposites (PrGO/S) for high performance Li-S batteries.

Dendritic growth of lithium can be approached using a ceramic membrane following the lithium anode or by using pre-lithiated silicon instead of lithium metal as the anode [18].

3.4. Li-O$_2$ batteries

Li-O$_2$ batteries show great potential for vehicular applications because they provide the highest theoretical energy density (3500 Wh/kg) of all current battery technologies [25]. Although it was first studied as early as 1978, Li-O$_2$ battery technology has only made huge strides in the past five years. A typical Li-O$_2$ battery consists of a metal-lithium anode, electrolytes and porous carbon support with or without catalyst particles. During discharge, Li-ions from lithium metal travel via the electrolyte and react with the incoming oxygen to form discharge products on a porous carbon support, which acts as the cathode. This *in situ* formation of the cathode as the battery discharges is the main difference between Li-O$_2$ batteries and those in which the cathode is already present before the battery cycling. Depending upon the type of electrolyte used, Li-O$_2$ batteries can be divided into four types: aqueous, non-aqueous, hybrid

(mixed aqueous/non-aqueous) and solid-state. Of these, non-aqueous $Li-O_2$ batteries are currently undergoing the strongest development, so we will focus our discussion on them. Figure 6 shows schematically how non-aqueous $Li-O_2$ batteries work.
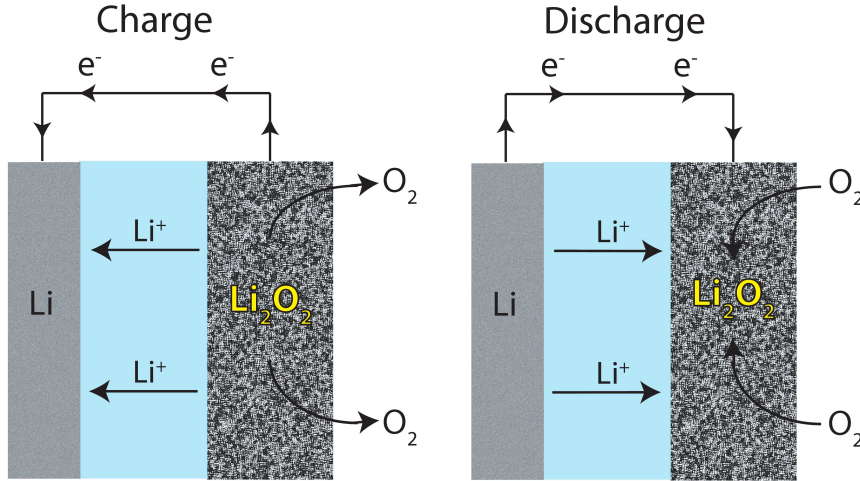
Figure 6: *Schematic representation of a non-aqueous $Li-O_2$ battery. During discharge, the Li_2O_2 that forms on the porous carbon support acts as the cathode, which decomposes as the battery is charged.*

During battery discharge, Li_2O_2 is formed on the porous carbon support. A recent study by Bruce and co-workers using *in situ* surface enhanced Raman spectroscopy (SERS) provided evidence that LiO_2 forms as an intermediate state during the oxygen reduction reaction (ORR) [25] as follows:

$$O_2 + e^- \rightarrow O_2^- \tag{1.4}$$
$$O_2^- + Li^+ \rightarrow LiO_2 \tag{1.5}$$
$$2LiO_2 \rightarrow Li_2O_2 + O_2 \quad \text{at 2.96 V vs. Li/Li}^+. \tag{1.6}$$
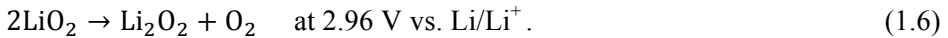
During battery charging, Li_2O_2 decomposes directly in a one-step reaction and evolves into O_2 following the oxygen evaluation reaction (OER) as follows:

$$Li_2O_2 \rightarrow 2Li^+ + 2e^- + O_2 \uparrow \tag{1.7}$$

High overpotential during charging, poor capacity retention and low cycle life are still the main impediments to the practical application of Li-air battery technology [26,27].

As described above, the proper choice of electrolyte is very important for battery performance. Superoxide radical anions O_2^-, which are formed during the ORR, can also be solvated by the solvent molecule surrounding them. If the mechanism of solvent attack is predominant, much less Li_2O_2 will be produced, and the solvent will decompose by forming lithium-alkyl carbonates. Studies of different electrolytes show that carbonate-based electrolytes are more prone to such attacks. Therefore, electrolytes such as EC and DMC, which are commonly used in Li-ion batteries, are not suitable for Li-air batteries. Ether-based electrolytes such as TEGDME (tetraethylene glycol dimethyl ether) and DMSO (dimethyl sulfoxide) are more stable against oxygen-reducing species and are thus preferable [28]. However, even with these electrolytes, the formation of undesirable carbonate products has been reported [28]. Thus the search for stable electrolytes continues.

Even if a stable electrolyte is found, capacity fading will occur as a consequence of the incomplete oxidation of Li_2O_2 upon charging, which is a consequence of caused by the poor ionic and electronic conduction of Li_2O_2 [29]. The progressive buildup of inactive Li_2O_2 during repeated battery cycles, in addition to byproduct accumulation, eventually leads to cell failure. The main factors influencing Li_2O_2 morphology, and hence cell capacity, are the current density and the solubility of the LiO_2 intermediate [30,31]. Poor LiO_2 solubility by the electrolyte, *i.e.* low donor numbers, promotes the formation of a passivating Li_2O_2 film, which is even more pronounced by high current densities and leads to early cell death [14]. In contrast, good LiO_2 solubility, i.e. high donor numbers, leads to Li_2O_2 growth in solution before deposition on the electrode surface. A potential approach to mitigate the passivating formation of an amorphous Li_2O_2 film at high rates and in low-donor electrolytes is to promote the formation of nanometer-sized Li_2O_2 crystallites at the electrode surface.

It has been reported that different metal and metal-oxide nanoparticles are used as catalysts to promote good round trip efficiency, to improve capacity retention and to prolong the cycle life of batteries [32]. However, the underlying mechanism for these improvements is not yet known. Detailed knowledge about the mechanism is required in order to design the ideal catalyst for Li-air batteries [32].

In the course of this thesis research, we have developed procedures to reveal the working mechanisms of catalysts particles. Furthermore, we have studied the role of hexagonal NiO nanoparticles as grain refiners to control the structure of grown Li_2O_2.

4. Goal of this dissertation

From the above discussion, it is clear that next-generation Li-ion, Li-S, Li-O$_2$, Na-ion, Na-S and Na-O$_2$ batteries are the most promising technologies for future applications, and that they are far from having reached their full potential. Battery performance essentially depends on the electrode-electrolyte materials, their interaction (interconnection) and their efficiency in drawing and supplying current. Therefore, to unveil the full potential of batteries, research efforts must be focused on materials selection, synthesis, cell design, and evaluation of cell performance in light of the fundamental understanding of the materials' behaviour and kinetics during battery operation.

In this thesis, we first emphasize on the preparation of better electrodes and electrolytes for Li-ion, Na-ion, Li-S, and Li-O$_2$ batteries. Evaluating the performance of a macro scale battery and correlating the electrode, electrolyte structure; morphology and chemical state using TEM and SEM studies, the main criteria for battery performance are identified for each cases.

To understand the performance of Li-O$_2$ batteries, transmission electron microscopy (TEM) is needed in order to obtain chemical and structural details of the discharge products at a very local scale. However, degradation of the sample upon air exposure and electron-beam and preserving the native details of the discharge products at nanometer scale during the sample preparation poses challenges. In this thesis we provide means of using TEM for Li-O$_2$ battery research in a reliable and effective manner.

Electrode nanoparticles are the building blocks of a battery. Thus, to improve the overall performance of a battery, we must improve the performance of the individual nanoparticles. To do so, we must determine the respective effects of electrode particle size, shape, structure, grain–grain boundary, defects and doping on electrode degradation. A macro battery is composed of thousands of millions of nanoparticles with additives and binders. Based on the average information about macro batteries obtained via different spectroscopic and diffraction techniques, it is almost impossible to uncouple the roles of all morphological and structural parameters without considerable ambiguity. The transmission electron microscope (TEM) is one of most important characterization tools in the field of materials science because it enables the simultaneous study of morphology, structure, and chemical information at the atomic level. Indeed, single-particle analysis is a routine task with a TEM. Hence, if a setup is built that allows us to create a battery with a single nanoparticle electrode and to perform charging-discharging inside a TEM, the

high temporospatial resolution of the TEM will allow *in situ* visualization of the battery processes down to the atomic level. This will allow us to uncouple the effects of different morphological and structural parameters on battery performance. This makes "operando TEM" *the* technique of choice for battery experiments, which justifies the tremendous interest in operando TEM battery research in the past eight years [33,34].

It is also extremely important that the experimental conditions inside the TEM should correspond as closely as possible to the conditions to which the nanoparticle electrodes would be subjected in a macro battery. Only then can the results obtained with an operando TEM experiment be used directly to synthesize better electrode materials, the entire potential of which can be fully leveraged. In this thesis we place special emphasis on building setups that mimic exactly the bulk environment in the operando TEM study. Using noble approach delithiation of $LiFePO_4$ cathode is studied using *in situ* TEM. *In situ* TEM is further applied to understand critical details about fabrication and operation of thin film batteries.

4.1. Thesis structure

This dissertation contains nine chapters, including this introduction (**Chapter 1**), where the basic principles of battery technologies are discussed.

Chapter 2 contains a brief description of the experimental techniques used at various stages of the research with a special emphasis on TEM. A brief description of SEM is also included.

Chapter 3 explores the research carried out on Li-ion, Na-ion, Li-S and Li-air macro batteries. The main goal of this research is to build high-power batteries with high energy densities. This research was carried out in collaboration with various research groups at TU Delft, whereas the work described in this thesis focuses mainly on my own contributions.

Chapter 4 evaluates the best possible parameters to study Li-air battery discharge products in a TEM.

Chapter 5 focuses on a unique way of using standard TEM grids as Li-air battery cathodes for studying Li-air battery discharge products in a reliable way.

Chapter 6 marks the second part of this thesis. It discusses the fabrication strategy of different MEMS devices that will be used in future operando TEM

battery studies. These MEMS devices are fabricated in the Kavli Nanolab of TU Delft.

Chapter 7 explores the use of MEMS heater to unveil the crystallization process of thin film $LiFePO_4$ and effect of high current densities in Ni current collector.

Chapter 8 focuses on developing a broadly applicable open-cell design for operando TEM battery experiments. In these experiments, the nanoparticle electrode should be under conditions that are as similar as possible to those in a macro battery. This is achieved by allowing Li ions to (de)intercalate from every part of the electrode particle, correlating the microstructure to local chemical and electronic structural changes during (dis)charge.

Chapter 9 explores the possibility to insert liquid electrolytes into the TEM to study the battery process via operando TEM in a liquid environment. A discussion of the future direction of operando TEM battery research rounds out this chapter and the thesis.

References

1.   Electricity production from coal sources (% of total). *2014* Available at: http://data.worldbank.org/indicator/EG.ELC.COAL.ZS

2.   Fossil fuel energy consumption (% of total). *2014* Available at: http://data.worldbank.org/indicator/EG.USE.COMM.FO.ZS

3.   Global Greenhouse Gas Emissions Data. *2016* Available at: https://www.epa.gov/ ghgemissions/global-greenhouse-gas-emissions-data

4.   Takle E. Global warming – impact on greenhouse gases. *2008* Available at: https://www.extension.iastate.edu/agdm/articles/others/TakMar08.html

5.   The Climate Time Machine. *2008* Available at: http://climatekids.nasa.gov/review/time-machine/

6.   Ambient (outdoor) air quality and health. *2016* Available at: http://www.who.int/ mediacentre/factsheets/fs313/en/

7.   Paris Agreement. *2015* Available at: https://ec.europa.eu/clima/policies/ international/ negotiations/paris/

8.   Ali ABMS. *Smart grids: Opportunities, developments, and trends*. (2013). doi:10.1007/978-1-4471-5210-1

9.   Pearre NS, Swan LG. Technoeconomic feasibility of grid storage: Mapping electrical services and energy storage technologies. *Appl Energy* (2015) **137**:501–510.

doi:10.1016/j.apenergy.2014.04.050

10. Müller M, Viernstein L, Truong CN, Eiting A, Hesse HC, Witzmann R, Jossen A. Evaluation of grid-level adaptability for stationary battery energy storage system applications in Europe. *J Energy Storage* (2017) **9**:1–11. doi:10.1016/j.est.2016.11.005

11. Sources of Greenhouse Gas Emissions. *2015* Available at: https://www.epa.gov/ghgemissions/sources-greenhouse-gas-emissions

12. Root M. *The TAB Battery Book*. (2010). doi:10.1036/9780071739917

13. Winter M, Brodd RJ. What are batteries, fuel cells, and supercapacitors? *Chem Rev* (2004) **104**:4245–4269. doi:10.1021/cr020730k

14. Singh P, Deepak. A Template for Enhanced Lithium Ion Battery Electrodes. (2014)

15. Broadhead, John and Kuo HC. "Electrochemical Principles and Reactions," in *Handbook of Battery*

16. Nitta N, Wu F, Lee JT, Yushin G. Li-ion battery materials: Present and future. *Mater Today* (2015) **18**:252–264. doi:10.1016/j.mattod.2014.10.040

17. Imanishi N, Luntz AC, Bruce P. *The Lithium Air Battery: Fundamentals*. doi:10.1007/978-1-4899-8062-5

18. Rosenman A, Markevich E, Salitra G, Aurbach D, Garsuch A, Chesneau FF. Review on Li-Sulfur Battery Systems: An Integral Perspective. *Adv Energy Mater* (2015) **5**:1–21. doi:10.1002/aenm.201500212

19. Kim H, Kim H, Ding Z, Lee MH, Lim K, Yoon G, Kang K. Recent Progress in Electrode Materials for Sodium-Ion Batteries. *Adv Energy Mater* (2016)1–38. doi:10.1002/aenm.201600943

20. Ha S, Kim JK, Choi A, Kim Y, Lee KT. Sodium-metal halide and sodium-air batteries. *ChemPhysChem* (2014) **15**:1971–1982. doi:10.1002/cphc.201402215

21. Lu JY, Jiang QS, Qin L. The Research on Energy-Storaged Application of Na/S Battery. *Manuf Sci Mater Eng Pts 1 2* (2012) **443**–**444**:189–192. doi:10.4028/www.scientific.net/AMR.443-444.189

22. Adelhelm P, Hartmann P, Bender CL, Busche M, Eufinger C, Janek J. From lithium to sodium: Cell chemistry of room temperature sodium-air and sodium-sulfur batteries. *Beilstein J Nanotechnol* (2015) **6**:1016–1055. doi:10.3762/bjnano.6.105

23. Ge P, Fouletier M. Electrochemical intercalation of sodium in graphite. *Solid State Ionics* (1988) **28**–**30**:1172–1175. doi:10.1016/0167-2738(88)90351-7

24. Ji X, Nazar LF. Advances in Li–S batteries. *J Mater Chem* (2010) **20**:9821. doi:10.1039/b925751a

25. Bruce PG, Freunberger S a., Hardwick LJ, Tarascon J-M. Li–O2 and Li–S batteries with high energy storage. *Nat Mater* (2011) **11**:172–172. doi:10.1038/nmat3237

26. McCloskey BD, Bethune DS, Shelby RM, Girishkumar G, Luntz AC. Solvents ' Critical Role in Nonaqueous Lithium À Oxygen Battery. *J Phys Chem Lett* (2011) **2**:1161–1166. doi:10.1021/jz200352v

27. Christensen J, Albertus P, Sanchez-Carrera RS, Lohmann T, Kozinsky B, Liedtke R, Ahmed J, Kojic A. A Critical Review of Li/Air Batteries. *J Electrochem Soc* (2012) **159**:R1. doi:10.1149/2.086202jes

28. Balaish M, Kraytsberg A, Ein-Eli Y. A critical review on lithium-air battery electrolytes. *Phys Chem Chem Phys* (2014) **16**:2801–2822. doi:10.1039/C3CP54165G

29. Mitchell RR, Gallant BM, Thompson C V., Shao-Horn Y. All-carbon-nanofiber electrodes for high-energy rechargeable Li–O2 batteries. *Energy Environ Sci* (2011) **4**:2952. doi:10.1039/c1ee01496j

30. Adams BD, Radtke C, Black R, Trudeau ML, Zaghib K, Nazar LF. Current density dependence of peroxide formation in the Li–O2 battery and its effect on charge. *Energy Environ Sci* (2013) **6**:1772–1777. doi:10.1039/c3ee40697k

31. Johnson L, Li C, Liu Z, Chen Y, Freunberger S a, Ashok PC, Praveen BB, Dholakia K, Tarascon J-M, Bruce PG. The role of LiO2 solubility in O2 reduction in aprotic solvents and its consequences for Li-O2 batteries. *Nat Chem* (2014) **6**:1091–9. doi:10.1038/nchem.2101

32. Wang Z-L, Xu D, Xu J-J, Zhang X-B. Oxygen electrocatalysts in metal-air batteries: from aqueous to nonaqueous electrolytes. *Chem Soc Rev* (2013) **43**:10.1039/c3cs60248f. doi:10.1039/c3cs60248f

33. Liu XH, Huang JY. In situ TEM electrochemistry of anode materials in lithium ion batteries. *Energy Environ Sci* (2011) **4**:3844. doi:10.1039/c1ee01918j

34. Wang C-M. In situ transmission electron microscopy and spectroscopy studies of rechargeable batteries under dynamic operating conditions: A retrospective and perspective view. *J Mater Res* (2015) **30**:326–339. doi:10.1557/jmr.2014.281

Appendix A

Li-ion Battery:

Cathode materials. Different cathode materials are currently being used in commercial lithium-ion batteries. In addition to being environmentally friendly and inexpensive, the main requirements, originally formulated by Whittingham [1], of cathode materials are as follows.

(a) They must contain a readily reducible-oxidizable, material that can assume various valence states. Transition metals are common in this role because they have more than one stable oxidation state.

(b) They must ensure lithium (de)insertion in a reversible manner. This essentially means that the host structure should remain as unchanged as possible as lithium is (de)inserted.

(c) They should feature high capacity and high voltage, preferably around 4 V (limited by the electrolyte stability) to provide high-energy storage.

(d) They should allow fast (de)insertion of lithium ions to ensure high power densities. They should have good electronic and ionic conducting properties. Good electronic conductivity properties ensure complete (de)lithiation without the need for additional carbon additives (such as carbon black). On the other hand, good ionic conductivity will reduce the need for a porous structure to ensure electrolyte flow. These properties will further increase the taping and energy densities of the battery. Table 1 lists the most common cathode materials and their basic characteristics. Every cathode has been further modified via doping and surface coating.

Material	Crystal structure	Voltage (V) vs. Li/Li$^+$	Specific capacity (mAhg^{-1}) (Theoretical / experimental)
LiCoO$_2$	Layered	3.8	274/148 [2]

LiNi$_{0.33}$Co$_{0.33}$Mn$_{0.33}$O$_2$	Layered	3.7	280/160 [3]
LiMn$_2$O$_4$	Spinel	4.1	148/120 [4]
LiFePO$_4$	Olivine	3.4	170/165 [5]
LiFeSO$_4$F	Tavorite	3.7	151/120 [6]

Table 1: *Most popular cathode materials for Li-ion batteries and their fundamental properties.*

In the course of this thesis research, we have studied: LiFePO$_4$ as cathode for Li-ion battery.

Anode materials. Theoretically, lithium metal has the highest possible specific capacity (3860 mAhg^{-1}) of all the possible anodes of lithium-ion batteries. However, the possibility of an electrical short circuit occurring due to dendritic growth of the lithium during repeated battery cycling poses a safety hazard. Currently graphite, which has a capacity of 372 mAhg^{-1}, is the most commonly used anode material in lithium-ion batteries. To improve the energy and power densities of lithium-ion batteries, the search has continued for anode materials that have a low potential against lithium, provide high capacity, facilitate the diffusion of Li ions into the anode, have a good cycling life and pose no safety concerns. In terms of their (de)intercalation reaction mechanism, Li-ion battery anodes can be divided into three main groups.

(a) Intercalation materials. As stated above, graphite is the most commonly used anode material because it allows intercalation of one Li-ion with six carbon atoms. As an alternative to graphite, soft carbon, hard carbon, carbon nanotubes and graphene, different polymorphous titanium oxides (TiO$_2$) and Li$_4$Ti$_5$O$_{12}$ are the most intensively researched anode material, based on such intercalation mechanisms. [7–9].

(b) Alloy materials. Anode materials based on alloying mechanisms can feature much larger capacities than graphite anodes. For example, the specific theoretical capacity for tin oxide and silicon are 780 and 4200 mAhg^{-1}, respectively [10,11]. However, high volume expansion-contraction during battery cycling leads to a shorter cycle life and poor capacity retention. Downsizing and composite fabrication are the most promising approaches. Apart from Si and SnO$_2$, the most intensively researched materials are Ge, Sn and Bi [12].

(c) Conversion materials. Transition metal oxides, phosphides, sulfides and nitrides (M$_x$N$_y$; M: Fe, Co, Cu, Mn, Ni and N: O, P, S and N) when utilized as anodes undergo conversions during battery cycling:

$$M_x N_y + zLi^+ + ze^- \leftrightarrow Li_z N_y + xM. \hspace{2cm} (1.3)$$

Multiple electron transfer during the reaction step generally achieves a good capacity (500–1000 $mAhg^{-1}$). However, a detailed understanding is required before these materials can be commercialized [12].

In the course of this thesis research, we have studied: Si nanoparticles, a-TiO2 as anodes for Li-ion battery.

Electrolytes. The role of electrolytes is to transfer the Li-ions from the cathode to the anode during charging and from the anode to the cathode during discharging.

The electrolytes used in Li-ion batteries can mainly be divided into four types: Non-aqueous, ionic liquid, gel polymer and solid-state electrolytes. It is worth mentioning that aqueous electrolytes are not suited for Li-ion batteries due to their cell voltage of ~3 V (>1.23 V). For cell voltages greater than 1.23 V, H_2O decomposes into H^+ and OH^- ions.

Non-aqueous electrolytes. Lithium salts dissolved in organic solvent(s) are used as non-aqueous electrolytes for Li-ion batteries. The solvents should be aprotic in order to be stable against metallic lithium and have a high polarity to dissolve lithium salts. The solvents should have a low melting point and high boiling point. Moreover, the solvent should have a lower viscosity to ensure a higher ionic conductivity of the electrolyte. It is quite difficult for a particular solvent to satisfy all these conditions. Thus, two different solvents are usually mixed in order to complement each other's properties. For example, ethylene carbonate (EC) has a high polarity but is highly viscous. Therefore, it is combined with dimethyl carbonate (DMC), which has a low viscosity but also a low polarity.

Lithium salts should have a high degree of dissociation and high mobility. $LiBF_4$, $LiPF_6$, $LiAsF_6$ salts are the most commonly used lithium salts dissolved in non-aqueous electrolytes [13].

Ionic-liquid electrolytes. Room temperature ionic liquids (RTIL) are salts having a low-temperature melting point and that may be used as electrolyte solvents in lithium-ion batteries. When a lithium salt $[Li^+][X^-]$ is dissolved in an ionic liquid $[A^+][X^-]$, it forms a new ionic liquid $[Li^+]_m[A^+]_n[X^-]_{m+n}$ consisting of two cations. The negligible vapor pressures of the ionic liquids make them inflammable. In addition, they feature a broad electrochemical stability window that is usually greater than 4 V. However, the high viscosity of ionic liquids leads to poor infusion of the electrodes and thus results in a low capacity of the battery [14].

Solid electrolytes. Inorganic solid electrolytes are non-flammable and have a high mechanical stability. Replacing liquid electrolytes with inorganic solid electrolytes

is considered to be the ultimate solution to the above-mentioned safety issues. However, a disadvantage is their low ionic conductivity. This has prompted worldwide research to find solid electrolytes with fast ionic conductivity. Lithium-superionic conductors (LISICONs), argyrodites, garnets, sodium-superionic conductors (NASICONs), Li-nitrides, Li-hydrides, perovskites and Li-halides are the most intensively researched electrolyte families, some of which have a conductivity close to their liquid counterparts [15]. In the course of this thesis research, we have studied the performance of Li_6PS_5Br as solid-state electrolyte.

Solid electrolytes are also used in thin-film batteries via sputtering or pulsed laser deposition. LiPON deposited from a Li_3PO_4 target in the presence of N_2 are the most popular kind of solid electrolytes used for thin-film batteries [16]. We have used LiPON for operando electrochemical delithiation TEM studies.

Another family of solid electrolytes are gel polymers [17]

References

1.   Whittingham MS. Lithium batteries and cathode materials. Chem Rev (2004) 104:4271–4301. doi:10.1021/cr020731c

2.   Cho J, Kim Y-W, Kim B, Lee J-G, Park B. A Breakthrough in the Safety of Lithium Secondary Batteries by Coating the Cathode Material with AlPO4 Nanoparticles. Angew Chemie Int Ed (2003) 42:1618–1621. doi:10.1002/anie.200250452

3.   Lin F, Markus IM, Nordlund D, Weng T-C, Asta MD, Xin HL, Doeff MM. Surface reconstruction and chemical evolution of stoichiometric layered cathode materials for lithium-ion batteries. Nat Commun (2014) 5:3529. doi:10.1038/ncomms4529

4.   Lee M, Lee S, Oh P, Kim Y, Cho J. High Performance LiMn 2 O 4 Cathode Materials Grown with Epitaxial Layered Nanostructure for Li-Ion Batteries. (2013)798. doi:10.1021/nl404430e

5.   Yamada A, Chung SC, Hinokuma K. Optimized LiFePO4 for lithium battery cathodes. J Electrochem Soc (2001) 148:A224–A229. doi:10.1149/1.1348257

6.   Sobkowiak A, Roberts MR, Younesi R, Ericsson T, Häggström L, Tai CW, Andersson AM, Edström K, Gustafsson T, Björefors F. Understanding and controlling the surface chemistry of LiFeSO4F for an enhanced cathode functionality. Chem Mater (2013) 25:3020–3029. doi:10.1021/cm401063s

7.   Kaskhedikar NA, Maier J. Lithium storage in carbon nanostructures. Adv Mater (2009) 21:2664–2680. doi:10.1002/adma.200901079

8.   Wagemaker M, Mulder FM. Properties and promises of nanosized insertion materials for li-ion batteries. Acc Chem Res (2013) 46:1206–1215. doi:10.1021/ar2001793

9.   Zhu G-N, Wang Y-G, Xia Y-Y. Ti-based compounds as anode materials for Li-ion batteries. Energy {&} Environ Sci (2012) 5:6652. doi:10.1039/c2ee03410g

10.   Wu H, Cui Y. Designing nanostructured Si anodes for high energy lithium ion batteries. Nano

Today (2012) 7:414–429. doi:10.1016/j.nantod.2012.08.004

11. Li H, Wang Z, Chen L, Huang X. Research on advanced materials for Li-ion batteries. Adv Mater (2009) 21:4593–4607. doi:10.1002/adma.200901710

12. Goriparti S, Miele E, De Angelis F, Di Fabrizio E, Proietti Zaccaria R, Capiglia C. Review on recent progress of nanostructured anode materials for Li-ion batteries. J Power Sources (2014) 257:421–443. doi:10.1016/j.jpowsour.2013.11.103

13. Morita Masayuki IM and MY. "Organic Electrolytes for Rechargeable Lithium Ion Battery," in Lithium Ion Batteries Fundamentals and Performance

14. Lewandowski A, Świderska-Mocek A. Ionic liquids as electrolytes for Li-ion batteries-An overview of electrochemical studies. J Power Sources (2009) 194:601–609. doi:10.1016/j.jpowsour.2009.06.089

15. Bachman JC, Muy S, Grimaud A, Chang HH, Pour N, Lux SF, Paschos O, Maglia F, Lupart S, Lamp P, et al. Inorganic Solid-State Electrolytes for Lithium Batteries: Mechanisms and Properties Governing Ion Conduction. Chem Rev (2016) 116:140–162. doi:10.1021/acs.chemrev.5b00563

16. Knauth P. Inorganic solid Li ion conductors: An overview. Solid State Ionics (2009) 180:911–916. doi:10.1016/j.ssi.2009.03.022

17. Park, Soo-Jin SM-K and KS. "Next-Generation Electrolytes for Li Batteries," in High Energy Density Lithium Batteries.

CHAPTER 2

EXPERIMENTAL TECHNIQUES

This chapter is devoted to the experimental techniques used in this thesis. First, a short introduction of transmission electron microscopy (TEM) is given with the focus on imaging and analytical techniques. In the next section scanning electron microscopy (SEM), which is used for morphological analysis of the electrodes is briefly discussed. In the last section of this chapter the overview of the experimental setups used during the dynamic operando TEM experiments and the sample preparation using focus ion beam (FIB) are discussed.

1. Transmission electron microscopy[i]

Transmission electron microscopy (TEM) is one of most frequently used characterization tools in materials science because it allows a sample to be quantified in terms of its structure and composition up to atomic level. In TEM, highly energetic electrons are used as illumination source. The Rayleigh criterion states that the smallest resolvable distance δ is a function of the illumination source wavelength λ in accordance with the relation

$$\delta = \frac{0.61\lambda}{\mu \sin \beta}$$

where, μ is the refractive index of the viewing medium and β is the semi-angle of collection. A highly energetic electron beam (which has a small wavelength of 3.70, 2.51 and 1.96 pm at 100, 200 and 300 keV, respectively), provides structural information in the form of images or diffraction patterns down to the atomic scale in TEM [1].

The very first TEM developed in 1931 by Max Knoll and Ernst Ruska was operated at an accelerating voltage of 50 kV [2]. In view of the inverse relationship between the energy and the wavelength of an accelerated electron, and to achieve higher resolution, TEMs with very high accelerating voltages (1–3 MeV) had been developed by the 1980s. However, highly energetic electrons led to irreversible radiation damage of the samples. From 1990 onwards, intermediate-voltage (200–400 keV) TEMs became more popular [1]. Improved electromagnetic lenses extended the resolution limit. Recent developments of aberration correctors provide information up to 50 pm, which permits the atomic column arrangement of most materials to be visualized [3].

Highly energetic electrons transmitting through a thin sample interact with the sample, generating a range of signals as shown in Figure 1 [1]. A fraction of the electrons either remain parallel to the direction of incident electrons, called a direct beam, or are elastically scattered, i.e. deviate from the incident direction due to the specimen without any loss of energy. The remaining electrons that lose energy undergo inelastic scattering, resulting in several detectable signals, like X-rays. In a conventional TEM, imaging and diffraction are utilized to determine the structural and morphological details of the sample. Further compositional as well as electronic structure quantification techniques such as EDX and EELS (EFTEM) are quite routine in modern microscopes (known as

---

[i] *Most of the text for this section is adopted from Ref. [1].*

analytical TEMs).
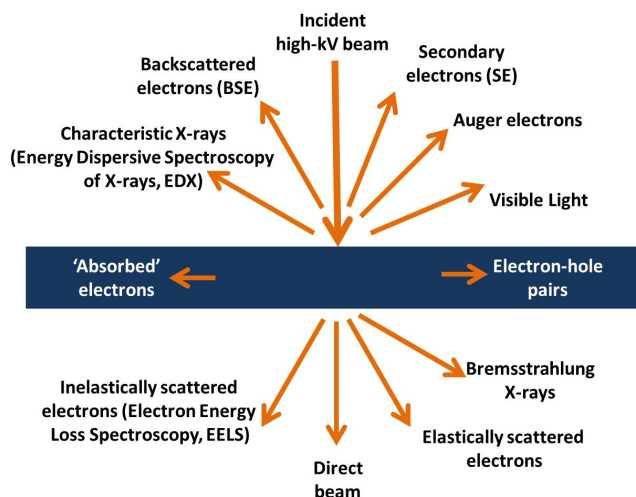
Figure 1: *Schematic of the signals generated when a high-energy electron beam interacts with a thin specimen. These signals can be collected using suitable detectors that allow various quantitative analyses of the sample.[ii]*

In a TEM electron beam generated from a thermionic or field electron emission source, guided by an electromagnetic condenser system, illuminates the specimen in high vacuum. After interacting with the thin sample, the transmitted electron beam passes through the objective, and then through the intermediate and projector lenses to a florescent screen or camera for recording. Conventional TEM, in which the beam remains static, can be operated in imaging or diffraction mode. Figure 2 is a ray diagram showing the imaging and diffraction processes [1]. The strength of the intermediate lens can be changed, depending on whether one wants to obtain image or diffraction information. In imaging mode, an objective aperture can be inserted in a back focal plane (BFP) of the objective lens. If the objective aperture is placed such that only the central beam can transmit, a bright field (BF) image is obtained, whereas if the objective aperture blocks the central beam and an image is formed using diffracted beam only, a dark-field (DF) image is obtained. To obtain a diffraction pattern, the electron beam is either focused on a small area of the sample (for convergent-beam electron diffraction, CBED) or an aperture is

---

[ii] *The directions shown for each signal do not necessarily represent the physical direction of the signal.*

introduced at the image plane of the objective lens (for selected-area electron diffraction, SAED).
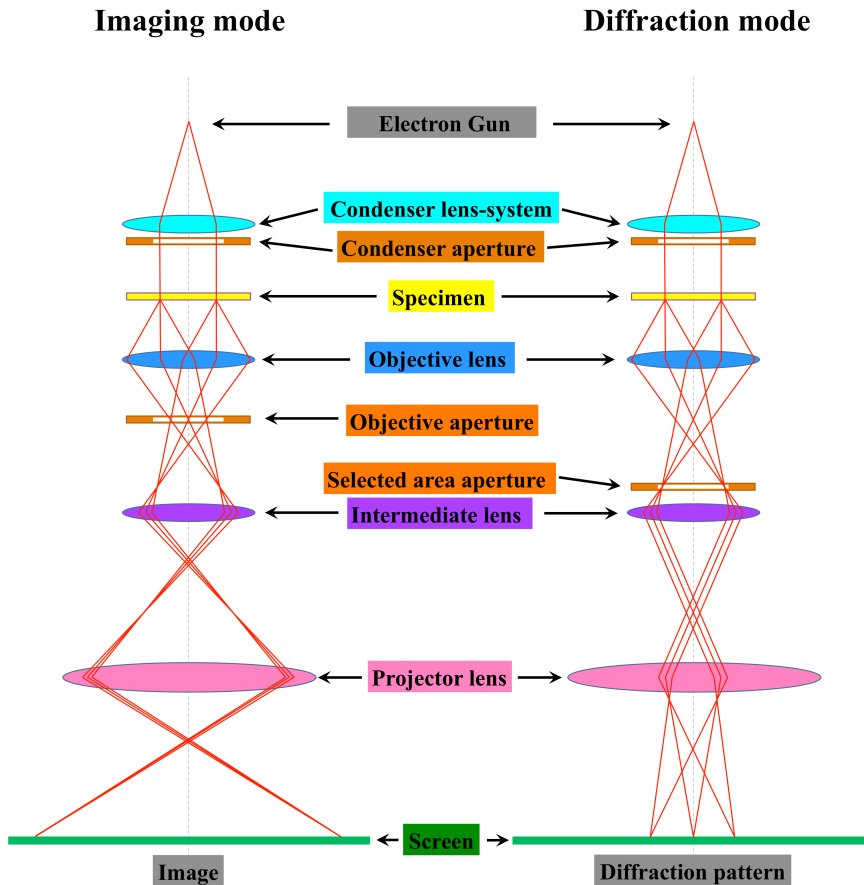
Figure 2: *Ray diagram of imaging-mode and (selected-area) diffraction-mode operation.*

The electron beam can also be focused on a small spot that can be scanned over the area of the sample in STEM mode [1]. Scanning in TEM is achieved by incorporating electromagnetic beam deflection coils in the illumination system, as shown in Figure 3. When the electron beam converges into a spot, it is called a probe; typical probe sizes range from 0.05 to 0.2 nm. The probe is scanned over the specimen, and the forward-scattered electrons are collected to form an image.

STEM mode

Electron Gun

Condenser lenses

Condenser aperture

Deflection scan coils

Upper-objective polepiece

Specimen

Incident
convergent
beam

Specimen

HAADF
detector

HAADF
detector

ABF
detector

BF
detector

ABF
detector
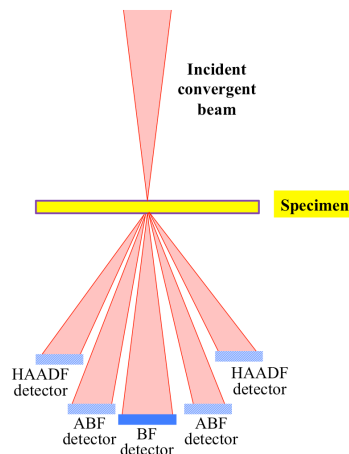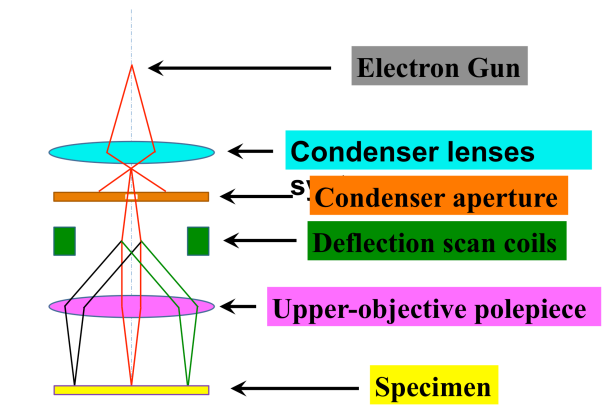
Figure 3: Ray diagram illustrating the operation of a TEM in STEM mode. Positions of possible STEM detectors are indicated (not to the scale).

1.1. Contrast

In a TEM the electron wave, incident on the sample, changes in phase and amplitude due to interaction with the sample. With a perfect lens and at zero focus only the amplitude of the electron wave will be imaged. In order to image the phase of the electron wave either the zero beam or the diffracted beams have to be changed in their phase. This can be done either by a defocus or lens imperfection (which changes the phases of the diffracted beams, whereby the phase shift depends on the diffraction angle)) or by a phase shift of the central beam, which can be done with a phase plate, similar to the phase plate for optical microscopy, for which Zernike got the Nobel price [4].

The amplitude of the electron wave depends on the local scattering probability, which depends on the local mass and thickness (mass-thickness contrast) and/or on the orientation of crystalline areas in the sample (diffraction contrast). If the beam illuminates two neighbouring areas in an amorphous sample with low mass (or thickness) and high mass (or thickness), the high-mass region will scatter electrons more and over bigger angles. If these scattered electrons are (partly) blocked by an objective aperture, as in BF TEM mode, high-mass regions will appear darker (have a lower intensity (less electrons)). Diffraction contrast occurs due to specific orientation of a grain. If the beam illuminates a polycrystalline sample of one material and thickness, specific areas where atomic planes are aligned to the incident electron wave, satisfy the Bragg condition for strong scattering. Thus diffraction contrast provides information about the crystal orientation of a polycrystalline sample. Schematic representation of mass-thickness and diffraction contrast formation in BF TEM mode is shown in Figure 4. If both diffraction and mass-thickness contrast are present simultaneously, mass-thickness contrast cannot be uncoupled from diffraction contrast in TEM mode. However, in STEM mode using HAADF detector and low camera length it is possible to form an image with mainly mass-thickness contrast, known as Z-contrast imaging.
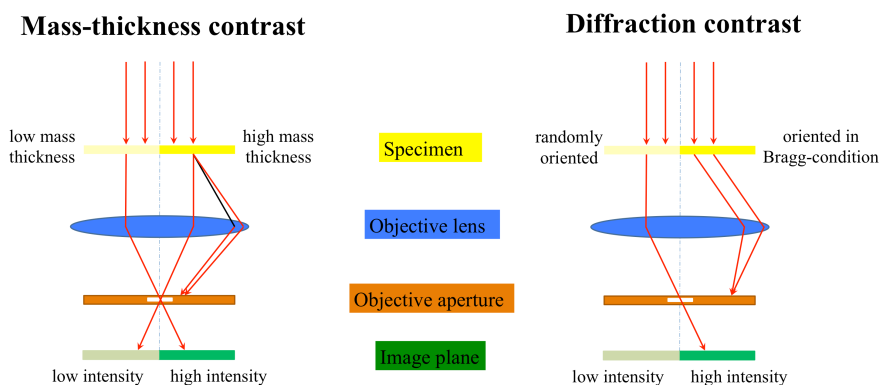
Figure 4: *Shows how mass-thickness contrast and diffraction contrast are generated in TEM mode.*

1.2. Microanalysis in TEM

One of the primary advantages of TEM investigations is the combination of above discussed imaging techniques with the other generated signals to analyze the chemistry of the specimens up to atomic level. A microscope capable of doing this kind of study is called analytical transmission electron microscope (ATEM) and the study is called microanalysis.

Most of the modern TEMs are equipped to carryout energy-dispersive X-ray spectroscopy (EDX), electron energy loss spectroscopy (EELS) and energy filtered transmission electron microscopy (EFTEM).

1.1.1. EDX. Energy-dispersive X-ray spectroscopy (EDS, EDX, or XEDS) uses element-specific emitted X-rays, which allows the local element composition to be determined [1]. At rest, atoms contain unexcited electrons in discrete energy levels (electron shells) bound to the nucleus. In TEM, the incident beam excites and ejects electrons from the bound inner shells and thus creates vacancies. As electrons from an outer higher-energy shell fill the vacancy, the difference in energy between the higher and lower-energy shell may be released in the form of an X-ray. Each of the possible transitions has energy unique to that element. Thus, by measuring the number and energy of the X-rays emitted from a specimen with an energy-dispersive spectrometer, the elemental composition of a specimen can be estimated. An example of an EDX analysis performed in STEM mode on Si@GaP nanowire is shown in Figure 5.
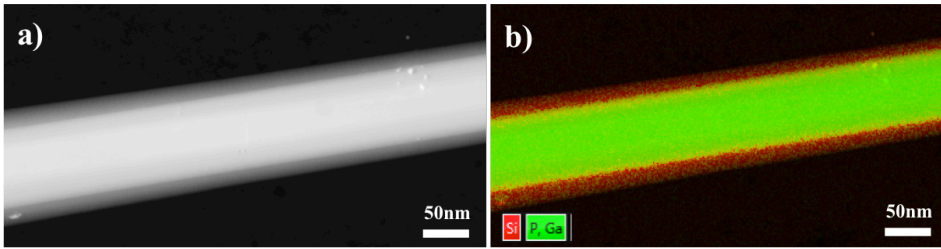
Figure 5: (a) HAADF image of a GaP@Si nanowire. (b) Elemental mapping confirms the Si shell on a GaP core.

1.1.2. EELS & EFTEM: As the electron beam is transmitted through a TEM specimen, some of the electrons lose energy in a variety of processes as discussed above. Electron energy loss spectroscopy (EELS) separates these losses of forward-scattered electrons into a spectrum using a magnetic prism. The magnetic prism ensures the separation of electrons based on their energy (loss), allowing the energy losses to be interpreted [1].

An EEL spectrum can be divided into no-loss, low-loss and high-loss regions, where ~40 eV is the arbitrary breaking point low-loss and high-lose regions. The low-loss and no-loss regions consist of the zero-loss peak, i.e. the electrons that have elastically scattered and a large proportion of forward-scattered electrons, and the electrons that have lost energy up to ~40 eV. This region provides information regarding the band gap of the sample, dielectric response, plasmonics and specimen thickness. In contrast, the high-loss region primarily

contains elemental information from the more tightly bound, core-shell electrons as well as details about bonding and atomic distribution [1]. Figure 6 shows EELS spectra acquired from a $NaFeSO_4$ cathode to determine the thickness of the sample and the ionization state of Fe.
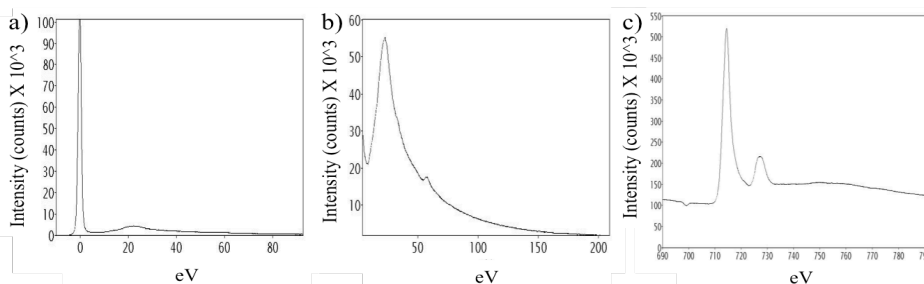
Figure 6: *EELS spectra acquired from a $NaFeSO_4$ cathode at different energy losses. (a) Zero loss and plasmon peak. (b) Plasmon and Fe-M edge. (c) Fe-L edge.*

In energy-filtered TEM (EFTEM), a slit is used to select a particular energy loss region. The slit width is generally 5–20 eV. Thus, the part of the sample containing the element that led to the particular energy loss will appear brighter in the image. In Chapter 8, we will see how EFTEM imaging is used to study the delithiation behaviour in $LiFePO_4$ nanoparticles via operando TEM.

2. Scanning electron microscopy

The scanning electron microscope (SEM) is another important characterization tool in materials science because it provides information about the morphology of a sample. As the name suggests, SEM—like TEM—also works with electron sources. The electron beam, which is focused by condenser lenses, is deflected in the x and y axes by a pair of scanning coils or pairs of deflector plates so that it scans in a raster fashion over a rectangular area of the sample surface [2].

When the primary electron beam interacts with the sample, the electrons lose energy by repeated random scattering and absorption within a teardrop-shaped volume of the specimen. This is known as the interaction volume, which extends less than 100 nm to approximately 5 µm into the surface. This interaction produces secondary electrons (SE), reflected or back-scattered electrons (BSE), photons of characteristic X-rays and light (cathodoluminescence) (CL) as well as absorbed current (specimen current). In most SEM studies, secondary electrons are imaged. Low-energy (<50 eV) secondary electrons originate within a few nanometers of the sample surface. As secondary electrons are emitted very close to the specimen surface, high-resolution (less than 1 nm) images of a sample surface can be produced. We

have used secondary-electron imaging to reveal the morphology of Li-O$_2$ battery discharge products. Figure 7 shows a typical image of the Li$_2$O$_2$ that forms on a gas diffusion cathode.
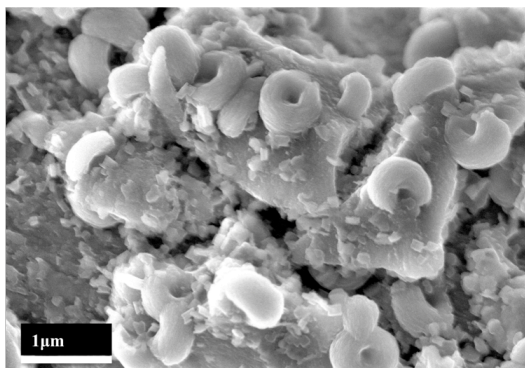
Figure 7: *Full/partial doughnut-shaped discharge products formed on porous carbon cathode after a Li-O$_2$ battery is discharged until 2.2 V with a current density of 50 μm/cm^2.*
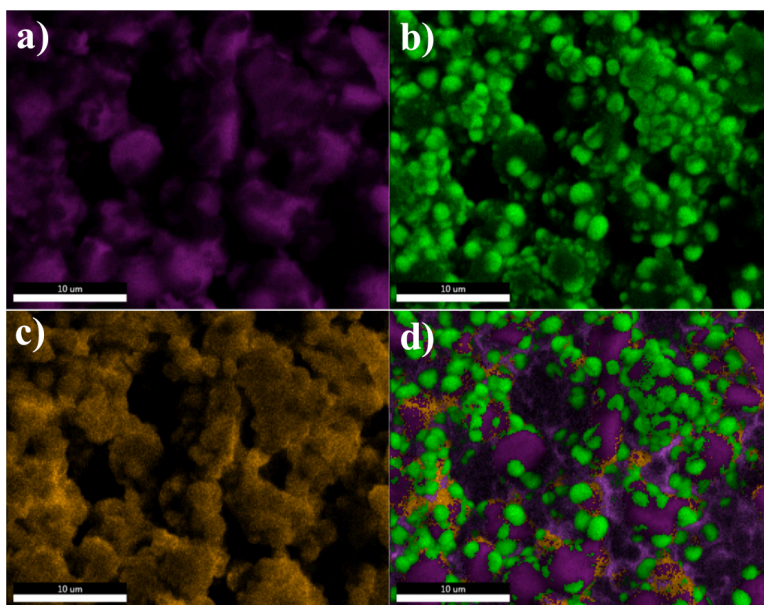
Figure 8: *SEM-EDX elemental mapping of a region of an activated carbon electrode, completely discharged to a 2.2 V cutoff at a current density of 50 μA/cm^2. Maps with (a) C-K, (b) O-K, (c) F-K and (d) overlaid with purple = C; green = O; and yellow = F.*

Furthermore, a SEM equipped with an EDX system allows elemental mapping [5]. Figure 8 shows the use of SEM-EDX to visualize Li$_2$O$_2$ particles on porous carbon electrodes. We used the same method in Chapter 3 to visualize the

preferential formation of Li_2O_2 on a NiO grain refiner on a porous carbon electrode.

3. *In situ* TEM experiments

TEM is a very powerful characterisation tool allowing a thorough structural and compositional understanding up to atomic level. In Chapter 3, applications of TEM in understanding the battery processes will be seen. However, due to the dynamic nature of the charge-discharge process, the ex-situ methods cannot answer some of the questions related to the dynamic process during battery operation [6]. For example, $LiFePO_4$ is considered to be one of the most promising cathode materials for Li-ion battery and has been studied in details. TEM shows presence of the domains in $Li_{0.5}FePO_4$ crystal aligned along the c-axis [7]. This observation subsequently raises several fundamental questions; such as when and how are these domains are formed? What role do domains play during battery operation? Answers to these questions only can be obtained by visualizing the dynamics of the particle under operating conditions (charge-discharge). The exact understanding of the controversial lithiation/delithiation mechanism in connection with particle size, grain–grain boundary, defects, doping will help designing better $LiFePO_4$ electrode, utilizing the full potential of the same.

Beside the unique possibility of visualizing up to the atomic level structural and chemical evolution of the electrode particles during the charge-discharge process *in situ* TEM provides the opportunity to charge-discharge a single nanoparticle without the use of binder and/or additives, making the interpretation of the result obtained from the *in situ* TEM experiment easy and reliable. These make *in situ* TEM one of **the most important tools** for the advancement of battery technologies [8–11]. *In situ* TEM also provides the opportunity to follow the structural and chemical evolution of the material during synthesis process, which in turn will illustrate optimal synthesis conditions and improve the efficiency of the process [12–15]. This can be utilized in battery material too[16].

In situ experiments have two important components: external stimuli and real time observations [17,18].External stimuli are applied inside the TEM using custom-made TEM holders with combination of micro electromechanical systems (MEMS) based devices. Real time observation required a fast detection system as well as high stability of the substrate. In this thesis electrical biasing, cooling and heating are used as external stimuli to understand the evolution of electrode materials. Experiments are performed using a FEI Tecnai operating at 200 keV and a FEI Titan microscope operating at 300 keV.

3.1. TEM holders

According to the requirement of the experiments, holders with different functionalities are used during this thesis.

3.1.1. Heating holder. Figure 9 shows the heating holder. This holder has four isolated electrical lines running through the tube for performing heating experiment inside TEM. Two of the lines are used for proving electrical power to the micro heater in the MEMS chip and other two lines are used to measure the power to enable high temperature stability through a software controlled feedback loop. This holder is used to study the crystallization process of LiFePO$_4$ (Chapter 7).
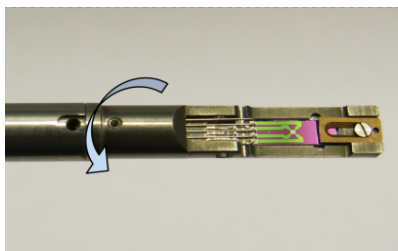
Figure 9: *The heating holder, allowing heating of the sample at high temperature maintaining high stability, arrow showing the tilt direction of the holder.*

3.1.2. Vacuum transfer electrical holder. Figure 11 shows the vacuum
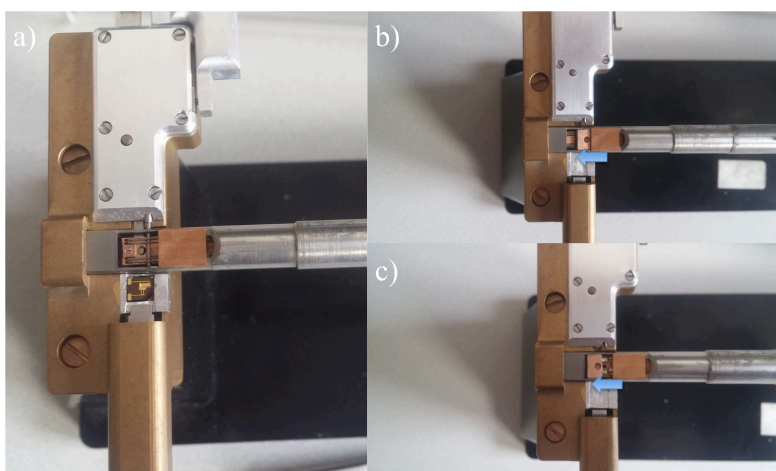
Figure 10: *The chip loading process in the vacuum transfer electrical holder is shown. (a) The MEMS chip is being inserted into the chip drawer, where the chip will be in contact with the four needles allowing electrode-biasing. (b) After the chip is inserted the drawer is being closed and (c) The drawer is completely closed. The O-ring around the drawer ensures that the sample (chip) will not be exposed to the ambient atmosphere when the holder is transported to the TEM.*

transfer electrical holder. The specially designed holder stand allows easy loading of the MEMS chip through the slit of the inside glovebox. By closing the drawer samples can be transferred from the glovebox to the TEM without any exposure to ambient atmosphere. Four isolated electrical lines permit heating or biasing experiment depending on the design of the MEMS chip. This holder is used to study delithiation mechanism in $LiFePO_4$ (Chapter 8).

3.1.3. Heating-biasing holder. Figure 11 shows the 10pin holder transfer holder, which allow simultaneous heating and biasing. Four lines are used for heating and rest six lines can be used for electrical biasing. This holder is used for performing battery experiment at elevated temperature (Chapter 9).
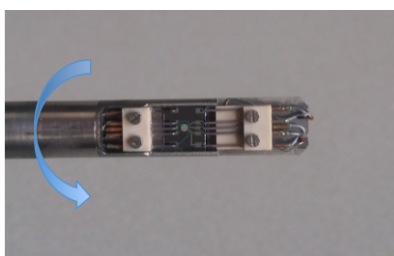
Figure 11: *The heating-biasing holder. Inset shows the MEMS chip with circular heating coil, designed such that there is no overlap between the heating coil and the biasing lines.*

3.2. Electrical measurements setup

The electrical measurements setup consists of four parts: Matrix module, IVVI rack, ADwin-GOLD module and PC (Figure 2.8). The holder is connected to the Matrix module though shielded cable. This module has 24 ports, depending on the holder and functionality 4, 8 or 10 ports correspond to the contacts from the holder. Matrix module is connected to the 'IVVI rack' and Adwin-Gold; and Adwin-Gold is connected to the personal computer (PC). The required voltage/ voltage profile is fed to the ADwin Gold using a Labview program. The Digital to Analog Converter (DAC) of the Adwin-Gold supply the voltage, which goes through the 'Matrix module' to the holder via shielded cable. The current meter in the IVVI rack measures the current running through the system and converts the current into a voltage with selectable amplification (10^6 to 10^9 V/A). This voltage is sent to the Analog to Digital Converter (ADC) of the ADwin-Gold. The current value is read and saved in the PC.

A separate control box controls heating functionality. Using a Labview program the temperature can be set using a feedback control. If simultaneous heating and biasing is required then the heating control box is connected to the Matrix module.
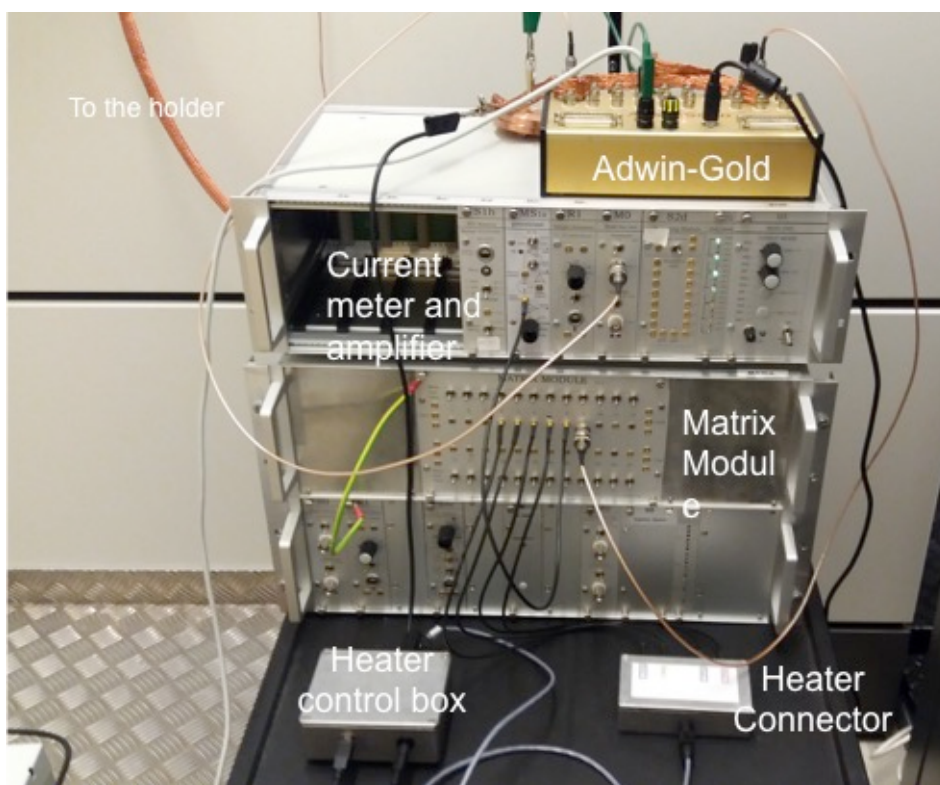
Figure 13. *Electrical measurements setup.*

3.3. Sample preparation for *in situ* TEM study: Focus ion beam

The quality of a TEM result depends strongly on the quality of the sample. Thin and representative samples are essential for true TEM analyses. We have used a focused ion beam (FIB) to prepare LiFePO₄ samples and solid-state battery samples for operando studies (Chapters 7, 8 & 9).

FIB operates in a similar fashion to an SEM except, as the name implies, FIB uses a finely focused beam of ions. At the source, gallium metal is placed in contact with a tungsten needle. The tungsten needle is then heated to melt the gallium, which wets the tungsten and flows to the tip of the needle, where the opposing forces of surface tension and electric field form the gallium into a cusp-shaped tip having a radius of ~2 nm. The high electric field ($>1{\times}10^8$ V/cm) within the small tip radius causes ionization and field emission of the gallium atoms. The generated Ga^+ beam guided by the lens, aperture and deflector system scans the sample. As the beam scans over the surface, it sputters material from the sample. Varying the primary beam current can

control the sputtering rate of the material and thus precision milling of the specimen down to the nanometer scale can be achieved. By collecting the sputtered ions, we can create an image.

Most FIBs are also equipped with a gas injection system (GIS). Gas is introduced by a nozzle positioned a few hundred microns above the area of interest. The gas is adsorbed on the surface of the material. The secondary electrons, which are produced when the FIB beam (either electron or ion) hits the surface, break the chemical bonds of the adsorbed gas molecules and separate them into different components: volatile components are sucked out of the system and others are deposited on the surface [19]. Using ion beam-induced deposition (IBID), we have deposited Pt to make electrical connections (Chapter 8).

Most modern FIBs are integrated within an SEM, and such instruments are called dual-beam SEM-FIBs. Addition of an SEM allows to select the desired location of a sample, without damaging the area (sputtering by Ga^+). We utilized this advantage of a dual-beam SEM-FIB to deposit Pt on the sample in order to connect the FIB lamella with the gold electrode precisely and without damaging the area.

References

1.   Williams DB, Carter CB. *Transmission Electron Microscopy*. 2nd ed. (2009). doi:10.1007/978-0-387-76501-3_1

2.   Ruska E. The development of the electron microscope and of electron microscopy. *Rev Mod Phys* (1987) **59**:627–638.

3.   Kisielowski C, Freitag B, Bischoff M, Lin H Van, Lazar S, Knippels G, Tiemeijer P, Stam M Van Der, Harrach S Von, Stekelenburg M, et al. Microscopy Microanalysis Detection of Single Atoms and Buried Defects in Three Dimensions by Aberration-Corrected Electron Microscope with 0 . 5-Å Information Limit. *Energy* (2008)469–477. doi:10.1017/S1431927608080902

4.   Zernike F. How I discovered phase contrast. *Science* (1955) **121**:345–349. doi:10.1126/science.121.3141.345

5.   Goldstein, Joseph, Newbury, Dale E. , Joy, David C., Lyman, Charles E., Echlin, Patrick, Lifshin, Eric, Sawyer, Linda MJR. *Scanning Electron Microscopy and X-ray Microanalysis*. 3rd ed. Springer US (2013).

6.   Harks PPRML, Mulder FM, Notten PHL. In situ methods for Li-ion battery research: A review of recent developments. *J Power Sources* (2015) **288**:92–105. doi:10.1016/j.jpowsour.2015.04.084

7.   Chen G, Song X, Richardson TJ. Electron Microscopy Study of the LiFePO4 to FePO4 Phase Transition. *Electrochem Solid-State Lett* (2006) **9**:A295. doi:10.1149/1.2192695

8. Liu N, Wu H, McDowell MT, Yao Y, Wang C, Cui Y. A yolk-shell design for stabilized and scalable Li-ion battery alloy anodes. *Nano Lett* (2012) **12**:3315–3321. doi:10.1021/nl3014814

9. Liu XH, Zheng H, Zhong L, Huang S, Karki K, Zhang LQ, Liu Y, Kushima A, Liang WT, Wang JW, et al. Anisotropic swelling and fracture of silicon nanowires during lithiation. *Nano Lett* (2011) **11**:3312–3318. doi:10.1021/nl201684d

10. Liu XH, Zhong L, Huang S, Mao SX, Zhu T, Huang JY. Size-dependent fracture of silicon nanoparticles during lithiation. *ACS Nano* (2012) **6**:1522–1531. doi:10.1021/nn204476h

11. McDowell MT, Lee SW, Harris JT, Korgel BA, Wang C, Nix WD, Cui Y. In situ TEM of two-phase lithiation of amorphous silicon nanospheres. *Nano Lett* (2013) **13**:758–764. doi:10.1021/nl3044508

12. Hummelgård M, Zhang R, Nilsson HE, Olin H. Electrical sintering of silver nanoparticle ink studied by In-situ TEM probing. *PLoS One* (2011) **6**:1–6. doi:10.1371/ journal. pone. 0017209

13. Woehl TJ, Park C, Evans JE, Arslan I, Ristenpart WD, Browning ND. Direct observation of aggregative nanoparticle growth: Kinetic modeling of the size distribution and growth rate. *Nano Lett* (2014) **14**:373–378. doi:10.1021/nl4043328

14. Jaramillo C, Ochoa D, Contreras L, Pagani M, Carvajal-ortiz H, Pratt LM, Krishnan S, Cardona A, Romero M, Quiroz L, et al. References and Notes 1. (2010) **321**:882–886. doi:10.1126/science.1229223

15. Xin HL, Pach EA, Diaz RE, Stach EA, Salmeron M, Zheng H. Revealing Correlation of Valence State with Structural Coarsening in Nanoporous Co / Silica Catalysts by in situ Environmental TEM and EELS. (2012) **18**:1116–1117. doi:10.1017/ S143192761200743X

16. Trudeau ML, Laul D, Veillette R, Serventi AM, Mauger A, Julien CM, Zaghib K. In situ high-resolution transmission electron microscopy synthesis observation of nanostructured carbon coated LiFePO4. *J Power Sources* (2011) **196**:7383–7394. doi:10.1016/j.jpowsour.2011.04.003

17. Ziegler A, Graafsma H, Zhang XF, Frenken JWM eds. *In-situ Materials Characterization Across Spatial and Temporal Scales*. Springer

18. Martin CA, Smit RHM, Egmond R Van, Van Der Zant HSJ, Van Ruitenbeek JM. A versatile low-temperature setup for the electrical characterization of single-molecule junctions. *Rev Sci Instrum* (2011) **82**: doi:10.1063/1.3593100

19. Introduction to Focused Ion Beams: Instrumentation, Theory, Techniques and Practice. Springer (2006).

CHAPTER 3

HIGH-CAPACITY AND HIGH-POWER BATTERIES USING ELECTRON MICROSCOPY

The ultimate aim of battery research is to develop a high-capacity battery that can deliver high power. This chapter summarizes our recent research on Li-ion, Na-ion, Li-S and Li-air batteries and the role of electron microscopy in such research. This research is performed in collaboration with different battery groups.

Understanding the key reason(s) behind battery performance—whether good or poor—is of utmost importance to utilize the full potential of a battery and to achieve further improvements. Electron microscopy enables simultaneous visualization and chemical and/or structural characterization at (sub)nanometer resolution. This chapter focuses on using SEM and TEM to identify the key factors that determine battery performance based on examples taken from our recent research on Li-ion, Na-ion, Li-S and Li-air batteries conducted at the TU Delft.

1. Lithium-ion batteries

Of all existing battery technologies, Li-ion batteries feature the best gravimetric and volumetric energy density. To further improve their cycle life, coulombic efficiency and to increase their energy and power density, researchers throughout the world are focusing on improving individual battery components, i.e. cathodes, anodes and electrolytes, using innovative materials synthesis techniques. The following sections summarize our contributions to developing a high-capacity retention, fast-rechargeable Li-ion battery.

1.1. Improving the reversible capacity of amorphous TiO_2 [i]

Owing to its low cost, ease of preparation and high theoretical capacity of 335 mAh g^{-1}, titanium dioxide (TiO_2) is a viable alternative to graphite as the anode material in Li-ion batteries. Even though the total energy density of the battery is reduced due to a high working potential of TiO_2 (1.5 V vs. Li/Li$^+$) compare to the graphite anode (~0 V vs. Li/Li$^+$), the advantage of absence of dendritic growth of Li (occurs at ~0 V vs. Li/Li$^+$) makes the battery safe [1–4].

Amorphous TiO_2 has been shown to possess a first discharge capacity that is about two and a half times higher than its theoretical maximum. However, it shows irreversible capacity loss during the first few battery cycles along with capacity fading during battery cycling. Its maximum reversible capacity of ~200 mAh g^{-1} is achieved at slow (dis)charge rates [5]. The loss of capacity during the first couple of cycles is largely attributed to degradation of the electrolyte on the electrode surface due to the presence of residual water or solvents. It appears very difficult to remove the surface-adsorbed water and solvent molecules from these high-surface-area titanium dioxides [6–8]. Although recent attempts to diminish this initial capacity

loss by using pre-lithiation to displace surface chemisorbed –OH groups by lithium appear to have been successful for TiO_2-(B) nanotubes, this treatment may prove to be challenging for larger-scale production [9]. In this study, we show that a judicious choice of preparation solvent and extended annealing at moderate temperatures in vacuum improves the capacity retention of amorphous TiO_2.

Sample preparation. First, the amorphous titania precursor is prepared by adding deionized water drop wise to a mixture of titanium isopropoxide and anhydrous acetone in an ice bath as described in Refs. [10,11]. The mixture is then washed several times with anhydrous acetone and stored overnight at 50°C. The amorphous TiO_2 samples are prepared by heating the pre-dried titania precursor in a vacuum tube at 80, 100 and 130°C for 4, 8 and 15 days, respectively. These samples will henceforth be referred to as A-TiO_2-80, A-TiO_2-100 and A-TiO_2-130. Another set of amorphous TiO_2 samples is made using a titania precursor prepared in ethanol described by Borghols and co-workers [5]. As before, this ethanol-based titania precursor is heated in the same environment to obtain E-TiO_2-80, E-TiO_2-100 and E-TiO_2-130.

To check the performance of the different TiO_2 samples, electrodes are prepared by mixing the TiO_2 powder with binder (Kynar Flex) and carbon black (Super P) in a weight ratio of 70:20:10 using NMP as a solvent. The mixture is subsequently casted on carbon-coated aluminum foil with a doctor blade. Circular pieces are cut out, compressed and then used in a battery, with lithium metal as the counter and reference electrode. The electrolyte is a 1M solution of $LiPF_6$ in EC:DMC (1:1). Electrochemical (dis)charge tests are performed with a MACCOR 5300 battery cycler.

Result and discussion. Representative TEM images for the A-TiO_2-130 and E-TiO_2-130 samples are shown in Figure 1. TEM images show that the aggregates of the E-TiO_2-130 particles are more porous than the A-TiO_2-130 particles. Moreover, the A-TiO_2-130 particles form larger and extremely spherical aggregates. All the electrodes prepared from different TiO_2 samples are (dis)charged galvanostatically within a range from 2.5 to 0.8 V at a rate of C/10, see Figure 2. The A-TiO_2-130 and E-TiO_2-130 samples both showed extremely high specific capacities of 860 and 1170 mAh g^{-1}, both of which are unprecedented for the amorphous TiO_2 polymorph [5]. The samples are annealed in vacuum at 100°C. A-TiO_2-100 and E-TiO_2-100 also feature high specific capacities after the first discharge at 790 and 800 mAh g^{-1}, respectively. This is comparable to what has been reported previously in the literature for amorphous TiO_2, corresponding to a composition of ~$Li_{2.4}TiO_2$. The samples are annealed to 80°C, and A-TiO_2-80 and E-TiO_2-80 achieved first

discharge capacities of 360 and 400 mAh g^{-1}, respectively, which is significantly lower than those of the samples annealed at higher temperatures. After 50 battery cycles, only A-TiO$_2$-130 and E-TiO$_2$-130 show an appreciable capacity retention of 220 and 240 mAh g^{-1}, respectively, the latter being the highest value observed for pristine amorphous TiO$_2$.
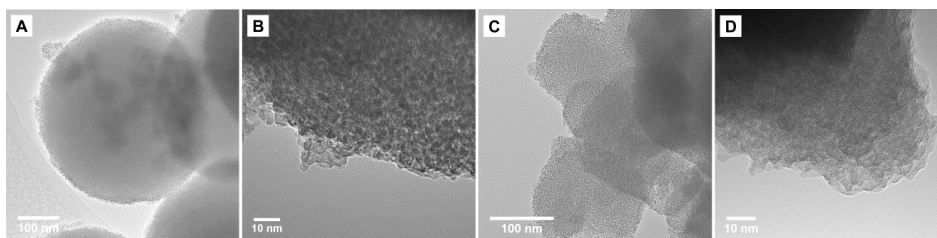
Figure 1. TEM images of amorphous TiO$_2$ samples (A, B) A-TiO$_2$-130 and (C, D) E-TiO$_2$-130.
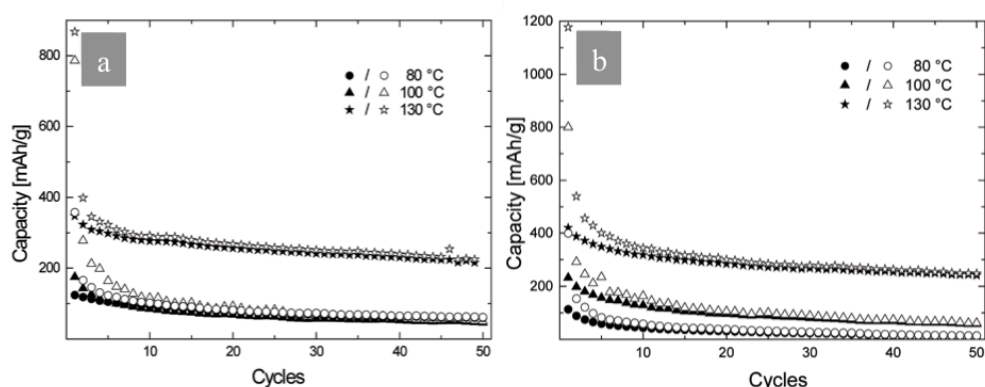
Figure 2. Capacity retention for samples prepared at different temperatures of (a) ethanol and (b) acetone for (dis)charge rates at C/10. Solid data points denote charge capacity whereas hollow points denote discharge capacity.

Fourier transform infrared (FTIR) spectroscopy measurements performed on all the amorphous samples show that heating the samples to 130°C in vacuum for a prolonged time is sufficient to remove all remnants of solvent molecules from the TiO$_2$ samples.[i] For samples prepared in acetone, chemisorbed solvent remained, even after being heated for several hours in vacuum at 130°C. For samples prepared in ethanol, heating above 100°C causes the chemisorbed ethanol species to oxide and form a carboxylate-containing species. Electron energy loss spectroscopy (EELS) measurements are performed to get a better indication of the amount of carbon in the TiO$_2$ samples prepared in ethanol. Background-subtracted carbon K edges are shown in Figure 3. Carbon-K edges of appreciable intensity are observed for the E-TiO$_2$-80 sample. Smaller C-K edge intensities for the E-TiO$_2$-100 sample and no C-K edge are observed for the E-TiO$_2$-130 material. This indicates the absence of molecular ethanol in E-TiO$_2$-130. Figure 3 shows that the amount of

surface carboxylate is very small; in fact, it is only visible in the bulk FTIR measurements.
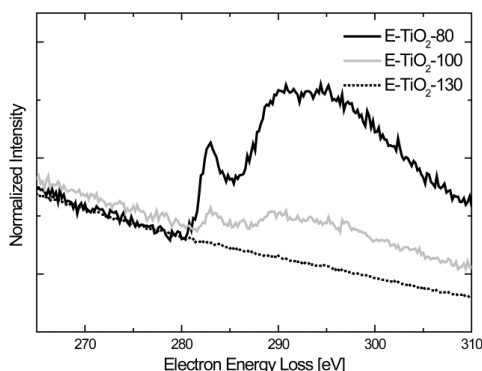
Figure 3. *EELS spectra of carbon K-edge of amorphous TiO$_2$ samples annealed in vacuum at various temperatures in ethanol.*

Conclusion. Amorphous TiO$_2$ prepared in acetone and ethanol with extended annealing in vacuum leads to a capacity retention of 220 and 240mAh g^{-1}, respectively, after 50 cycles. We found no residual solvent for the amorphous TiO$_2$ samples prepared in acetone. For the samples prepared in ethanol, the surface of the amorphous TiO$_2$ is partially functionalized by a small amount of residual functional groups coordinated to the oxygen-deficient surface that displaces the more reactive hydroxyl groups. We argue that this formation of a more stable SEI layer has a dramatic impact on the electrochemistry of nanostructured battery electrodes, allowing the reversible capacity to be increased by up to 20%. The results presented here provide a simple and effective strategy to improve the performance of high-surface-area transition-metal oxides.

1.2. High-performance Si anode from direct deposition[ii]

Owing to a theoretical capacity of 4200 mAh g^{-1}, Si is considered to be the next-generation anode material for Li-ion batteries [12]. However, electrode pulverization due to the huge volume change resulting from lithium-ion insertion leads to a loss of electrical connection and thus a rapid loss of capacity retention [13–15]. Various kinds of nanostructured Si materials such as nanowires, nanotubes, and nanospheres in a flexible reduce electrode pulverization [16–20]. However, large-scale production, i.e. commercialization, appears to be challenging, especially considering the low mass loading of Si (<0.5 mg cm^{-2}) [21–23].

[ii] *This section is based on* **"A High-performance Li-ion Anode from Direct Deposition of Si Nanoparticles,",** *Yaolin Xu, Ellie Swaans, Sibo Chen, Shibabrata Basak, Peter-Paul R.M.L. Harks, Bo Peng, Dana Borsa, Fokko M. Mulder, Nano Energy (Submitted).*

In this study, the Si anode is prepared using a novel but simple and industrially scalable plasma-enhanced chemical vapour deposition (PECVD) technique with high active mass loading.

Sample preparation. Silicon nanoparticles (NP) are deposited directly on a porous carbon substrate with no additional carbon or binder by means of an expanding thermal plasma (ETP) PECVD process. Silicon nuclei are formed and agglomerated into nanoparticles and eventually clusters of particles before they reach the substrate. A detailed description can be found in the article [ii].

The performance of the as-deposited Si anodes are tested with a lithium-metal foil (Aldrich) as the counter electrode. 1M $LiPF_6$ salt dissolved in a mixture of ethylene carbonate (EC), diethyl carbonate (DEC) and fluoroethylene carbonate (FEC) (1:1:1 in volume) acted as the electrolyte. Electrochemical performance is measured with a MACCOR 4600 battery cycler at room temperature.

Results and discussion. SEM images (Figures 4a–c) illustrate the hierarchically multi-branched porous nanostructure of the deposition layers. The resulting porosity provides an expressway for electrolyte intrusion and thus for accelerated Li-ion transport throughout the electrode in addition to accommodating the volume expansion during Li-ion insertion. TEM images (Figures 4d–f) demonstrates that clusters are composed of individual particles about ~20 nm in size. Particles are crystalline and nicely spherical in shape with a very thin native SiO_x layer on the surface. As CVD-based Si deposition is already widespread at the industrial level for producing microelectronics and solar cells, the necessary infrastructure is already in place for large-scale production.

The Si electrode with a Si mass loading of 0.5 mg cm^{-2} at 0.1 A g^{-1} shows a highly stable reversible capacity after the initial (dis)charge, see Figure 5. After 30 battery cycles, we obtained a capacity of 1825 mAh g^{-1}, which corresponds to a Coulombic efficiency of ~90% as indicated in Figure 5. Considering the amount of SiO_x present in the sample according to a Raman study, the capacity of Si NPs will be in remarkably good agreement with theoretical values. Further details about the high capacity retention and superior rate capability at different mass loading can be found in Ref. [ii].

We attribute the excellent performance of the Si NP electrode to the stable SEI formation. The addition of fluoroethylene carbonate (FEC) to the electrolyte has proved to be advantageous because it creates a compact and stable LiF-dominant SEI layer that limits the further formation of SEI [24–26]. It is anticipated that a SEI layer will form on the exposed surface of the individual Si NPs during the first Li-

ion insertion. As shown in Figures 6b–g, the SEI-covered Si NP clusters after 100 cycles appear to remain the same typical size as after the first cycle, and the microstructure of the electrode is preserved throughout the cycling. Therefore, after
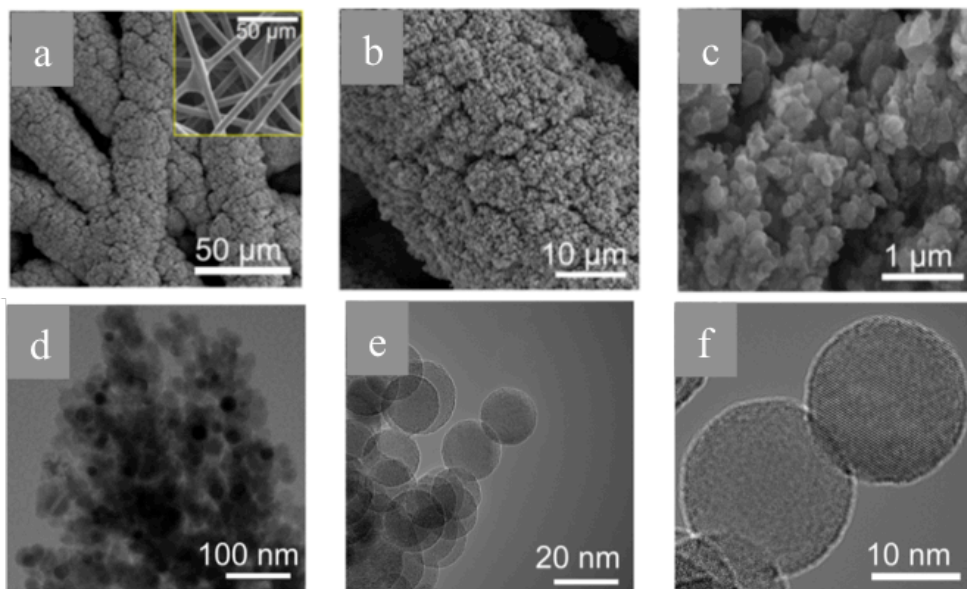
Figure 4. *Morphology of as-synthesized Si NP on a porous C substrate. (a) - (c) SEM micrographs of the nanostructured Si layer imaged at different magnifications; inset of (a): SEM micrograph of the porous C fiber sheet. (d) - (f) TEM image of as-synthesised Si nanoparticle cluster and individual particles.*
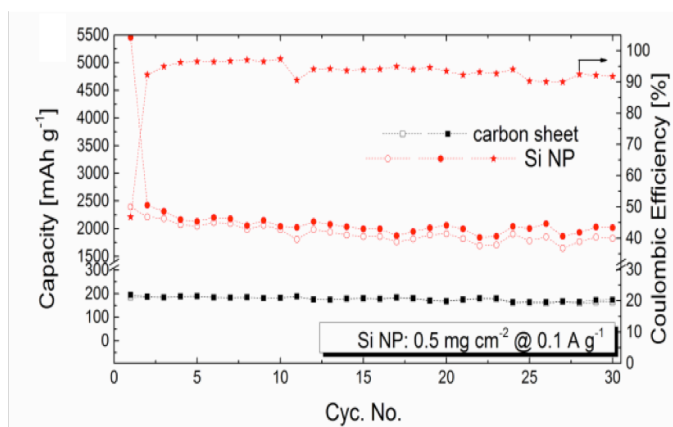
Figure 5. *Electrochemical performance of Si NP electrode with mass loading of 0.5 mg cm^{-2} at 0.1 A g^{-1} over 30 battery cycles. The calculated Coulombic efficiency of the electrode is also shown. The performance of a carbon substrate using exactly the same system and parameters is shown for comparison.*
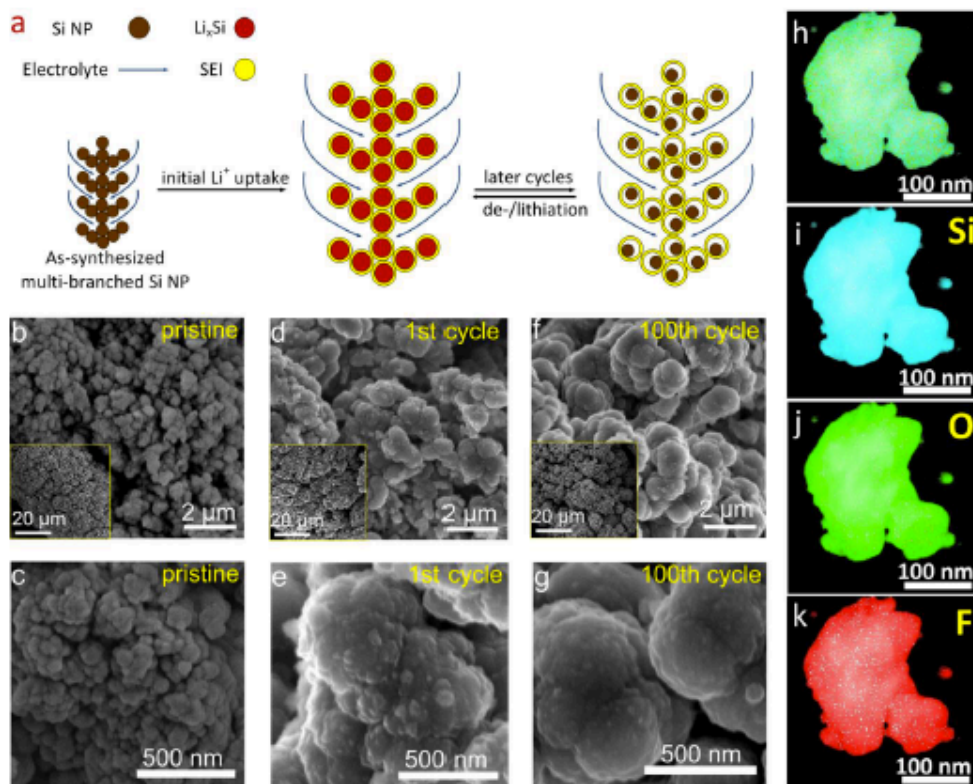
Figure 6. *Morphology of Si NP electrodes at three different stages: pristine, after first cycle and after 100th cycle cycling at 0.8 A g^{-1}. (a) Schematic of the morphology change. (b) - (g) SEM images showing Si NP at different stages: (b) - (c): pristine; (d) - (e): after first cycle; (f) - (g): after 100th cycle; (h) - (k): STEM-EDX result: layered image and element mapping of Si, O and F, respectively, on electrode after 100 battery cycles.*

the rigid protective SEI is formed, it apparently stays largely intact during later cycles, and the volume change of individual particles is accommodated by the space available between individual particles and their SEI. In this way, the contact throughout the electrode is not destroyed, as illustrated in Figure 6a. The uniform growth of the SEI layer can be seen in the similar distribution of the F element (mostly from LiF in the SEI layer), with Si and O elements spreading throughout the NP clusters, see Figures 6h–k.

Conclusions. The binder/carbon-free Si NP anode synthesized via a noble PECVD process is a particularly rapid and scalable method to synthesize Si anodes of Li-ion batteries. Excellent cycling stability results from the formation of locally protective SEI on individual nanoparticles throughout the electrode. This not only reinforces

the mechanical strength of single particles as well as the entire electrode, it also protects the electrode from pulverization.

1.3. Li$_6$PS$_5$Br solid electrolyte for fast Li-ion transport [iii]

Solid electrolytes are currently attracting considerable attention because of their excellent chemical and physical stability, wide voltage window and non-flammability [27,28]. However, one of the main obstacles impeding the development of solid-state batteries is the low Li-ion conductivity of solid electrolytes at room temperature [29,30].

An important family of sulfide-based solid electrolytes are the Li$_6$PS$_5$$X$ (X=Cl, Br and I) that provide Li-ion conductivities in the range of $10^{-2} - 10^{-3}$ S cm^{-1} at room temperature [31]. The high conductivity and low cost of the basic materials makes them promising candidates for solid-state batteries.

In this study, we show the effect of annealing on increasing the Li-ion conductivity of Li$_6$PS$_5$Br.

Sample preparation. Li$_6$PS$_5$Br is synthesized by mechanical milling. Briefly, a stoichiometric amount of Li$_2$S, P$_2$S$_5$ and LiBr powders (all obtained from Sigma-Aldrich) are ball-milled under argon atmosphere at 500 rpm. After the ball-milling process, half the sample is set aside and hereafter referred to as BM-Li$_6$PS$_5$Br. The rest is sealed in a quartz tube, annealed at 300$^{\mathrm{o}}$C for 5 hours, and then ball-milled again to obtain a different set of electrolytes hereafter referred to as AN-Li$_6$PS$_5$Br.

These solid electrolytes are tested in Li$_2$S/Li$_6$PS$_5$Br/In batteries at a current density of 0.064 mA cm^{-2} between 0 and 3.5 V vs. In (i.e., 0.62–4.12 V vs. Li/Li$^+$).

Results and discussion. From our AC impedance measurements[iii] with BM-Li$_6$PS$_5$Br and AN-Li$_6$PS$_5$Br, we found that the bulk conductivities of BM-Li$_6$PS$_5$Br and AN-Li$_6$PS$_5$Br are roughly the same, whereas the grain boundary conductivity improves by 3 orders of magnitude due to annealing.

Figures 7a and 7c are BF-TEM images of BM-Li$_6$PS$_5$Br and AN-Li$_6$PS$_5$Br, respectively, and Figures 7b and d show the corresponding diffraction patterns. The presence of a ring-like diffraction pattern of the BM-Li$_6$PS$_5$Br sample reveals its polycrystalline nature. Further annealing and milling increases the grain size of the sample, making it more crystalline, as can be derived from the well-crystalline

---

[iii] *This section is based on **"Revealing the annealing effects on Li-ion mobility in Li$_6$PS$_5$Br solid electrolyte synthesized by mechanical milling route,"** Chuang Yu, Swapna Ganapathy, Ernst R.H. van Eck, Shibabrata Basak, Henny W. Zandbergen, Marnix Wagemaker (in preparation).*

nature of the diffraction pattern shown in Figure 7d. We argue that the decrease in grain boundary resistance may be a consequence of the increase in the crystallinity of the AN-Li_6PS_5Br sample compared to that of BM-Li_6PS_5Br. The STEM-EDX mapping of the BM-Li_6PS_5Br sample shown in Figure 7f shows a uniform distribution of S, P and Br, which indicates a homogeneous distribution of the elements in the prepared Li_6PS_5Br electrolyte.
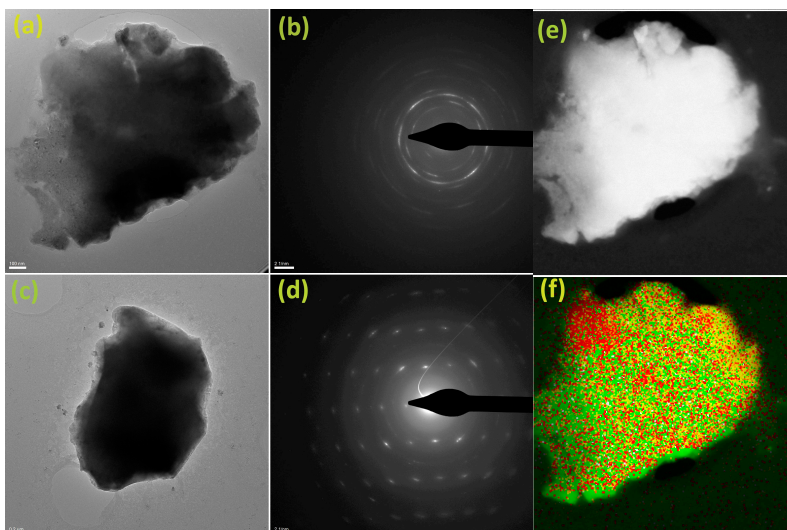
Figure 7: *Bright-field TEM images (scale bar is 100 nm) and their corresponding diffraction patterns for (a, b) BM-Li_6PS_5Br and (c, d) AN-Li_6PS_5Br). (e, f) STEM image and EDX mapping of the BM-Li_6PS_5Br sample. The yellow, green and red dots represent the distribution of S (red), Br(yellow), and P (green) respectively.*
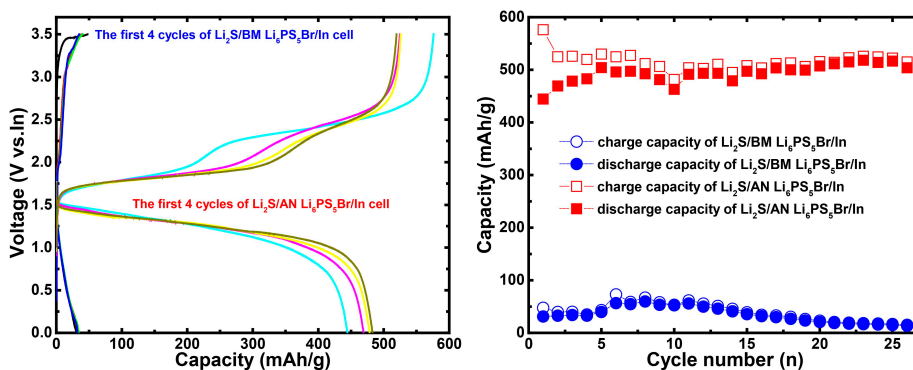
Figure 8. *(a) Comparison of the first four cycles of the assembled Li_2S/Li_6PS_5Br (BM and AN)/In solid-state batteries at a current density of 0.064 mA cm^{-2} applied between 0 and 3.5 V vs. In. (b) Comparison of capacity retention with the two different solid electrolytes.*

In Figure 8a, the (dis)charge curves of the first four cycles showed no obvious (dis)charge plateau and a very low discharge capacity of less than 50 mAh g^{-1} for

the solid-state cell using BM-Li_6PS_5Br. In contrast, the charge curve of the solid-state cell with an AN-Li_6PS_5Br solid electrolyte produced two distinct charge plateaus located at 1.8 and 2.3 V vs. In and a discharge plateau at 1.4 V vs. In. Moreover, the solid-state cell with AN-Li_6PS_5Br showed a much higher initial discharge capacity of 450 mAh g^{-1}. The superior performance of AN-Li_6PS_5Br can further be seen in Figure 8b. After 25 cycles, the discharge capacity with the AN-Li_6PS_5Br electrolyte shows a stable value of 500 mAh g^{-1}. In sharp contrast, the solid-state battery using BM-Li_6PS_5Br as a solid electrolyte shows a very poor discharge capacity: After 20 cycles, the discharge capacity almost goes to zero.

Conclusion. A fast lithium-ion conductor Li_6PS_5Br is successfully synthesized by direct mechanical milling. Superior electrochemical performances with AN-Li_6PS_5Br as electrolyte are due to improved grain boundary conductivity resulting from increased sample crystallinity.

2. Na-ion batteries

Owing to the analogy between Li and Na ions, different types of materials that have been applied in Li-ion batteries are also candidates for application in Na-ion batteries [32–34]. Thus, based on Si as a promising anode material for Li-ion batteries, research interest has also been focused on Si as an anode for Na-ion batteries. With a theoretical capacity of 954 mAh g^{-1}, Si can be a very suitable material for Na-ion battery anodes. Until now, however, reversible sodium insertion has been unsuccessful [35,36].

2.1. Reversible Na-ion uptake in Si nanoparticles [iv]

Anticipating the advantage of nanoscaling for the kinetics of ion insertion and extraction, and considering the fact that amorphous Si is more favorable for Na insertion, we have studied much smaller Si particles (~20 nm) containing a large proportion of amorphous Si obtained via expanding thermal plasma chemical vapor deposition (ETPCVD) of silane [37–40]. To our knowledge, this is the first time reversible Na-ion uptake in Si has been achieved experimentally for a significant capacity.

Sample preparation. Electrodes are prepared using a slurry created by mixing Si nanoparticles obtained from ETPCVD, a sodium carboxymethyl cellulose binder

---

[iv] *This section is based on "**Reversible Na-ion uptake in Si nanoparticles,**" Yaolin Xu, Ellie van Swaans, Shibabrata Basak, Henny W. Zandbergen, Dana Borsa, Fokko Mulder, Adv. Energy Mater. 2016, 6, 1501436.*

(NaCMC) (Aldrich) and Super P-conductive carbon black in a weight ratio of 5:3:2 in deionized water. The well-mixed slurry is casted onto a Cu foil (Goodfellow) with a doctor blade, then dried in a vacuum oven and rolled with a compressor for good electronic contact.

The electrodes are tested with a Na metal foil as counter electrode. 1M $NaClO_4$ dissolved in ethylene carbonate (EC) and propylene carbonate (PC) (1:1 in volume) is used as the electrolyte. Electrochemical performance is measured with a MACCOR 5300 battery cycler.

Results and discussion. Figure 9a shows bundles of Si nanoparticle clusters having treelike morphology with micron-sized fiber branches consisting of small nanoparticles. Figure 9b demonstrates the presence of crystalline as well as amorphous Si particles. Both appear to be nicely spherical. The crystalline Si particle has an oxidized surface layer due to air exposure. Raman measurements show that the amount of amorphous Si is significant (c-Si: a-Si = 0.39: 0.61) [iv].
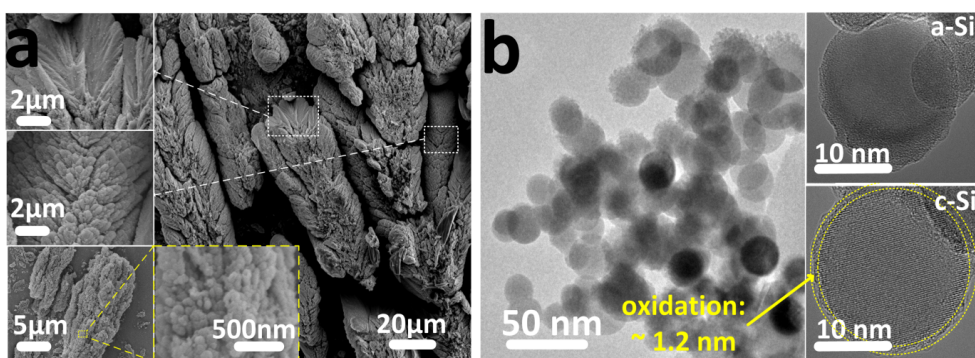

Figure 9. (a) SEM images of Si nanoparticle clusters. (b) TEM images of Si nanoparticles.
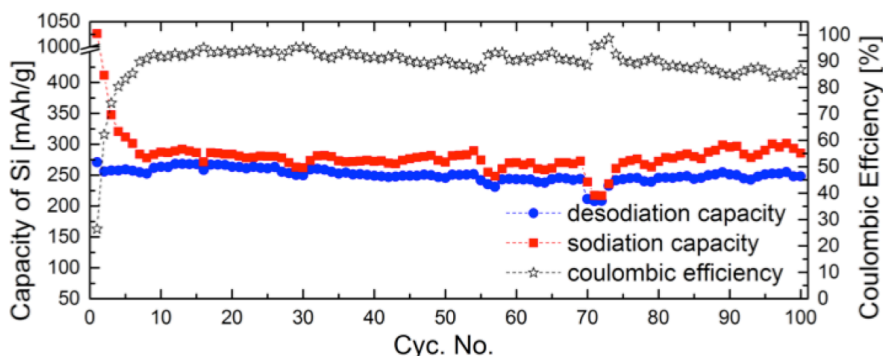
Figure 10. Capacity retention and Coulombic efficiency of the Si electrode at 20 mAg^{-1}.

Figure 10 demonstrates an initial sodiation capacity of 1027 mAh g^{-1} for Si at 20 mAg^{-1}, which is higher than the theoretical capacity of 954 mAh g^{-1} for NaSi. A

large part of this initial capacity is attributed to the irreversible formation of a solid electrolyte interface (SEI) layer on the surface of Si. The subsequent Na-ion extraction process achieves a capacity of up to 270 mAh g^{-1}, indicating that a significant proportion of Na is stored reversibly, in addition to the large irreversible part. The Coulombic efficiency of the electrode for up to 100 battery cycles remains at around 90%. Further details on the performance of the Si electrodes can be found in the article [iv].

Conclusion. The Si electrode prepared using ETPCVD produced a sample containing both amorphous and crystalline Si nanoparticles that demonstrate an excellent capacity retention of 248 mAh g^{-1} after 100 cycles at 20 mAh g^{-1}, which is the report of sizeable reversible Na uptake in a Na-ion battery.

3. Li-S batteries

As next-generation energy storage materials, lithium-sulfur (Li-S) batteries have become increasingly attractive owing to their high gravimetric density of 2600 Whk g^{-1} and specific capacity of 1671 mAh g^{-1}. In addition, sulfur is a highly cost-effective and environmentally benign element [41]. However, the overall performance of current Li-S batteries is impeded by the inherently poor electronic and ionic conductivity of sulfur and the dissolution of higher-order polysulphides phases (Li$_2$S$_n$, where $8 \geq n \geq 2$) during cycling, which causes irreversible loss of active material.

3.1. Graphene-graphene oxide-based cathodes for Li-S batteries[v]

Here we report binder-free, 3-D, vertically aligned, few-layered graphene (FLG) electrodes filled with partially reduced graphene oxide-sulfur nanocomposites (PrGO/S) for high-performance Li-S batteries. This cathode provides several key advantages over conventional 2-D planar electrode morphology: (i) improved electrical conductivity and high sulfur loading in the interconnected microporous FLG network, (ii) ease of electrolyte accessibility owing to its highly interconnected nature and (iii) uniform distribution of micro/macropores confining the polysulfide shuttle within the cathode matrix and improving the active material utilization [42].

Sample preparation. Details of the cathode fabrication can be found in the article[v]. In short, predetermined amounts of sulfur (Sigma Aldrich) and partially reduced

---

[v] *This section is based on "3-D Vertically Aligned Few Layer Graphene – Partially Reduced Graphene Oxide/Sulfur Electrodes for High Performance Li-Sulfur Batteries," D.P. Singh, N. Soin, S. Sharma, S. Basak, S. Sachdeva, P. Gonugunta, S.S. Roy, H.W. Zandbergen, J.A. McLaughlin, M. Huijben, and M. Wagemaker, Advanced Materials Interfaces (Submitted).*

GO powders are mixed in toluene and ball-milled in an argon atmosphere for 60 to 90 minutes to obtain a homogeneous mixture. The mixture is then melt-infiltrated at $130^{\circ}C$ in an argon atmosphere, and the PrGo/S is subsequently drop-cast on vertically aligned FLG.

Results and discussion. The elemental mapping of PrGO/S composites revealed a homogeneous dispersion of sulfur on the PrGO sheets. Owing to the melt-infiltration process to synthesize 3-D FLG/PrGO-S, a thin layer of sulfur nanoparticles as well as larger discrete particles are observed embedded in the matrix, as evident from the elemental mapping in Figure 11.
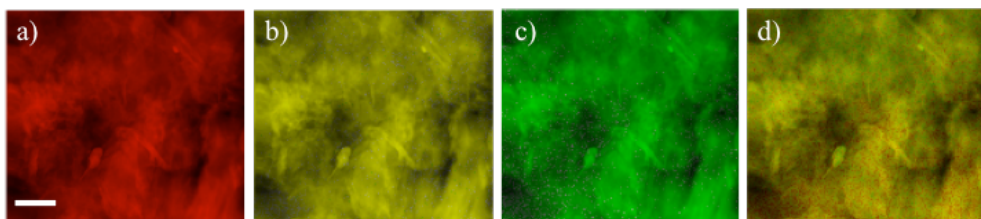
Figure 11. *The elemental maps of (a) C (b) S (c) O and (d) overlay show a uniform distribution of sulfur for PrGO/S. The scale bar represents 100nm.*
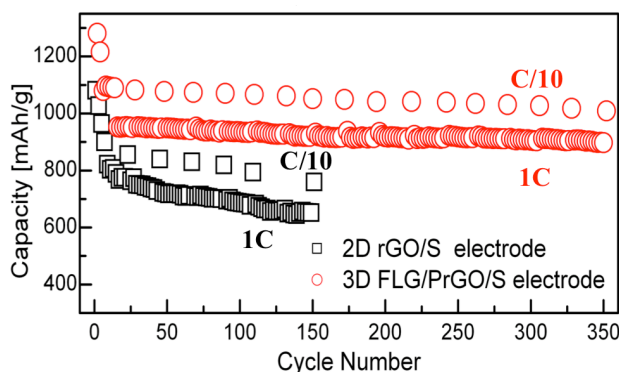
Figure 12: *Lifecycle profile of 2-D PrGO/S and 3-D FLG/PrGO-S electrodes at C/10 and 1C rates.*

To elucidate the performance-enhancing role of the 3-D electrodes, the discharge performance is compared with the PrGO/S composites with equivalent sulfur loading (~80 wt%). The PrGO/S electrode showed an initial discharge capacity of 1080 mAh g^{-1} at a rate of C/10 compared to an initial value of 1280 mAh g^{-1} for the 3D FLG/PrGO/S electrode (Figure 12). However, the capacity continued to drop after subsequent cycles, suggesting the dissolution of soluble Li-polysulfides in the liquid electrolyte, which 3D FLG/PrGO/S electrode can deliver ~900mAh g^{-1} after same number of cycles. This significant better performance of 3-D FLG/PrGO-S electrodes compare to planar PrGO/S electrodes suggest that the 3-D microstructure with interconnected ionic and electronic transport pathways lowers the overall

charge transport resistance and facilitates excellent electrical and ionic transport in the entire electrode matrix [44–46]. The higher rate performance of the cathode is described in detail in ref. [v].

Conclusion. Using multifunctional composites with 3-D architectures, we are able to achieve electronic and ionic conductivity, facilitate electrolyte accessibility and confine the polysulfide shuttle within the matrix. This leads to excellent cycling capabilities and capacity of Li-S batteries.

4. Li-air batteries

The prospect of using Li-O_2 systems to replace gasoline for automotive applications has thrust battery research into the limelight [47,48]. However, there are several fundamental obstacles to be overcome before this battery system can work effectively. These include the high overpotentials observed during (dis)charge that lead to low cycle energy efficiency, slow kinetics due to poor electronic and ionic conductivity, and several side reactions involving the electrolyte and electrodes that result in poor cyclability [49–52]. Even if a stable electrolyte is found, capacity fading will occur due to the incomplete oxidation of Li_2O_2 upon charging, which is a consequence of the poor ionic and electronic conduction of Li_2O_2 [53]. The progressive buildup of inactive Li_2O_2 during repeated battery cycles, in addition to byproduct accumulation, eventually causes cell failure. The main factors influencing Li_2O_2 morphology, and hence cell capacity, are the current density and the solubility of the LiO_2 intermediate [54,55]. Poor LiO_2 solubility by the electrolyte, i.e. low donor numbers, promotes the formation of a passivating Li_2O_2 film, which is even more pronounced for high current densities, leading to early cell death [55].

4.1. Using nanoseed crystals to control peroxide morphology [vi]

A potential approach to mitigate the passivating formation of an amorphous Li_2O_2 film at high rates is to promote the formation of nano-sized Li_2O_2 crystallites at the electrode surface. A method to control the grain size and prevent agglomeration is to add grain-refining agents, as is frequently done in metallurgy [56]. Grain refinement involves adding particles that act as substrates or seeds for heterogeneous nucleation, and that also promote equiaxed grain formation, which in the case of alloying can compete with dendritic crystal nucleation and growth [56].

[vi] *This section is based on **"The Use of Nano Seed Crystals to Control Peroxide Morphology in a Non-Aqueous Li-O_2 Battery,"** Swapna Ganapathy, Zhaolong Li, Maria S. Anastasaki, Shibabrata Basak, Xue-Fei Miao, Kees Goubitz, Henny W. Zandbergen, Fokko M. Mulder and Marnix Wagemaker, Journal of Physical Chemistry C, 120, 33, 18421-18427 (2016).*

Mesoporous NiO sheets in their cubic crystalline form have already been demonstrated to work as a non-noble-metal-based catalyst for Li-O$_2$ battery systems to promote the decomposition of Li$_2$CO$_3$ [57,58]. Interestingly, NiO in its hexagonal form is structurally similar to Li$_2$O$_2$ and has an a,b-lattice parameter (2.973 Å) close to that of Li$_2$O$_2$ (3.135 Å). This makes hexagonal NiO an attractive candidate for grain refiner for Li$_2$O$_2$ in Li-O$_2$ batteries.

Sample preparation. Gas diffusion electrodes are prepared by mixing activated carbon (AC) and NiO (Figure 13) nanoparticles having AC:NiO weight ratios of 95:5 (AC-NiO-1) and 33.3:66.6 (AC-NiO-2), respectively, or only AC and a lithiated Nafion® binder having a weight ratio of 90:10 for AC-NiO/AC:binder and subsequently cast on carbon paper (Spectracarb 2050a). These gas diffusion electrodes are then dried in vacuum at 100°C for 24 h to remove all traces of surface-adsorbed water before the disks are punched.
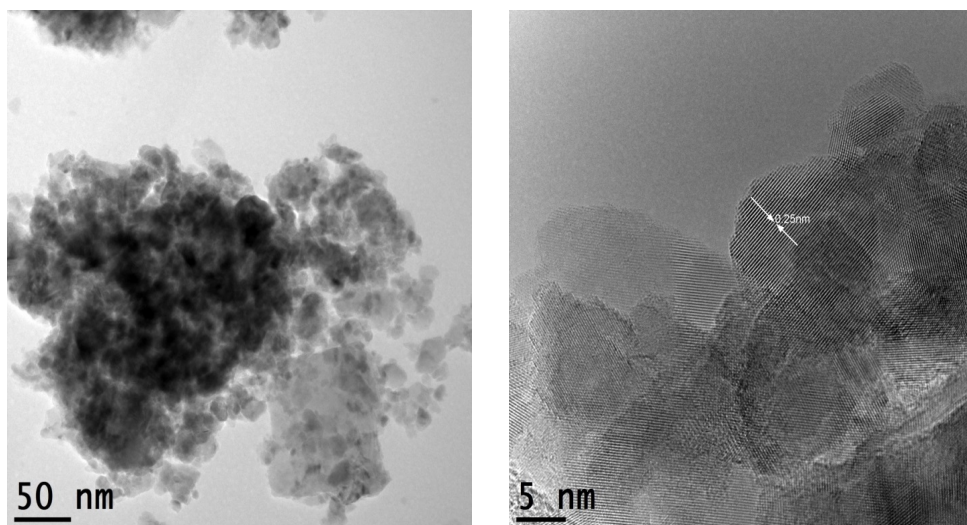
Figure 13: TEM images show an agglomerate of NiO nanoparticles in different magnifications. HRTEM image indicates the hexagonal {10-10}/{1-100} d spacing.

Batteries comprising a cathode, a glass microfiber (Whatman) soaked with electrolyte and a Li-metal anode are assembled in a glove box (Argon, O$_2$ and H$_2$O <0.1 ppm) in our home-built cells for non-aqueous Li-O$_2$ batteries. 1M lithium bis(trifluoromethanesulfonyl)imide (LiTFSI, Aldrich) dissolved in dried and distilled tetraethylene glycol dimethyl ether (TEGDME <5 ppm H$_2$O, Aldrich) acts as the electrolyte. Once connected to O$_2$ (Linde, 99.995%), the cell is allowed to equilibrate for 2–6 h under an O$_2$ pressure of 1.2 bar. Galvanostatic (dis)charge cycles are performed using a MACCOR 5300 battery cycler.

Results and discussion. The evolution of the a,b-lattice parameters of Li_2O_2, shown in Figure 14a, is distinctly different for the AC-NiO-1 and AC electrodes during Li_2O_2 formation and subsequent decomposition. The Li_2O_2 that formed on the AC-NiO-1 electrode during the initial stages of discharge results in an a,b-lattice parameter that started at 3.074±0.004 Å and further increased to 3.129±0.001 Å at the end of discharge. In contrast to this, the a,b values of Li_2O_2 that forms on the AC electrode start at 3.143±0.002 Å and decrease to 3.136±0.0004 Å at the end of discharge, as revealed by operando XRD measurements.
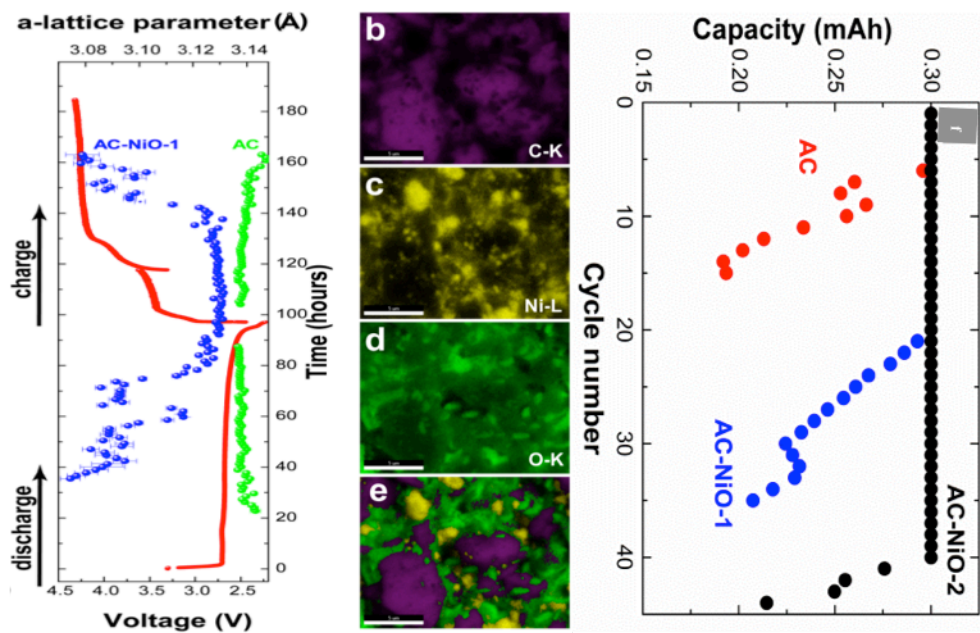
Figure 14. *(a) Evolution of the Li_2O_2 a,b-lattice parameter in the AC-NiO-1 cathode as a function of (dis)charge time. The evolution of the Li_2O_2 a,b-lattice parameter in the AC electrode is shown at the same capacity. (b)-(e) SEM-EDX elemental mapping of a region of an AC-NiO-2 electrode, completely discharged at a current density of 50 μA cm^{-2} to 2.2 V cutoff, showing maps of (b) C (c) Ni (d) O and (e) overlaid with purple = C; yellow = Ni; and green = O. The scale bar corresponds to 5 μm. (f) Restricted capacity cycling performance of AC-NiO-1/2 and AC electrodes at a current density of 100 μA cm^{-2}. The cutoff capacity is set to 0.3 mAh cm^{-2}.*

The smaller lattice parameters of peroxide that initially formed on the AC-NiO-1 electrodes can be attributed to the epitaxial growth of Li_2O_2 on NiO nanoparticles (a,b-lattice parameters 2.973 Å). As the discharge proceeds, Li_2O_2 particles grow and the a,b-lattice parameters tends to the bulk Li_2O_2. Furthermore, the deviation of the average a,b lattice parameters of the electrochemically formed Li_2O_2 in AC-NiO-1 and AC unambiguously proves that the majority of Li_2O_2 formation takes place on the NiO particles.

To visualize Li_2O_2 on the surface of an electrode consisting of NiO at the end of discharge, scanning electron microscopy with energy-dispersive X-ray spectroscopy (SEM-EDX) is performed on electrodes of AC-NiO-2. The high NiO content of this sample makes it easier to see the dispersed NiO and yields elemental maps, see Figures 14b–e of the carbon and oxygen K edges and the nickel L edge. As can clearly be seen in Figure 14e, the oxygen from Li_2O_2 is preferentially found on the parts of the electrode where Ni is present, whereas the area of the electrode consisting predominantly of C remains mostly uncovered.

Note that all Ni in Figure 14e should be considered NiO because oxygen are present in the same area in the elemental map, see Figure 14d. The apparent variation in Ni/O intensity indicates that Li_2O_2 does not cover the complete NiO surface and, consequentially, the uncovered NiO surface will appear to have a larger Ni/O ratio than the Li_2O_2-covered NiO.

Figure 14f compares the electrochemical performance of AC, AC-NiO-1 and AC-NiO-2 electrodes. Upon restricted capacity cycling (0.3 mAh cm^{-2}), the AC-NiO-1 electrode completely regains its discharge capacity on charge for more than 20 cycles, whereas the AC-NiO-2 electrode retains its capacity for 40 cycles. We anticipate that the improved cycling stability we observed is due to the epitaxial formation of Li_2O_2 on NiO, which suppresses the formation of any passivating thin Li_2O_2 film and keeps the Li_2O_2 crystallites smaller, both of which promote reversibility. As more NiO is present in the AC-NiO-2 electrodes, relatively more Li_2O_2 will form on NiO, which explains the better cycling performance when more NiO is present, although in practice this will compromise the energy density.

Conclusion. The observed average changes in the Li_2O_2 lattice parameters suggest that a relatively large proportion of the Li_2O_2 formed upon discharge is affected by NiO, which increases battery capacity and prolongs cycle life. Therefore, the presented grain-refining strategy calls for further research into materials that can act as seed crystals while catalysing the Li-air redox reactions, preventing side reactions and achieving good electronic conductivity.

References

1.   Wagemaker M, Mulder FM. Properties and promises of nanosized insertion materials for li-ion batteries. *Acc Chem Res* (2013) **46**:1206–1215. doi:10.1021/ar2001793

2.   Yang Z, Choi D, Kerisit S, Rosso KM, Wang D, Zhang J, Graff G, Liu J. Nanostructures and lithium electrochemical reactivity of lithium titanites and titanium oxides: A review. *J Power Sources* (2009) **192**:588–598. doi:10.1016/j.jpowsour.2009.02.038

3.   Kyeremateng NA, Dumur F, Knauth P, Pecquenard B, Djenizian T. Electropolymerization of

copolymer electrolyte into titania nanotube electrodes for high-performance 3D microbatteries. *Electrochem commun* (2011) **13**:894–897. doi:10.1016/j.elecom.2011.03.026

4.   Plylahan N, Kyeremateng NA, Eyraud M, Dumur F, Martinez H, Santinacci L, Knauth P, Djenizian T. Highly conformal electrodeposition of copolymer electrolytes into titania nanotubes for 3D li-ion batteries. *Nanoscale Res Lett* (2012) **7**:1–11. doi:10.1186/1556-276X-7-349\r10.1016/j.crci.2012.05.002; Perre, E., Taberna, P.L., Mazouzi, D., Poizot, P., Gustafsson, T., Edström, K., Simon, P., Electrodeposited Cu(2)Sb as anode material for 3-dimensional Li-ion microbatteries (2010) J Mater Res, 25, pp. 1485-1491; Gelloz, B., Mentek, R., Djenizian, T., Dumur, F., Jin, L., Koshida, N., Electropolymerization of poly(para-phenylene)vinylene films onto and inside porous Si layers of different types and morphologies (2010) J Electrochem Soc, 157, pp

5.   Borghols WJH, Lützenkirchen-Hecht D, Haake U, Chan W, Lafont U, Kelder EM, van Eck ERH, Kentgens APM, Mulder FM, Wagemaker M. Lithium Storage in Amorphous TiO_2 Nanoparticles. *J Electrochem Soc* (2010) **157**:A582. doi:10.1149/1.3332806

6.   Diebold U. The surface science of titanium dioxide. *Surf Sci Rep* (2003) **48**:53–229. doi:10.1016/S0167-5729(02)00100-0

7.   Bradley DC, Thomas IM. View Article Online / Journal Homepage / Table of Contents for this issue. *J Chem Soc* (1960)3857–3861. doi:10.1039/B813328J/Analyst

8.   Hadjiivanov KI, Klissurski DG. Surface chemistry of titania (anatase) and titania-supported catalysts. *Chem Soc Rev* (1996) **25**:61. doi:10.1039/cs9962500061

9.   Brutti S, Gentili V, Menard H, Scrosati B, Bruce PG. TiO 2-(B) nanotubes as anodes for lithium batteries: Origin and mitigation of irreversible capacity. *Adv Energy Mater* (2012) **2**:322–327. doi:10.1002/aenm.201100492

10.   Sudant G, Baudrin E, Larcher D, Tarascon J-M. Electrochemical lithium reactivity with nanotextured anatase-type TiO2. *J Mater Chem* (2005)1263–1269. doi:10.1039/b416176a

11.   Livage J, Henry M, Sanchez C. Sol-gel chemistry of transition metal oxides. *Prog Solid State Chem* (1988) **18**:259–341. doi:10.1016/0079-6786(88)90005-2

12.   Boukamp B a., Journal T, Weeks MC, Voss E, Yoshizawa S, Okada S, Mathieson RT, Press P, Jones EL, Papazov G, et al. All-Solid Lithium Electrodes with Mixed-Conductor Matrix. *J Electrochem Soc* (1981) **128**:725. doi:10.1149/1.2127495

13.   Obrovac MN, Christensen L, Le DB, Dahn JR. Alloy Design for Lithium-Ion Battery Anodes. *J Electrochem Soc* (2007) **154**:A849. doi:10.1149/1.2752985

14.   Larcher D, Beattie S, Morcrette M, Edström K, Jumas J-C, Tarascon J-M. Recent findings and prospects in the field of pure metals as negative electrodes for Li-ion batteries. *J Mater Chem* (2007) **17**:3759. doi:10.1039/b705421c

15.   Obrovac MN, Christensen L. Structural Changes in Silicon Anodes during Lithium Insertion/Extraction. *Electrochem Solid-State Lett* (2004) **7**:A93–A96. doi:10.1149/1.1652421

16.   Chan CK, McIlwrath K, Huggins RA. High-performance lithium battery anodes using silicon nanowires. *Nat Nanotechnol* (2008) **3**:31–35. doi:10.1038/nnano.2007.411

17.   Jeong S, Lee JP, Ko M, Kim G, Park S, Cho J. Etched graphite with internally grown si nanowires from pores as an anode for high density Li-ion batteries. *Nano Lett* (2013) **13**:3403–3407. doi:10.1021/nl401836c

18.   Cui LF, Ruffo R, Chan CK, Peng H, Cui Y. Crystalline-amorphous core-shell silicon nanowires for high capacity and high current battery electrodes. *Nano Lett* (2009) **9**:491–495. doi:10.1021/nl8036323

19.   Yao Y, McDowell MT, Ryu I, Wu H, Liu N, Hu L, Nix WD, Cui Y. Interconnected silicon hollow nanospheres for lithium-ion battery anodes with long cycle life. *Nano Lett* (2011) **11**:2949–2954. doi:10.1021/nl201470j

20.   Wu H, Chan G, Choi JW, Ryu I, Yao Y, McDowell MT, Lee SW, Jackson A, Yang Y, Hu L, et al. Stable cycling of double-walled silicon nanotube battery anodes through solid-electrolyte interphase control. *Nat Nanotechnol* (2012) **7**:310–5. doi:10.1038/nnano.2012.35

21.   Zhu B, Jin Y, Tan Y, Zong L, Hu Y, Chen L, Chen Y, Zhang Q, Zhu J. Scalable Production of Si Nanoparticles Directly from Low Grade Sources for Lithium-Ion Battery Anode. *Nano Lett* (2015) **15**:5750–5754. doi:10.1021/acs.nanolett.5b01698

22.   Chen Z, Wang C, Lopez J, Lu Z, Cui Y, Bao Z. High-areal-capacity silicon electrodes with low-cost silicon particles based on spatial control of self-healing binder. *Adv Energy Mater* (2015) **5**:1–8. doi:10.1002/aenm.201401826

23.   Liu N, Lu Z, Zhao J, McDowell MT, Lee H-W, Zhao W, Cui Y. A pomegranate-inspired nanoscale design for large-volume-change lithium battery anodes. *Nat Nanotechnol* (2014) **9**:187–92. doi:10.1038/nnano.2014.6

24.   Etacheri V, Haik O, Goffer Y, Roberts GA, Stefan IC, Fasching R, Aurbach D. Effect of fluoroethylene carbonate (FEC) on the performance and surface chemistry of Si-nanowire li-ion battery anodes. *Langmuir* (2012) **28**:965–976. doi:10.1021/la203712s

25.   Lin Y-M, Klavetter KC, Abel PR, Davy NC, Snider JL, Heller A, Mullins CB. High performance silicon nanoparticle anode in fluoroethylene carbonate-based electrolyte for Li-ion batteries. *Chem Commun* (2012) **48**:7268. doi:10.1039/c2cc31712e

26.   Schroder K, Alvarado J, Yersak TA, Li J, Dudney N, Webb LJ, Meng YS, Stevenson KJ. The Effect of Fluoroethylene Carbonate as an Additive on the Solid Electrolyte Interphase on Silicon Lithium-Ion Electrodes. *Chem Mater* (2015) **27**:5531–5542. doi:10.1021/acs.chemmater.5b01627

27.   Fergus JW. Ceramic and polymeric solid electrolytes for lithium-ion batteries. *J Power Sources* (2010) **195**:4554–4569. doi:10.1016/j.jpowsour.2010.01.076

28.   Knauth P. Inorganic solid Li ion conductors: An overview. *Solid State Ionics* (2009) **180**:911–916. doi:10.1016/j.ssi.2009.03.022

29.   Kim JG, Son B, Mukherjee S, Schuppert N, Bates A, Kwon O, Choi MJ, Chung HY, Park S. A review of lithium and non-lithium based solid state batteries. *J Power Sources* (2015) **282**:299–322. doi:10.1016/j.jpowsour.2015.02.054

30.   Minami T, Hayashi A, Tatsumisago M. Recent progress of glass and glass-ceramics as solid electrolytes for lithium secondary batteries. *Solid State Ionics* (2006) **177**:2715–2720. doi:10.1016/j.ssi.2006.07.017

31.   Deiseroth HJ, Kong ST, Eckert H, Vannahme J, Reiner C, Zai?? T, Schlosser M. Li6PS5X: A class of crystalline Li-rich solids with an unusually high Li+ mobility. *Angew Chemie - Int Ed* (2008) **47**:755–758. doi:10.1002/anie.200703900

32.   Ding J, Wang H, Li Z, Kohandehghan A, Cui K, Xu Z, Zahiri B, Tan X, Lotfabad EM, Olsen

BC, et al. Carbon nanosheet frameworks derived from peat moss as high performance sodium ion battery anodes. *ACS Nano* (2013) **7**:11004–11015. doi:10.1021/nn404640c

33. Lee DH, Xu J, Meng YS. An advanced cathode for Na-ion batteries with high rate and excellent structural stability. *Phys Chem Chem Phys* (2013) **15**:3304–12. doi:10.1039/c2cp44467d

34. Liu Y, Xu Y, Zhu Y, Culver JN, Lundgren CA, Xu K, Wang C. Tin-coated viral nanoforests as sodium-ion battery anodes. *ACS Nano* (2013) **7**:3627–3634. doi:10.1021/nn400601y

35. Ellis LD, Wilkes BN, Hatchard TD, Obrovac MN. In Situ XRD Study of Silicon, Lead and Bismuth Negative Electrodes in Nonaqueous Sodium Cells. *J Electrochem Soc* (2014) **161**:A416–A421. doi:10.1149/2.080403jes

36. Komaba S, Matsuura Y, Ishikawa T, Yabuuchi N, Murata W, Kuze S. Redox reaction of Sn-polyacrylate electrodes in aprotic Na cell. *Electrochem commun* (2012) **21**:65–68. doi:10.1016/j.elecom.2012.05.017

37. Jung SC, Jung DS, Choi JW, Han YK. Atom-level understanding of the sodiation process in silicon anode material. *J Phys Chem Lett* (2014) **5**:1283–1288. doi:10.1021/jz5002743

38. Legrain F, Malyi OI, Manzhos S. Comparative computational study of the energetics of Li, Na, and Mg storage in amorphous and crystalline silicon. *Comput Mater Sci* (2014) **94**:214–217. doi:10.1016/j.commatsci.2014.04.010

39. Bruce PGG, Scrosati B, Tarascon J-M. Nanomaterials for rechargeable lithium batteries. *Angew Chem Int Ed Engl* (2008) **47**:2930–2946. doi:10.1002/anie.200702505

40. Goriparti S, Miele E, De Angelis F, Di Fabrizio E, Proietti Zaccaria R, Capiglia C. Review on recent progress of nanostructured anode materials for Li-ion batteries. *J Power Sources* (2014) **257**:421–443. doi:10.1016/j.jpowsour.2013.11.103

41. Armand M, Tarascon J-M. Building better batteries. *Nature* (2008) **451**:652–657. doi:10.1038/451652a

42. Dörfler S, Hagen M, Althues H, Tübke J, Kaskel S, Hoffmann MJ. High capacity vertical aligned carbon nanotube/sulfur composite cathodes for lithium–sulfur batteries. *Chem Commun* (2012) **48**:4097. doi:10.1039/c2cc17925c

43. He G, Ji X, Nazar L. High "C" rate Li-S cathodes: sulfur imbibed bimodal porous carbons. *Energy Environ Sci* (2011) **4**:2878. doi:10.1039/c1ee01219c

44. Wang Y-X, Huang L, Sun L-C, Xie S-Y, Xu G-L, Chen S-R, Xu Y-F, Li J-T, Chou S-L, Dou S-X, et al. Facile synthesis of a interleaved expanded graphite-embedded sulphur nanocomposite as cathode of Li–S batteries with excellent lithium storage performance. *J Mater Chem* (2012) **22**:4744. doi:10.1039/c2jm15041g

45. Singhal R, Chung S-H, Manthiram A, Kalra V. A free-standing carbon nanofiber interlayer for high-performance lithium-sulfur batteries. *J Mater Chem A* (2015) **3**:4530–4538. doi:10.1039/c4ta06511e

46. Chen R, Zhao T, Lu J, Wu F, Li L, Chen J, Tan G, Ye Y, Amine K. Graphene-based three-dimensional hierarchical sandwich-type architecture for high-performance Li/S batteries. *Nano Lett* (2013) **13**:4642–4649. doi:10.1021/nl4016683

47. Abraham KM, Jiang Z. A Polymer Electrolyte − Based Rechargeable Lithium / Oxygen

Battery TECHNICAL PAPERS ELECTROCHEMICAL SCIENCE AND TECHNOLOGY A Polymer Electrolyte-Based Rechargeable lithium / Oxygen Battery. *J Electrochem Soc* (1996) **143**:1–5. doi:10.1149/1.1836378

48.   Bruce PG, Freunberger S a., Hardwick LJ, Tarascon J-M. Li–O2 and Li–S batteries with high energy storage. *Nat Mater* (2011) **11**:172–172. doi:10.1038/nmat3237

49.   Lu Y-C, Gallant BM, Kwabi DG, Harding JR, Mitchell RR, Whittingham MS, Shao-Horn Y. Lithium-oxygen batteries: bridging mechanistic understanding and battery performance. *Energy Environ Sci* (2013) **6**:750–768. doi:Doi 10.1039/C3ee23966g

50.   Lee J-H, Black R, Popov G, Pomerantseva E, Nan F, Botton GA, Nazar LF. The role of vacancies and defects in Na0.44MnO2 nanowire catalysts for lithium–oxygen batteries. *Energy Environ Sci* (2012) **5**:9558. doi:10.1039/c2ee21543h

51.   McCloskey BD, Bethune DS, Shelby RM, Girishkumar G, Luntz AC. Solvents ' Critical Role in Nonaqueous Lithium À Oxygen Battery. *J Phys Chem Lett* (2011) **2**:1161–1166. doi:10.1021/jz200352v

52.   McCloskey BD, Scheffler R, Speidel A, Girishkumar G, Luntz AC. On the mechanism of nonaqueous Li-O2 electrochemistry on C and its kinetic overpotentials: Some implications for Li-air batteries. *J Phys Chem C* (2012) **116**:23897–23905. doi:10.1021/jp306680f

53.   Mitchell RR, Gallant BM, Thompson C V., Shao-Horn Y. All-carbon-nanofiber electrodes for high-energy rechargeable Li–O2 batteries. *Energy Environ Sci* (2011) **4**:2952. doi:10.1039/c1ee01496j

54.   Adams BD, Radtke C, Black R, Trudeau ML, Zaghib K, Nazar LF. Current density dependence of peroxide formation in the Li–O2 battery and its effect on charge. *Energy Environ Sci* (2013) **6**:1772–1777. doi:10.1039/c3ee40697k

55.   Johnson L, Li C, Liu Z, Chen Y, Freunberger S a, Ashok PC, Praveen BB, Dholakia K, Tarascon J-M, Bruce PG. The role of LiO2 solubility in O2 reduction in aprotic solvents and its consequences for Li-O2 batteries. *Nat Chem* (2014) **6**:1091–9. doi:10.1038/nchem.2101

56.   Murty BS, Kori S a., Chakraborty M. Grain refinement of aluminium and its alloys by heterogeneous nucleation and alloying. *Int Mater Rev* (2002) **47**:3–29. doi:10.1179/095066001225001049

57.   Qiu D, Bu G, Zhao B, Lin Z, Pu L, Pan L, Shi Y. In situ growth of mesoporous NiO nanoplates on a graphene matrix as cathode catalysts for rechargeable lithium-air batteries. *Mater Lett* (2015) **141**:43–46. doi:10.1016/j.matlet.2014.11.033

58.   Hong M, Choi HC, Byon HR. Nanoporous NiO plates with a unique role for promoted oxidation of carbonate and carboxylate species in the Li-O2 battery. *Chem Mater* (2015) **27**:2234–2241. doi:10.1021/acs.chemmater.5b00488

CHAPTER 4

OPTIMIZATION OF EXPERIMENTAL PARAMETERS FOR RELIABLE TEM INVESTIGATION OF LI-O$_2$ BATTERY

To understand the performance of Li-O$_2$ batteries, transmission electron microscopy (TEM) is needed in order to obtain chemical and structural details of the discharge products at a very local scale. However, degradation of the sample upon air exposure and electron-beam irradiation poses challenges. In this chapter, we evaluate experimental procedures to reduce electron-beam degradation and present methods to deal with air sensitivity. This will allow us to acquire reliable data from TEM measurements. The sample's air sensitivity can be addressed by using a vacuum transfer TEM holder. As with electron-beam degradation, we show that Li$_2$O$_2$ decomposition under e-beam irradiation is some 4–5 times more severe at 80 than at 200 kV, and the decomposition is completely dose-dependent. We also show that low-dose-rate STEM exposure is useful to keep the sample in its pristine state. We further demonstrate that a "graphene cell", which encapsulates the sample between graphene sheets, can protect it against damage due to air and e-beam exposure.

Optimization of Experimental Parameters for Reliable TEM Investigation of Li-O2
Battery

1. Introduction

In the context of foreseeable fuel shortages and the growing emphasis on green
technologies, electrification of road transportation is a potential solution for
environmental protection. Lithium−O_2 batteries, whose theoretical energy density is
comparable to that of gasoline, have the potential to become the battery of choice
for electric vehicles [1-3]. Worldwide research over the past five years has made
huge strides toward understanding their complex chemistry [4-6]. However, high
overpotential during charging, poor capacity retention and low cycle life are still the
main impediments to their practical application [7,8].

The morphology of Li_2O_2 is reported to determine the reversibility and charge
overpotential of such batteries. Small peroxide particles lead to lower charge than
large ones do [9,10]. The morphology of the discharge products also depends on the
type of carbon support and electrolytes used [11].

In addition to the desired Li_2O_2, several undesirable discharge products are also
formed. Depending on the electrolyte and current density, a significant amount of
irreversible Li_2O is found [8]. Several carbonate-based products, including lithium
carbonates, are reported due to the decomposition of electrolytes, especially in
carbonate-based electrolytes [12]. Ether-based electrolytes, which are less prone
than carbonate-based electrolytes to superoxide attack, are considered a better
choice for Li-O_2 batteries because they generate mainly Li_2O_2 as a discharge
product [13]. Carbon, which is the most common material of the porous cathode
support, also can cause carbonates to form due to side reactions with the electrolyte
[14]. Recently, several carbon-free support cathodes such as nanoporous gold,
indium-tin oxide and titanium nitride have been used to avoid the parasitic reactions
involving carbon and electrolyte and/or Li_2O_2, and hence to reduce the charge
overpotential and improve the cycling performance of Li-O_2 batteries [5,15,16].

Several papers have reported the use of catalyst/promoter nanoparticles dispersed
on a porous cathode support to improve the (dis)charge overpotential and prolong
cycle life [15,16]. Nevertheless, the working mechanisms of these catalysts are far
from understood. It is speculated that the catalyst particles control the growth of
Li_2O_2 facets and facilitate the growth of kinetically active facets, thus improving the
reaction kinetics. This necessitates structural and chemical investigations on
discharge products at the nanometer scale to determine any probable
crystallographic and/or compositional variations between the discharge products
grown on catalyst particles and other areas on the cathode. Furthermore, if the
discharge product can be analysed in relation to different carbon and non-carbon

cathode supports, binders and electrolytes, the chemistry of Li-O_2 batteries can be better understood.

Detailed TEM investigations allow crystallographic and compositional analyses of the discharge products at a local scale. However, discharge products are sensitive to air and electron beams. This poses a challenge to retaining the pristine form of the sample throughout the TEM measurements, which jeopardizes a reliable analysis. In this chapter we evaluate the possible ways to avoid air and e-beam degradation such that discharge products can be analysed in their pristine form.

2. Experimental details

Li_2O_2, Li_2O and Li_2CO_3, obtained from Sigma Aldrich, are used as samples to determine the best conditions to prevent air and e-beam degradation. After crushing a sample, we prepared a suspension in anhydrous hexane and dripped it onto TEM grids. The entire sample preparation is done inside a glove box filled with argon and O_2 and H_2O levels of <10 ppm and <1 ppm, respectively. To prevent O2 contact with the sample, TEM grids are loaded into a custom-made vacuum transfer TEM holder inside the glove box. A standard TEM holder is used for experiments using a "graphene cell".

2.1. Graphene cell preparation

A "graphene cell", in which Li_2O_2 particles are encapsulated between graphene sheets, is prepared in the following way. First, multilayer graphene films (3–4 layers) are transferred onto standard holey-carbon TEM grids, following the procedure described in [17]. In brief, standard Au Quantifoil grids with holey carbon films are placed on top of CVD-grown graphene on copper foil, to which drops of isopropanol are applied. During evaporation of the isopropanol, the holey-carbon film of the grid becomes attached to the graphene. The copper is then etched away with a $FeCl_3$ solution, and the graphene-coated grids are rinsed several times with deionized water. Finally, the grids are removed from the water and left to dry on filter paper at ambient temperature.

Two such grids form the scaffold of a graphene cell. It is prepared by applying drops of hexane suspension (containing the Li_2O_2 particles) to a graphene grid with the graphene side facing up and, just before the solution has evaporated completely, placing the second graphene grid on top with the graphene side facing down. As the hexane evaporates, the graphene sheets adhere to each other, thus encapsulating the Li_2O_2 particles. The preparation of a graphene cell, which is done inside the argon glove box, is schematically shown in Figure 1.
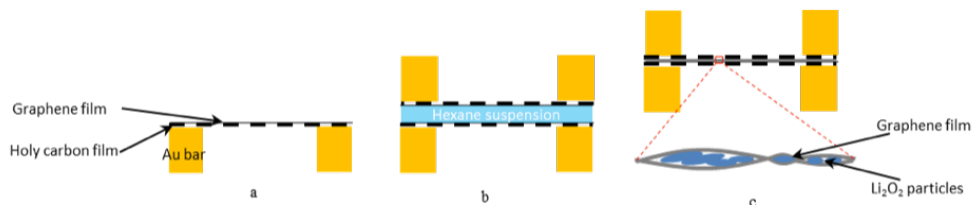
Figure 1: Schematic illustration of graphene cell preparation. The process is performed inside an argon glove box. (a) Holey carbon TEM grid with graphene film; (b) Li_2O_2 suspension in hexane is dripped onto the grid. Before the hexane has evaporated completely, another grid is placed on top of it. (c) As the hexane evaporates, the graphene films become attached to each other, thus encapsulating the Li_2O_2 particles and forming a "graphene cell".

2.2. TEM measurements and dose calculation

TEM measurements are performed in a FEI Tecnai microscope equipped with a Gatan EEL spectrometer and operated at 80 and 200 kV. EEL spectra are recorded in diffraction mode with a resolution of 0.7 eV, determined from the full width at half maximum of the zero-loss peak. Li-K and O-K edges are recorded for acquisition times of 0.1 and 5 s, respectively.

An electron beam current I is calculated in nA using the relation $I = 2.2\ E/t$, where E is the emulsion setting (=2 in our case) and t is the exposure time on screen in seconds. The electron dose is calculated from the beam current.

2.3. Fit procedure for EELS series

Upon e-beam exposure, Li_2O_2 gradually decomposes to Li_2O. Therefore, upon e-beam irradiation, the proportion of Li_2O_2 present in the sample eventually decreases with increasing Li_2O. To determine what experimental conditions will prolong keeping Li_2O_2 in its pristine state during TEM analyses, time-evolved EELS series are acquired for different experimental conditions.

The proportion of Li_2O_2 present at each instant of an EEL spectra series is calculated in the following way. Background-subtracted pristine Li_2O_2, designated by the presence of no peak at 533 eV, and 50% decomposed Li_2O_2, designated by the same intensity 530 and 533 eV peaks, serve as two reference spectra. To determine the proportion of Li_2O_2 present in a spectrum, the background is subtracted from the spectrum and a least-squares fit is used to calculate the two scale factors that should be applied to the reference patterns so their sum would be the best match for the spectrum under consideration. To allow an automated analysis of all spectra, we programmed a simple computer routine. Even though we took extreme care to choose an area with similar particles for all the different series,

thickness variations between different areas cannot be eliminated. Moreover, as the thickness variations in the sample may affect the EELS edge profile, which in turn will affect our ability to quantify the proportion of Li_2O_2, we always assigned the reference spectra from the corresponding series. In the case where the first spectrum of the series already contained a peak at 533 eV, a spectrum from another area with no peak at 533 eV is used as the first reference. Note that such reference spectra can lead to a less reliable analysis.

3. Results

In Li-O_2 batteries along with the reversible discharge product Li_2O_2, the formation of Li_2O and Li_2CO_3 is likely, depending on the conditions discussed above. Therefore, we chose to investigate the effect of air and e-beam exposure on these chemicals. Electron energy loss spectroscopy (EELS) is a very powerful technique that can provide detailed chemical information about the sample under TEM investigation [18]. Background-subtracted Li-K and O-K edge EEL spectra acquired from Li_2O_2, Li_2O and Li_2CO_3 are shown in Figures 2a and b, respectively. These EEL spectra are in good agreement with previously reported XAS spectra [19]. The unambiguous differences between the spectra of Li_2O_2, Li_2O and Li_2CO_3 are due to differences in the local Li and O environments in these compounds. These spectra can be used as reference spectra to verify the chemical compositions of the Li-O_2 battery discharge product. One of the predominant differences in the EEL spectra is the O-K edge position of the Li_2O_2 (at 530 eV) and Li_2O (at 533 eV). Therefore, we chose to monitor the O-K edge for further study.

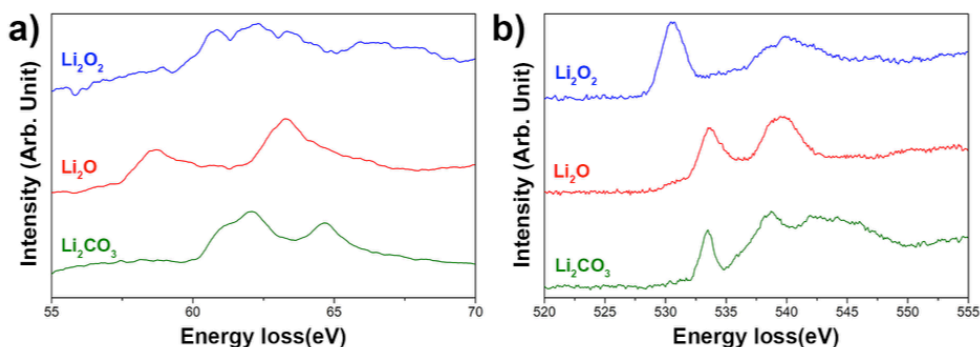**Figure 2:** *Li_2O_2, Li_2O and Li_2CO_3 EEL spectra at the (a) Li-K and (b) O-K edge.*

The sensitivity of Li_2O_2 to air is shown in Figure 3. The EEL spectrum acquired from Li_2O_2 exposed to air is quite different from that of unexposed Li_2O_2. This demonstrates that air exposure alters the pristine Li_2O_2 sample. To avoid any air contact, we used our homemade TEM holder with vacuum transfer stage.
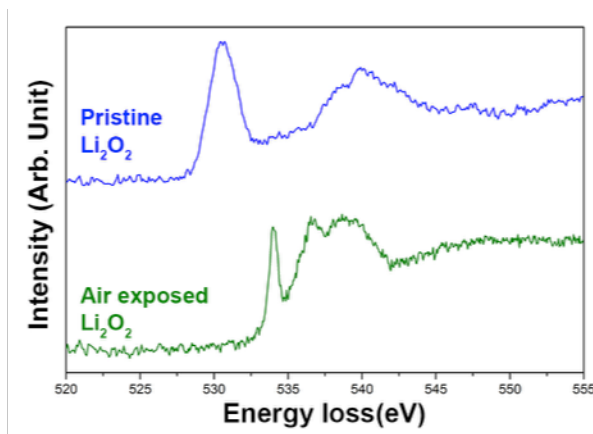
Figure 3: *Effect of air exposure on Li_2O_2 is shown by the O-K edge EEL spectra.*

Electron-beam irradiation in a TEM can change the pristine nature of Li_2O_2 and Li_2CO_3 samples. Figure 4a shows the typical evolution of the O-K edge Li_2O_2-EEL spectra exposed to an e-beam of 200 kV. Increasing e-beam exposure reduces the intensity of the peak at 530 eV and creates a new peak at around 533 eV. The simultaneous decrease of the peak at 530 eV and the increase of the peak at 533 eV with e-beam exposure shows that e-beam irradiation transforms Li_2O_2 into Li_2O. Figure 4b and c show that e-beam irradiation transforms single-crystalline Li_2O_2 particles into polycrystalline Li_2O. It is apparent that this transformation does not proceed via core-shell growth with Li_2O being the newly formed shell. Like Li_2O_2, Li_2CO_3 is also transformed into Li_2O, as can be concluded from Figure 4d.

In order to have reliable chemical and structural analyses of the discharge products, it is essential to keep the sample in its pristine state throughout the measurements. Thus, the transformations of discharge products due to air exposure and e-beam irradiation have to be eliminated. Using a vacuum transfer TEM holder eliminates air exposure of the TEM sample during the transfer process. Thus, air contact with the sample can be completely avoided if the TEM sample is prepared and loaded onto a vacuum transfer TEM holder in a glove box. Even though it is not possible to eliminate e-beam irradiation damage completely, suitable imaging conditions allow the onset of decomposition to be delayed as long as possible, thus providing the opportunity to acquire information about the pristine sample. Therefore, the main goal of the research reported in this chapter is to find suitable imaging parameters that delay the onset of Li_2O_2 decomposition; they will be discussed in the following sections.
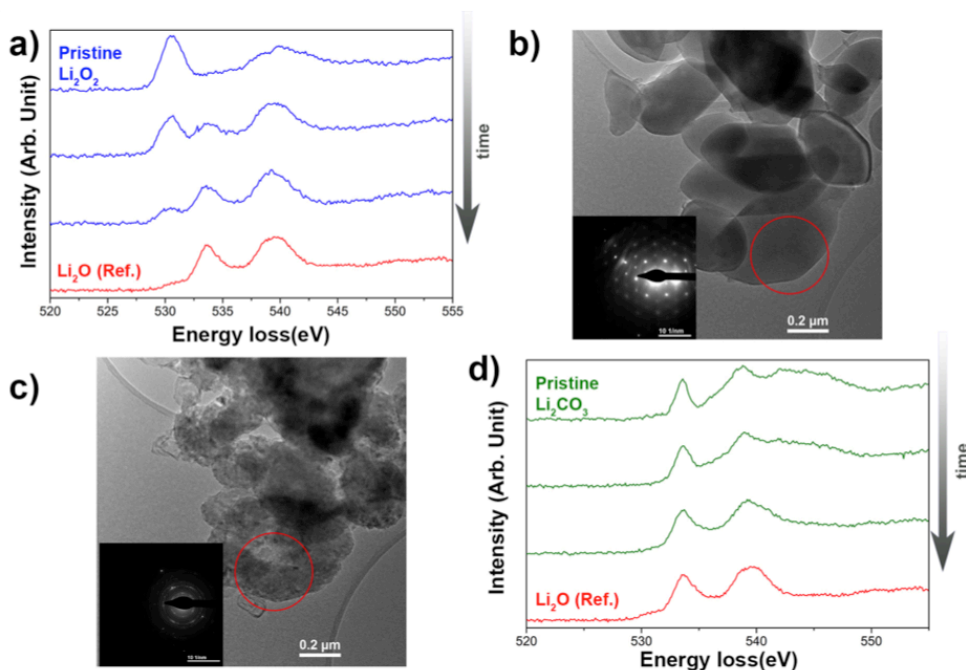
Figure 4: *Effects of e-beam irradiation on Li₂O₂ and Li₂CO₃ are revealed by the O-K edge EEL spectra shown in (a) and (d), respectively. Li₂O EEL spectrum is given as a reference. All O-K edge EEL spectra are acquired at 200 kV for an acquisition time of 5 s using a vacuum transfer holder. Owing to e-beam exposure, (b) single-crystalline Li₂O₂ particles are transformed into (c) polycrystalline Li₂O.*

It is well known that the acceleration voltage plays a significant role in the extent of e-beam damage [20,21]. To check the effect of acceleration voltage in the decomposition rate of Li_2O_2, EELS measurements are carried out at 80 and 200 kV with the same electron dose rate of 8900 enm^{-2}s^{-1}. Figure 5 compares the O-K edge EEL spectra acquired at 80 and 200 kV from a fresh area of the sample that had not been subjected to prior e-beam exposure. We should bear in mind that the pristine area is exposed to e-beam irradiation during the acquisition time of the EEL spectrum (5 s). The sample is exposed to additional irradiation for about 5 s, which is the time required to set up the microscope for EEL spectrum acquisition. Therefore, for the EEL spectra under consideration, the fresh areas are actually exposed to e-beam irradiation for a total of about 10 s. The EEL spectrum acquired at 80 kV shows peaks at 530 and 533 eV, and the intensity of the peak at 533 eV is higher than that at 530 eV. This indicates that a large proportion of the Li_2O_2 has been transformed into Li_2O. The EEL spectrum acquired at 200 kV with the same electron dose shows no detectable peak at 533 eV, meaning that no decomposition has occurred, and that it takes around 4–5 times the electron beam dose to transform a similar amount of Li_2O_2 into Li_2O at 200 than at 80 kV. This shows that e-beam

irradiation damage for Li_2O_2 is faster at 80 than at 200 kV. Thus, to prolong the pristine nature of Li_2O_2, it is better to image at 200 than at 80 kV.
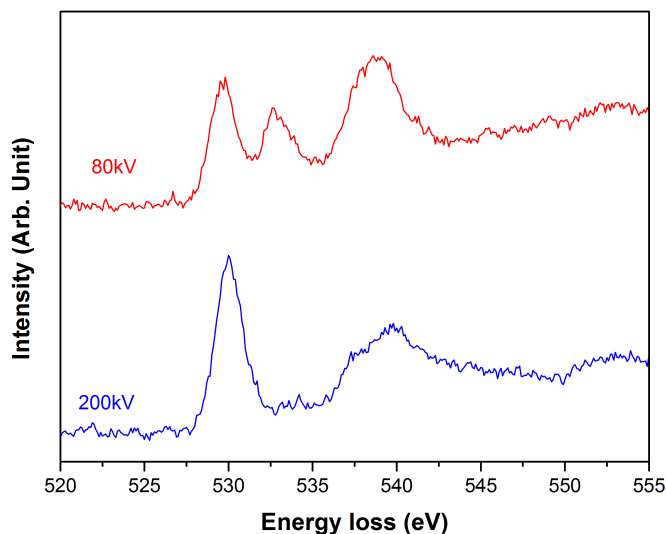
Figure 5: *Comparison of the e-beam irradiation effect on Li_2O_2 at different acceleration voltages. Both spectra are recorded from a fresh spot of the sample with an electron dose rate of 8900 enm^{-2}s^{-1}.*

The Li_2O_2-to-Li_2O transformation also occurs at 200 kV. Figure 6a shows how the proportion of Li_2O_2 is decreased in the sample for an e-beam dose rate of 8900 enm^{-2}s^{-1}. To demonstrate this effect, consecutive EEL spectra are acquired every 10 seconds during e-beam exposure from the same area of the Li_2O_2 sample. The proportion of Li_2O_2 is determined from each spectrum. Please refer to the experimental section for a detailed description of the procedure. The graph in Figure 5 shows that, for a dose rate of 8900 enm^{-2}s^{-1}, the onset of Li_2O_2 decomposition starts after 20 seconds of e-beam exposure. Thus, pristine Li_2O_2 is retained for the first 20 seconds of e-beam exposure. Further irradiation decreases the proportion of Li_2O_2, 50% of which decomposed within 160 seconds.

To check how the onset of decomposition depends on the dose rate, we repeated the experiment with different dose rates. Figure 6b compares the time required to initiate Li_2O formation for 1900, 8900 and 38000 enm^{-2}s^{-1}. For a dose rate of 1900 enm^{-2}s^{-1}, the onset of decomposition is delayed for 60 s, whereas for dose rates of 38000 enm^{-2}s^{-1} and beyond, no onset of decomposition is observed (first acquired EEL spectra show a presence of Li_2O). Therefore, the decomposition onset can be delayed by using a lower dose rate. The dependence of the decomposition on the total electron dose will be addressed below. The typical decomposition trends of Li_2O_2 at different electron dose rates are shown in Figure S-1.

Figure 6: *(a) Typical decomposition trend of Li_2O_2 with a dose rate of 8900 $enm^{-2}s^{-1}$; (b) Effect of electron dose rate to initiate Li_2O formation. All these data are for 200 kV irradiation.*

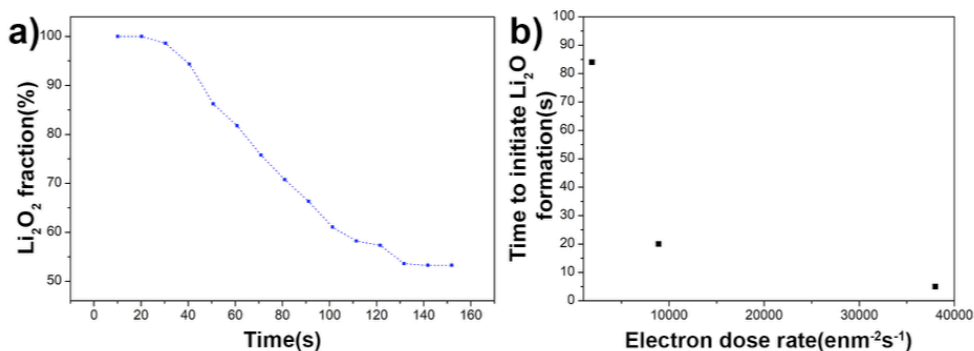To verify the decomposition trend, we have repeated the experiments for each dose rate. Variations in decomposition time can be found for different measurements at the same dose rates, see Figure S-2a. These differences can be attributed to different sample thicknesses, where thin samples tend to decompose faster, as reported by Egerton [20]. We have also observed the slow transformations of thick Li_2O_2 samples (not included here). The times required in various experiments for 50% of Li_2O_2 to decompose are indicated in Figure S-2b.

It has been predicted in the literature that conductive coating could reduce e-beam irradiation damage in insulating samples [20]. With this in mind, we used a graphene cell that encapsulates the sample with conductive graphene sheets. A schematic description of graphene cell preparation is shown in Figure 1. To determine whether the use of the graphene cell can reduce the e-beam decomposition of Li_2O_2, we acquired EEL spectra series. Figure 7a shows a typical decomposition of Li_2O_2 in a graphene cell for a dose rate of 8900 $enm^{-2}s^{-1}$. The onset of Li_2O_2 decomposition is delayed in a graphene cell compared to a standard grid sample: Li_2O_2 withstands four times the e-beam exposure compared to a standard grid sample. Variations in the effectiveness of a graphene cell against e-beam decomposition are described below.

With further e-beam exposure, Li_2O_2 in a graphene cell is also transformed and, within 15 minutes of e-beam exposure, 50% Li_2O_2 decomposes to Li_2O. Like the standard grid, the Li_2O_2 transformation onset is further delayed in a graphene cell when the electron dose rate is reduced to 1900 $enm^{-2}s^{-1}$. In that case, for the first 350 seconds of e-beam exposure in the graphene cell, no detectable Li_2O_2 decomposition occurs, which is four times longer than with an e-beam dose rate of 8900 $enm^{-2}s^{-1}$ and about six times longer than with a standard grid with the same e-beam dose rate of 1900 $enm^{-2}s^{-1}$. The effectiveness of graphene cells in delaying

the onset of decomposition is also observed for higher dose rates. For a dose rate of 38000 $enm^{-2}s^{-1}$, the graphene cell stops Li_2O_2 decomposition for 25 seconds, compared to a standard grid, where an average of 20% of the Li_2O_2 decomposed after only 10 seconds of e-beam exposure. When the e-beam dose rate is increased to 225,000 $enm^{-2}s^{-1}$, no onset of the decomposition can be seen in the graphene cell. Figure 7b compares the time required to initiate Li_2O_2 decomposition in a graphene cell and a standard grid sample at different dose rates.
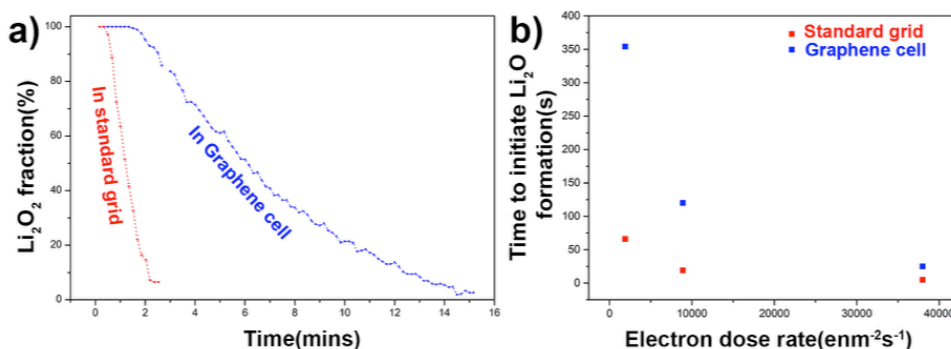
Figure 7: *Effectiveness of the graphene cell to delay the formation of Li_2O. (a) A typical decomposition trend of Li_2O_2 with a dose rate of 8900 $enm^{-2}s^{-1}$. (b) Effect of electron dose to initiate Li_2O formation. All these data are for 200 kV irradiation. Average values from the standard grid are given as a reference.*

In a graphene cell, the oxygen released during the Li_2O_2-to-L_2O transformation would be trapped within the graphene pocket, creating an oxygen-rich environment. Therefore, one could argue that this oxygen-rich environment delays the Li_2O_2-to-Li_2O transformation. For our investigations, we used an electron beam to drill holes in the graphene cell close to the sample area to provide a path for oxygen release. Nevertheless we found no significant difference in the Li_2O_2 decomposition behavior. Therefore the oxygen-rich environment is not the main reason for the prolonged delay in Li_2O_2 decomposition.

To check whether the graphene cell is similarly effective throughout the grid area, we recorded several sets of EEL spectra from different areas of the graphene cell. Figure S-3 shows the time required for a 50% decomposition of Li_2O_2 with different dose rates for the various experiments. The figures show that, even though the graphene cell shows better overall performance than the standard grid in terms of lowering the decomposition rates, the performance of the graphene cell is not the same everywhere. The decomposition trends in the graphene cell at different dose rates can be seen in Figure S-4. Average decomposition curves from a standard grid are shown for easy comparison. We attribute the large variation in e-beam-induced

decomposition to differences in the encapsulation of Li_2O_2 between graphene sheets. As different sample thicknesses also led to variations, it is difficult to uncouple the performance of the graphene cell in various areas of the grid.

In addition to delaying Li_2O_2 decomposition, the graphene cell can also protect Li_2O_2 from degradation caused by air exposure. EEL spectra acquired from the Li_2O_2 in the graphene cell after exposure to air closely resemble those from an unexposed sample. This indicates that a pristine form of Li_2O_2 could be retained in a graphene cell even if it is exposed to air because the graphene cell encapsulates the discharge products that are sensitive to air exposure. Figure S-5 compares the non-exposed Li_2O_2 O-K edge spectra with the exposed samples in a standard grid and a graphene cell.

In STEM mode, a focused probe is scanned over the sample, typically residing for only a few microseconds (depending on the dwell time) at the same spot. To check whether this kind of irradiation increases the onset of Li_2O_2 decomposition, we exposed the sample under STEM scanning to irradiation at different electron dose rates. In STEM, the dose rate can be changed in two ways: by changing the beam dwell time or by changing the pixel size by adjusting the magnification. We observed that, with a dose rate of lower than $100 \ enm^{-2}s^{-1}$, Li_2O_2 could withstand 30 minutes of STEM scanning without decomposing to Li_2O. Therefore, the STEM mode is ideal for investigating the morphology of the discharge products while retaining the pristine nature of the sample. We have acquired EEL spectra in TEM mode to check the decomposition behaviour of the sample. To avoid degradation of Li_2O_2 during spectra acquisition, EEL spectra are acquired at a dose rate of $1900 \ enm^{-2}s^{-1}$, and acquisition numbers are kept to a minimum.

However, we detected faster Li_2O_2 decomposition with increasing dose rates. For example, at a dose rate of $100 \ enm^{-2}s^{-1}$, Li_2O_2 retains its pristine state for 30 minutes under STEM scanning, whereas 50% of the Li_2O_2 decomposed within 30 seconds for a dose rate of $28,000 \ enm^{-2}s^{-1}$, a magnification of $160,000\times$ and a dwell time of 50 µs. Details about the parameters used during the STEM investigations are listed in S-6.

4. Discussion

As the reaction products of air or e-beam-induced degradation are quite similar to some of the discharge products in a Li-O_2 battery, it is essential to keep the sample in its pristine state until and during TEM analysis. Air exposure transforms Li_2O_2 into Li_2O. We have shown that degradation due to air exposure can be avoided by using a vacuum transfer TEM holder or by encapsulating the Li_2O_2 in a graphene

cell (Figure S-7). For the air exposure test, we kept the TEM sample at ambient atmosphere for one hour. Therefore, the changes in EEL spectra are due to being exposed to air for one hour. We chose such a long air exposure to show the effect prominently. We should point out that the EEL spectrum acquired from a sample exposed to air for two minutes showed no significant difference from the unexposed sample (not shown here). However, Li_2O_2 layers only a few nanometers thick formed during the fast discharge, and are likely to transform much faster upon contact with air. Thus, to ensure that we retain the sample in its pristine state for TEM investigations, any amount of air exposure should be avoided. We have also explored different measures one can take to reduce e-beam irradiation damage. Even though it is not possible to prevent e-beam damage completely, as can be seen from the results, the pristine nature of Li_2O_2 can be prolonged despite e-beam radiation by using (a) a relatively high acceleration voltage, (b) a lower electron dose rate, (c) a graphene cell and (d) STEM mode. We observed that Li_2O_2 could sustain 4-5 times the electron dose at 200 than at 80 kV. Moreover, compared to Li_2O_2 in a normal TEM grid, Li_2O_2 in a graphene cell can sustain 4 times the electron dose before it starts to transform into Li_2O (considering the best case scenario).

Decomposition of Li_2O_2 to Li_2O occurs also if Li_2O_2 is heated. It is reported that the Li_2O_2 decomposition proceeds via Li_2O_2-Li_2O solid solution formation till 50% Li_2O_2 is decomposed [22,23]. However, our EELS study showed that with increasing e-beam exposure the peak around 530eV became weaker and simultaneously a new peak at around 533eV appeared and enhanced. The presence of two distinct peaks at 530eV and 533eV, which are representative of Li_2O_2 and Li_2O respectively, throughout the Li_2O_2 to Li_2O transformation indicate that no solid solution is formed during e-beam decomposition while crystalline Li_2O_2 transform to nanocrystalline Li_2O as evident from the figure 4(c) and 4(d).

For insulating materials in TEM knockout displacement cross-section is considerably below than that of ionization damage. So although knockout damages do occur in insulating specimens, ionization damage remains the dominant form of damage [24,25]. Since the inelastic scattering cross section varies inversely to the acceleration voltage, Li_2O_2 decomposes faster at 80kV compare to 200kV.

Our experiments show that a 'graphene cell' can delay the Li_2O_2 decomposition as depicted in figure 7(b). Zan et al. and Algara-Siller et al. have already demonstrated the damage reduction capability of graphene, where they sandwiched MoS_2 with graphene sheets [26,27]. Even though one can argue in case of MoS_2 graphene sheets are very well connected due to two-dimensional nature of MoS_2 compare to our tens of nanometer thick Li_2O_2 particles, we observed a clear damage reduction

with graphene cell. Thus even a partial graphene coverage to can delay the decomposition of Li_2O_2. It's worth to mention that the preparation of our 'graphene cell' is quite different to that of the graphene-MoS_2 sandwich. In our case when hexane evaporates from in between two graphene grids, during graphene cell preparation, Van der Waals interaction binds the graphene sheets and Li_2O_2 particles together. Though the exact mechanisms responsible for the improvement against beam damage are difficult to determine with certainty, the remarkable electric and thermal conduction of graphene abet with the said attachment is expected to contribute effectively in dissipating the accumulated charge or heat under the beam. However, comparing the result from different parts of the graphene cell, we found that the effectiveness of graphene cell is not same throughout the grid. This is perhaps due to bad attachment of graphene sheets and Li_2O_2 particles at that particular area. Functionalization of graphene sheets may improve the attachment.

Since the e-beam damage cannot be eliminated completely the sole aim of our work is to find solution to delay the decomposition onset. And it is noticed for both standard grid and graphene cell lower electron dose rate lead to delay in the decomposition onset; however at higher dose rate it seem this onset is absent (figure 7(b)). This suggests the possibility of a threshold dose rate below which an onset of decomposition can be found. However, from the comparison between the total dose required for 50% Li_2O_2 decomposition (figure 8) in the standard grid and graphene cell at different dose rate it can be seen, roughly, the total dose required for the decomposition is independent of the e-beam dose rate. This advocates that the decomposition is total dose dependent.
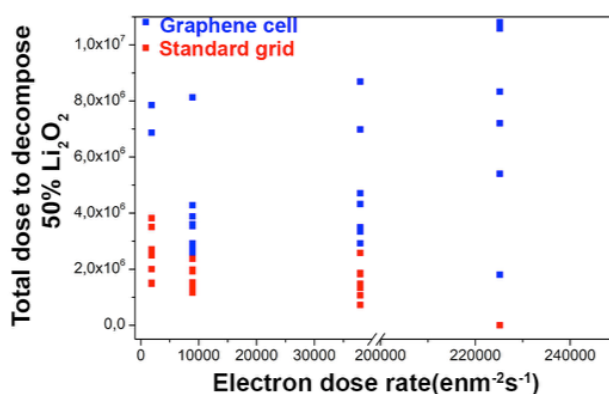

Figure 8: *Shows the comparison between the total dose required to decompose 50% Li_2O_2 at different dose rates in standard grid and graphene cell at 200kV.*

We found Li_2O_2 could withstand STEM scanning for 30 minutes for electron dose rate lower than 100 e/nm^{2}s without being decomposed at all. So, one may conclude in STEM mode Li_2O_2 can withstand more electron dose compare to TEM mode. However if we calculate the total dose the Li_2O_2 particles had faced during the STEM scanning, we see that it is one order of magnitude less than it required to decompose Li_2O_2 particles in TEM mode [Table S-6]. Further, as pointed out earlier, increase in dose rate via decrease in pixel size (increase in magnification) and/or increase in beam dwell time leads to faster decomposition of Li_2O_2. This result at a fast glance suggested dose rate dependent decomposition. However when the total dose is calculated for each case, total electron dose dependent decomposition emerges.

5. Conclusions

To keep the discharge products in their pristine state, air contact must be avoided, which necessitates using the TEM vacuum transfer holder. We found that 80 kV of irradiation causes Li_2O_2 to decompose much faster than 200 kV at the same electron dose rate. Therefore, for TEM investigations, we recommend using a relatively higher acceleration voltage. Decomposition is completely dependent on the radiation dose, and using a low e-beam dose rate delays the onset of decomposition long enough to allow the sample to be analysed in its pristine state. In STEM mode, lower dose rates, and thus low beam dwell times and magnification, are ideal for preserving the pristine nature of the sample much longer, which is ideal for TEM investigations. However, like in TEM mode, higher dose rates degrade the pristine Li_2O_2 faster in STEM mode.

A "graphene cell" provides the perfect stage for investigating Li-O$_2$ battery discharge products. Graphene cells not only prevent decomposition of the sample due to air exposure, they also delay the onset of e-beam degradation compared to the sample on a standard TEM grid. Nevertheless, the performance of a graphene cell is not the same throughout the grid, probably due to poor encapsulation. Further work is needed to improve this situation, and graphene cells show great promise as the ideal carriers for investigating Li-O$_2$ battery discharge products.

The understanding obtained from the current investigation will serve as a solid basis to expand our understanding of Li-O$_2$ battery discharge products from TEM analyses and thus to advance Li-O$_2$ battery technology.

References

1. Rahman MA, Wang X, Wen C. A review of high energy density lithium-air battery technology. *J Appl Electrochem* (2014) **44**:5–22. doi:10.1007/s10800-013-0620-8

2. Girishkumar G, McCloskey B, Luntz AC, Swanson S, Wilcke W. Lithium-air battery: Promise and challenges. *J Phys Chem Lett* (2010) **1**:2193–2203. doi:10.1021/jz1005384

3. Lu Y-C, Gallant BM, Kwabi DG, Harding JR, Mitchell RR, Whittingham MS, Shao-Horn Y. Lithium-oxygen batteries: bridging mechanistic understanding and battery performance. *Energy Environ Sci* (2013) **6**:750–768. doi:Doi 10.1039/C3ee23966g

4. Peng Z, Freunberger S a., Chen Y, Bruce PG. A Reversible and Higher-Rate Li-O2 Battery. *Science (80-)* (2012) **337**:563–566. doi:10.1126/science.1223985

5. Ottakam Thotiyl MM, Freunberger S a, Peng Z, Chen Y, Liu Z, Bruce PG. A stable cathode for the aprotic Li-O2 battery. *Nat Mater* (2013) **12**:1050–6. doi:10.1038/nmat3737

6. Adams BD, Black R, Radtke C, Williams Z, Mehdi BL, Browning ND, Nazar LF. The importance of nanometric passivating films on cathodes for Li-Air batteries. *ACS Nano* (2014) **8**:12483–12493. doi:10.1021/nn505337p

7. Feng, NingningFeng, N., He, P., & Zhou, H. (2016). Critical Challenges in Rechargeable Aprotic Li-O2 Batteries. Advanced Energy Materials, 6(9) 1–24. http://doi.org/10.1002/aenm.201502303, He P, Zhou H. Critical Challenges in Rechargeable Aprotic Li-O2 Batteries. *Adv Energy Mater* (2016) **6**:1–24. doi:10.1002/aenm.201502303

8. Christensen J, Albertus P, Sanchez-Carrera RS, Lohmann T, Kozinsky B, Liedtke R, Ahmed J, Kojic A. A Critical Review of Li∕Air Batteries. *J Electrochem Soc* (2012) **159**:R1. doi:10.1149/2.086202jes

9. Hu Y, Han X, Cheng F, Zhao Q, Hu Z, Chen J. Size effect of lithium peroxide on charging performance of Li-O2 batteries. *Nanoscale* (2014) **6**:177–80. doi:10.1039/c3nr04728h

10. Lau S, Archer LA. Nucleation and Growth of Lithium Peroxide in the Li-O$_2$ Battery. *Nano Lett* (2015) **15**:5995–6002. doi:10.1021/acs.nanolett.5b02149

11. Geaney H, O'Dwyer C. Examining the Role of Electrolyte and Binders in Determining Discharge Product Morphology and Cycling Performance of Carbon Cathodes in Li-O-2 Batteries. *J Electrochem Soc* (2016) **163**:A43–A49. doi:10.1149/2.1011514jes

12. Freunberger SA, Chen Y, Peng Z, Griffin JM, Hardwick LJ, Bardé F, Novák P, Bruce PG. Reactions in the rechargeable lithium-O2 battery with alkyl carbonate electrolytes. *J Am Chem Soc* (2011) **133**:8040–8047. doi:10.1021/ja2021747

13. Balaish M, Kraytsberg A, Ein-Eli Y. A critical review on lithium-air battery electrolytes. *Phys Chem Chem Phys* (2014) **16**:2801–2822. doi:10.1039/C3CP54165G

14. McCloskey BD, Speidel A, Scheffler R, Miller DC, Viswanathan V, Hummelshøj JS, Nørskov JK, Luntz AC. Twin problems of interfacial carbonate formation in nonaqueous Li-O 2 batteries. *J Phys Chem Lett* (2012) **3**:997–1001. doi:10.1021/jz300243r

15. Li F, Tang DM, Chen Y, Golberg D, Kitaura H, Zhang T, Yamada A, Zhou H. Ru/ITO: A carbon-free cathode for nonaqueous Li-O2 battery. *Nano Lett* (2013) **13**:4702–4707. doi:10.1021/nl402213h

16. Chang Y, Dong S, Ju Y, Xiao D, Zhou X, Zhang L, Chen X, Shang C, Gu L, Peng Z, et al. A Carbon- and Binder-Free Nanostructured Cathode for High-Performance Nonaqueous Li-O2 Battery. *Adv Sci* (2015)n/a-n/a. doi:10.1002/advs.201500092

17. Chen Q, Smith JM, Park J, Kim K, Ho D, Rasool HI, Zettl A, Alivisatos AP. 3D motion of DNA-Au nanoconjugates in graphene liquid cell electron microscopy. *Nano Lett* (2013) **13**:4556–4561. doi:10.1021/nl402694n

18. Egerton RF. Electron energy-loss spectroscopy in the TEM. *Reports Prog Phys* (2008) **72**:16502. doi:10.1088/0034-4885/72/1/016502

19. Qiao R, Chuang Y De, Yan S, Yang W. Soft X-Ray Irradiation Effects of Li2O2, Li2CO3 and Li2O Revealed by Absorption Spectroscopy. *PLoS One* (2012) **7**:3–8. doi:10.1371/journal.pone.0049182

20. Egerton RF, Li P, Malac M. Radiation damage in the TEM and SEM. *Micron* (2004) **35**:399–409. doi:10.1016/j.micron.2004.02.003

21. Egerton RF. Mechanisms of radiation damage in beam-sensitive specimens, for TEM accelerating voltages between 10 and 300 kV. *Microsc Res Tech* (2012) **75**:1550–1556. doi:10.1002/jemt.22099

22. Tsentsiper AB, Kuznetsova ZI. Thermal decomposition of lithium peroxide. *Bull Acad Sci USSR Div Chem Sci* (1965) **14**:1873–1875. doi:10.1007/BF00850186

23. Yao KPC, Kwabi DG, Quinlan R a., Mansour a. N, Grimaud a., Lee Y-L, Lu Y-C, Shao-Horn Y. Thermal Stability of Li2O2 and Li2O for Li-Air Batteries: In Situ XRD and XPS Studies. *J Electrochem Soc* (2013) **160**:A824–A831. doi:10.1149/2.069306jes

24. Egerton RF. Control of radiation damage in the TEM. *Ultramicroscopy* (2013) **127**:100–108. doi:10.1016/j.ultramic.2012.07.006

25. Egerton RF. Choice of operating voltage for a transmission electron microscope. *Ultramicroscopy* (2014) **145**:85–93. doi:10.1016/j.ultramic.2013.10.019

26. Zan R, Ramasse QM, Jalil R, Georgiou T, Bangert U, Novoselov KS. Control of Radiation Damage in MoS by Graphene Encapsulation. *ACS Nano* (2013)1–17. doi:10.1021/nn4044035

27. Algara-Siller G, Kurasch S, Sedighi M, Lehtinen O, Kaiser U. The pristine atomic structure of MoS2 monolayer protected from electron radiation damage by graphene. *Appl Phys Lett* (2013) **103**: doi:10.1063/1.4830036

Appendix B
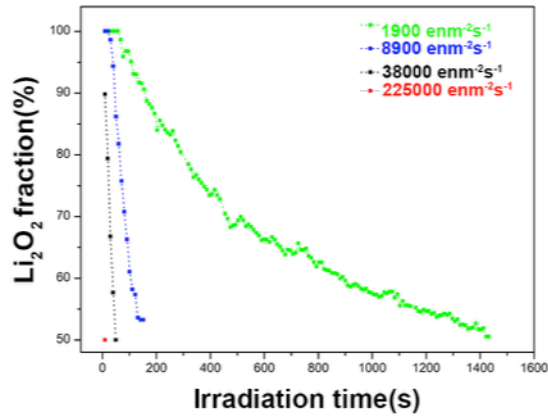
S-1: *Typical decomposition trend of Li$_2$O$_2$ at 200 kV with different dose rates in a standard grid.*
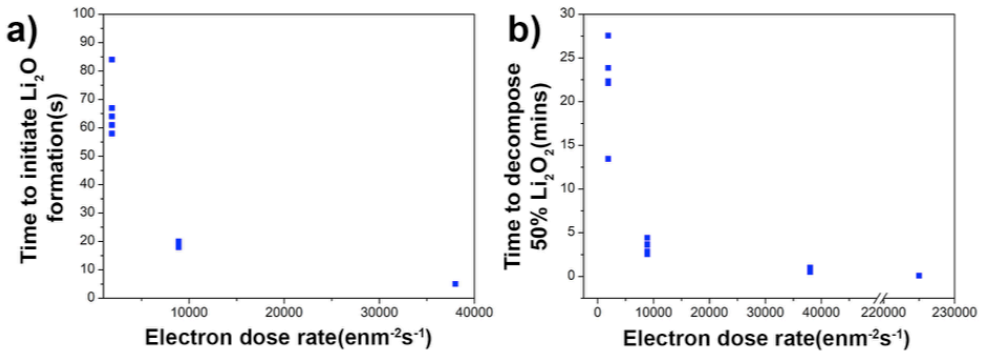
S-2: *Variations in Li$_2$O$_2$ decomposition at different dose rates: (a) time required before Li$_2$O begins to form and (b) time required for 50% of Li$_2$O$_2$ to decompose.*
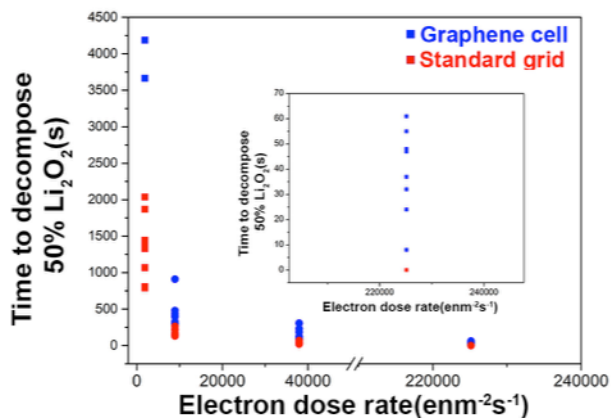
S-3: *Comparison of the time required to for 50% of the Li_2O_2 in a graphene cell and a standard grid to decompose (from various experiments). Inset: Magnified version for a dose rate of 225,000 $enm^{-2}s^{-1}$.*
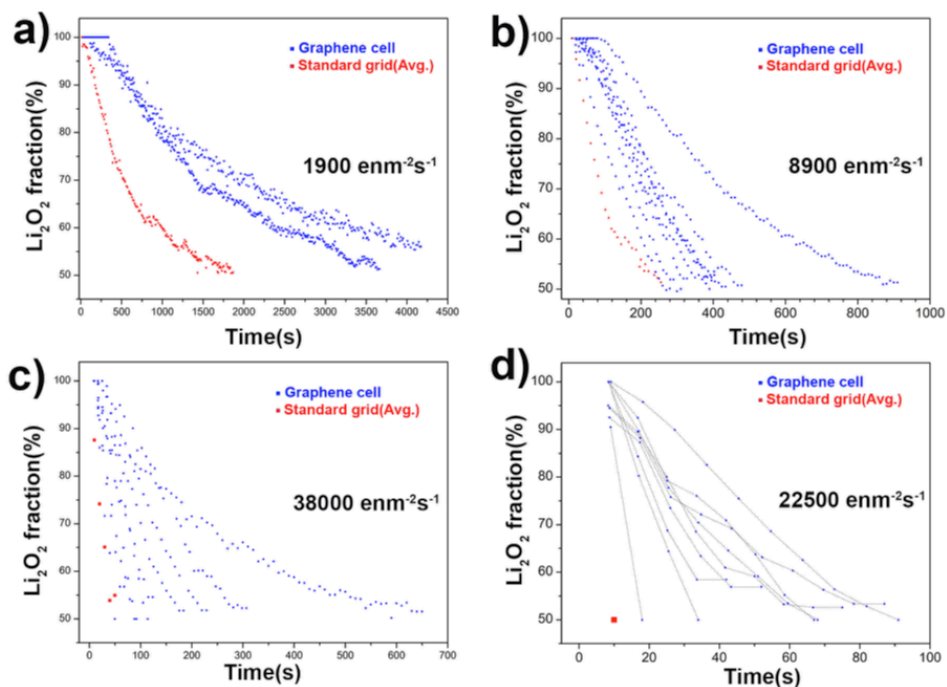
S-4: *Decomposition trend of Li_2O_2 with different dose rates in a graphene cell (from various experiments).*
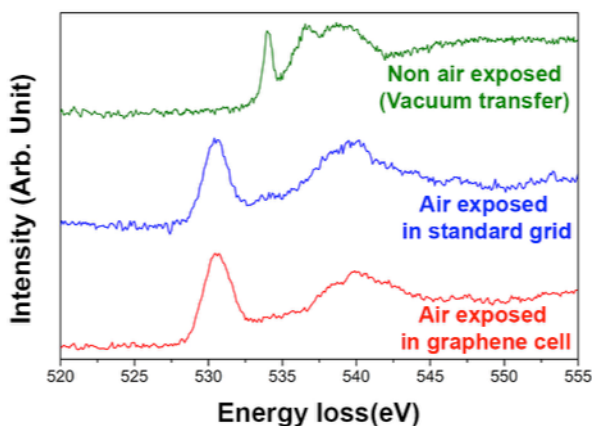
S-5: *Effect of air exposure on Li_2O_2 revealed by O-K edge EELS spectra. Non-air-exposed Li_2O_2 transferred using our vacuum transfer holder is compared with a sample in a standard grid and in a graphene cell exposed to air for 1 h. O-K edge EELS spectra were obtained from a fresh spot on the sample at 200 kV at a dose rate of 1900 $enm^{-2}s^{-1}$.*

Magnification	Dwell time (μs)	Frame (512 × 512 pixels^2) time (s)	Dose rate ($enm^{-2}s^{-1}$)	Time to decompose 50% Li_2O_2 (s)	Total dose (enm^{-2})
20,000×	3	1	27	1800**	$4.8×10^4$
20,000×	12	4	109	1800**	$4.8×10^4$
20,000×	50	16	434	1800**	$4.8×10^4$
20,000×	203	64	1737	1800**	$4.8×10^4$
40,000×	3	1	109	1800**	$1.9×10^5$
40,000×	12	4	434	1800*	$1.9×10^5$
40,000×	50	16	1737	1800*	$1.9×10^5$

40,000×	203	64	6948	1800	1.9×10^5
80,000×	3	1	434	840	3.6×10^5
80,000×	12	4	1737	720	3.1×10^5
80,000×	50	16	6948	520	2.2×10^5
80,000×	203	64	27792	420	1.9×10^5
160,000×	3	1	1737	100	1.7×10^5
160,000×	12	4	6948	60	1×10^5
160,000×	50	16	27792	0†	0†

*Less than 50% Li_2O_2 decomposition in 30 minutes ; ** No decomposition at all in 30 minutes; † more than 50% Li_2O_2 decomposition before measurement (30 seconds)

S-6: *Details of scanning parameters used in STEM mode to compare the time and total dose required to decompose 50% of Li_2O_2 at different dose rates.*

CHAPTER 5

UNVEILING MECHANISMS OF LI-O₂ BATTERIES USING TEM GRIDS

To understand the complex mechanisms of the Li-O₂ battery use of TEM is essential to study the structure and composition of the discharge product on and off catalyst/ promoter nanoparticles. However keeping the native environment intact during the TEM sample preparation techniques, especially owing to the moisture sensitive nature of the discharge products is one of the key concerns. This limits the application of TEM in Li-O₂ battery research. In this study we show that the use of conventional holey carbon TEM grids in a Li-O₂ battery can allow unveiling complex mechanisms of Li-O₂ battery by preserving the native environment of the discharge products.

1. Introduction

With the focus in automobile industry to switch from petroleum-based vehicles to all electric vehicles, to reduce the green house gas emission, the demand for battery capable of delivering higher energy densities is constantly increasing. The Li-O$_2$ battery capable of delivering a theoretical energy density of 3500 Wh/kg, is considered to be the most suitable option. However, there are several obstacles to be overcome before Li-O$_2$ battery can reach its true potential. These include low energy efficiency due the high (dis)charge overpotential, slow kinetics due to poor electronic and ionic conductivity, poor cyclability due pore clogging, incomplete oxidation of the discharge product during charging, several side reactions involving the electrodes and electrolyte [1–7]. Among these challenges, the enormous overpotential during (dis)charge of Li−O$_2$ (e.g., discharge overpotential on carbon >1000 mV) has motivated tremendous research effort for developing effective Li−O$_2$ catalysts or promoters[8–10]. Use of different metal and metal oxides nanoparticles on the porous cathode support are reported to improve the kinetics of the battery. However the detailed underneath mechanism behind the working of the catalyst or promoters is not well understood. Information about the formation and/or decomposition of discharge products, on and off the catalyst or promoter nanoparticles, in realistic Li-O$_2$ batteries will help understanding the mechanism and thus lead to design of better catalysts or promoters.

The formation and/or decomposition of Li$_2$O$_2$ has been studied by a various of in-situ and traditional ex-situ techniques including spectroscopy, and diffraction each providing valuable information about the transformation process [11–15]. Alongside ex-situ characterization, operando studies using mostly spectroscopy and diffraction techniques are relatively easy to perform. However they often only give average information about the whole electrode hiding the details of individual electrode grains. On the other hand transmission electron microscopy (TEM) study attracts lots of attention due to its unique capability of providing visualization along with chemical and structural information at sub nanometer scale. However, traditional TEM study suffers from two main issues. Air and electron beam sensitivity of the discharge products and preserving the native details of the discharge products at nanometer scale during the sample preparation. The decomposition due to air and electron beam exposure can be taken care by using moderately high acceleration voltage (e.g. 200kV), low electron dose, vacuum transfer holder, "graphene cell" as described in details in chapter 4. Even though operando TEM allows study of individual Li$_2$O$_2$ grain transformation, the artificial nature of the setup involved and the high resistances associated with the use of micro batteries do not accurately reflect a representative environment within a

realistic Li-O$_2$ battery electrode. Furthermore, this field is in its infancy and the sophisticated nature of study lacks the wide scale application.

Here we report a simple method, which will allow TEM investigation of the Li-O$_2$ battery discharge products in its native environment to study different stages (dis)charge. This system allows study of the effect of catalyst or promoters on morphology of the discharge product along with chemical composition and/or crystallographic orientation; thus will allow unveiling the role of the catalyst or promoters. All of these, with added advantage is the no requirement of sample preparation step, which is helpful especially considering the highly air sensitive nature of the discharge product. This is achieved using conventional TEM grids with holey carbon film as the porous cathode support.

2. Materials and Methods

Figure 1 shows the schematic of the Li-O$_2$ battery setup used in our experiments. The setup consists of two halves, working as current collectors. A rubber O-ring, which ensures no physical contact between the two halves when they are closed together, separates these halves. The presence of O-ring also ensures the inside parts of the setup remain at pristine environment even if the battery setup is placed in ambient atmosphere. One of the halves has a gas inlet, which allows introduction of oxygen to the system. The bulk porous cathode support (activated carbon coated on porous carbon paper) is placed on a steel mesh, which provide electrical connection as well as allows the incoming oxygen to be diffused through the cathode support. The holey carbon TEM grids are placed on top of the bulk porous cathode support. To ensure good electrical contacts to the TEM grids, piece of aluminium foil are attached to the rim of the grids with conductive carbon paint before placing in on the bulk cathode support. At the other halves of the setup freshly cut lithium foil is placed. Separators soaked in the electrolyte are used to separate direct contact between the lithium foil and the TEM grids. To prevent damage to the TEM grid by the glass fiber from the glass fiber separator a plastic like separator (from Cell Guard) is placed first followed by the glassy fiber separator (from Whatman). In Appendix C the comparison between TEM grids placed with and with out the Cell Guard separator is shown. 1M LiTFSi in TEGDME is used as electrolyte. During discharge of the battery Li-ions from the lithium metal travel through the electrolyte towards the porous support, i.e., bulk cathode support as well as holey carbon TEM grid, where they interact with incoming oxygen from the pores and form discharge products. Due to the air sensitive nature of the discharge product, all the components of the battery are dried inside the glove box overnight before assembling of the battery. For discharging batteries are connected to 1.2 bar oxygen

supply and the discharge process is conducted using AUTOLAB running in galvanostatic mode. After completion of the discharge batteries are disassembled inside glovebox.
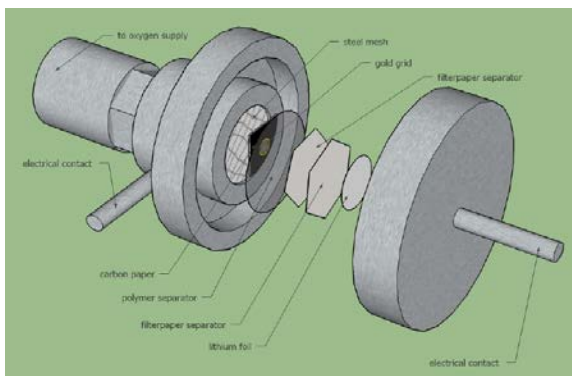

Figure 1: Schematic representation of the Li-O$_2$ battery setup with TEM grid.

For the TEM measurement an in house TEM with a vacuum transfer stage is used to avoid any air exposure to the sample. TEM measurements are carried out in FEI Tecnai microscope operating at 200kV. The beam parameters are chosen carefully to avoid any beam damage to the sample during the measurements. SEM checks are carried out in a simple tabletop SEM from Phenom World operating at 5kV. For SEM studies samples are transferred through ambient atmosphere but exposure is kept below 1 minute to minimize the damage.

3. Results and discussions

In bulk carbon support the presence of the pores are responsible for supplying oxygen to the surface of the electrode allowing dissolution of oxygen in the electrolyte and its subsequent reaction with the incoming lithium-ions also coming via the electrolyte. Holey carbon TEM grids can be considered as the cross section of an ideal porous cathode support, where the pores of the bulk cathode support is represented by the regularly spaced 1μm diameter holes in the grid. Figure 2 illustrates the concept.

To validate our concept, the discharge product that forms on the TEM grid is compared with the discharge product that forms on the bulk carbon support. This is essential to check whether the TEM grids can be used as representative of the bulk. For this a battery is assembled with the TEM grids and discharged till 2.2V with an applied current density of 20 μm/cm^2. The similar morphology of the discharge product, as seen in Figure 3, on both substrates is quite evident. This ensures that the discharge product formed on the TEM grid is representative of the bulk.
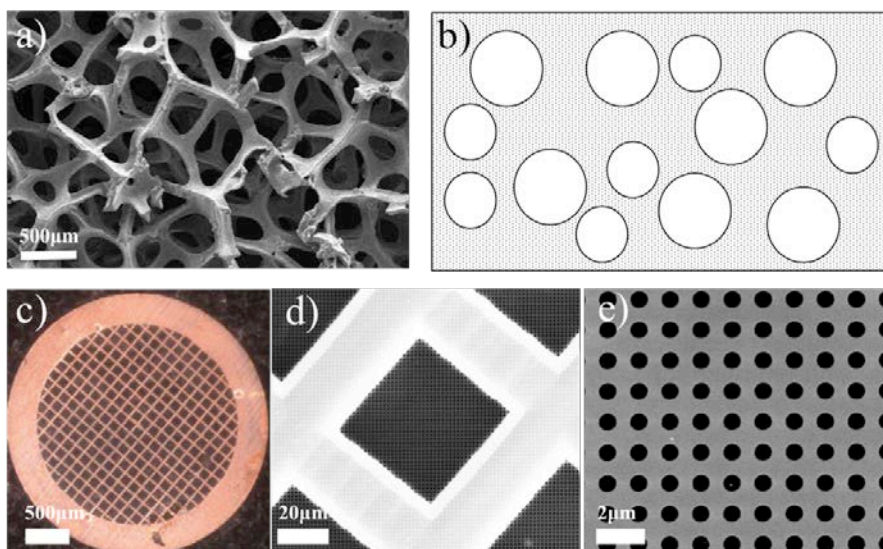
Figure 2: Illustrate the use of TEM grid as representative of the usual porous carbon support used in Li-O$_2$ battery. (a) SEM image of graphene foam used as porous carbon support; (b) Simplified cross sectional representation of graphene foam; (c)-(d) Holey carbon TEM grid at different magnifications, (c) optical micrograph and (d)-(e) SEM images.

Figure 3: SEM images compare between the discharge products formed on bulk cathode support (a-b) and holey carbon grid (c-d) at different magnifications.

To demonstrate the value of the setup we choose to start with a simple system, we coated the TEM grids with 20nm thick continuous gold film. The continuous gold film serves two purposes: it makes the surface of TEM grid electrically conductive and alongside acting as an oxygen reduction reaction (ORR) catalyst [9] .

Figure 4 shows the discharge product formed at various location of the gold-coated TEM grids, due to discharge till 2.2V with an applied current density of 20 $\mu m/cm^2$. From the BF-TEM images (figure 4a - 4c) and EFTEM thickness maps (figure 4d - 4f), performed with 10eV slit, three distinct size variation of the discharge products can be seen: (a) smallest particles (100-200nm) are formed around the edges of the holes and further distributed throughout the grids; (b) medium sized particles (400-600nm) are also observed throughout the grid but not at around the holes; (c) few large sized particles (>1μm) are present in the gold coated region of the grid. Thickness maps (figure 4d - 4f) reveal the typical donut shapes of the discharge products[16].
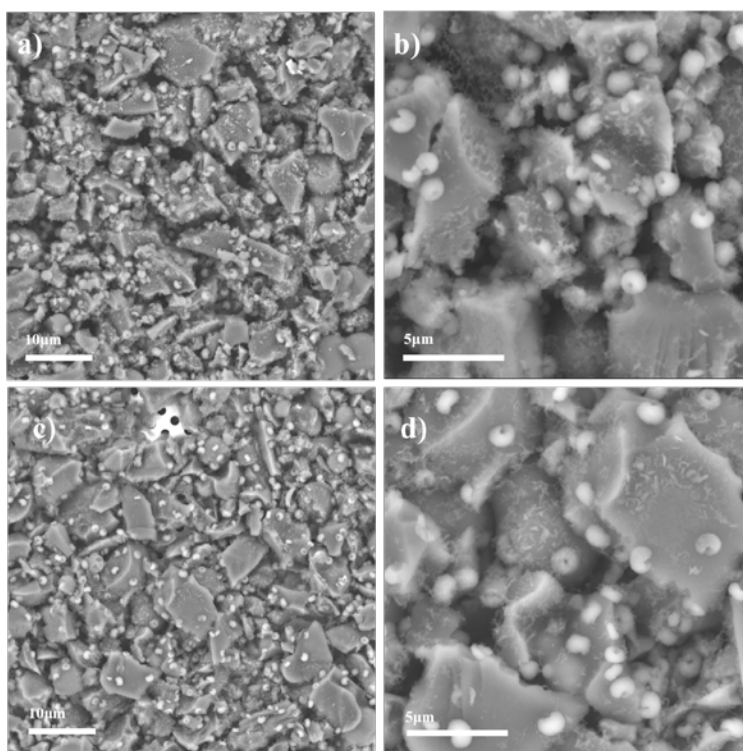

Figure 4: *Discharge products formed at various locations on the Au coated TEM grid is shown using BF-TEM images (a-c) and thickness map using EFTEM imaging (d-f).*

Li_2O_2 can be formed directly at the electrode surfaces or in electrolyte and then get deposited on the electrode surface. Depending upon the donor number of the electrolyte solvent phase formation or electrode surface formation dominates. For electrolyte with low LiO_2 solubility (low donor number) Li_2O_2 mainly forms at the electrode surface. In contrast, good LiO_2 solubility (high donor number) leads to Li_2O_2 growth in solution before deposition on the electrode surface. As TEGDME

has medium donor level both solution phase growth of Li_2O_2 and electrode surface growth are probable at low current densities. Thus we can argue that at least part of the discharge products visible on the gold-coated TEM grids are formed in the electrolyte before deposition on the gold surface. For these discharge products gold is unlikely to act as a catalyst.

Intuitively, the edges around the holes of the TEM grids are the most suitable position for the growth of discharge product as they have direct access to the incoming oxygen. In order to form a discharge product at any other position on the grid, either the oxygen has to be dissolved in the electrolyte or absorbed by the gold layer. To check our assumption, and to find any possible difference between the solution phase grown Li_2O_2 and Li_2O_2 grown on the electrode surface we replaced

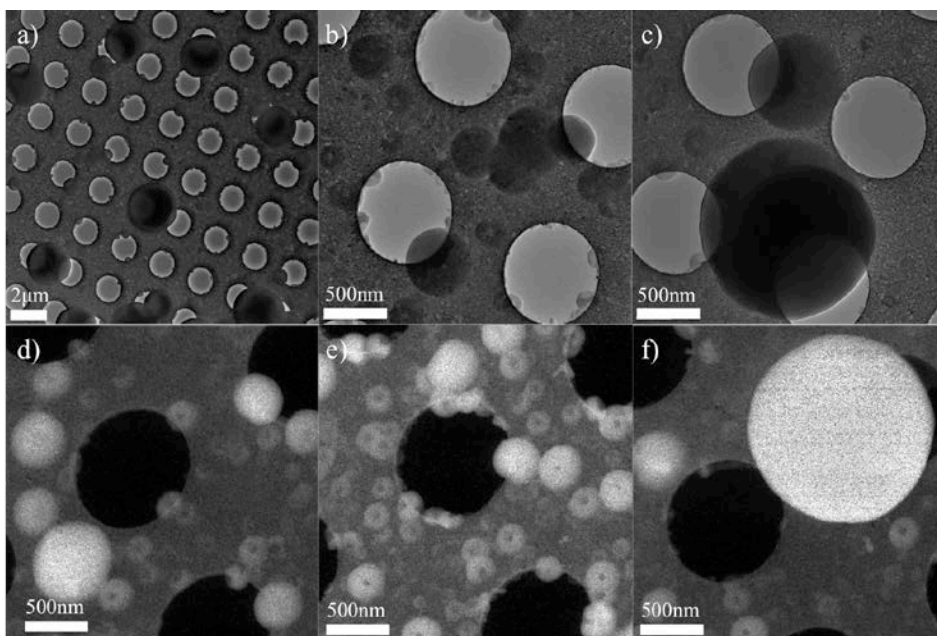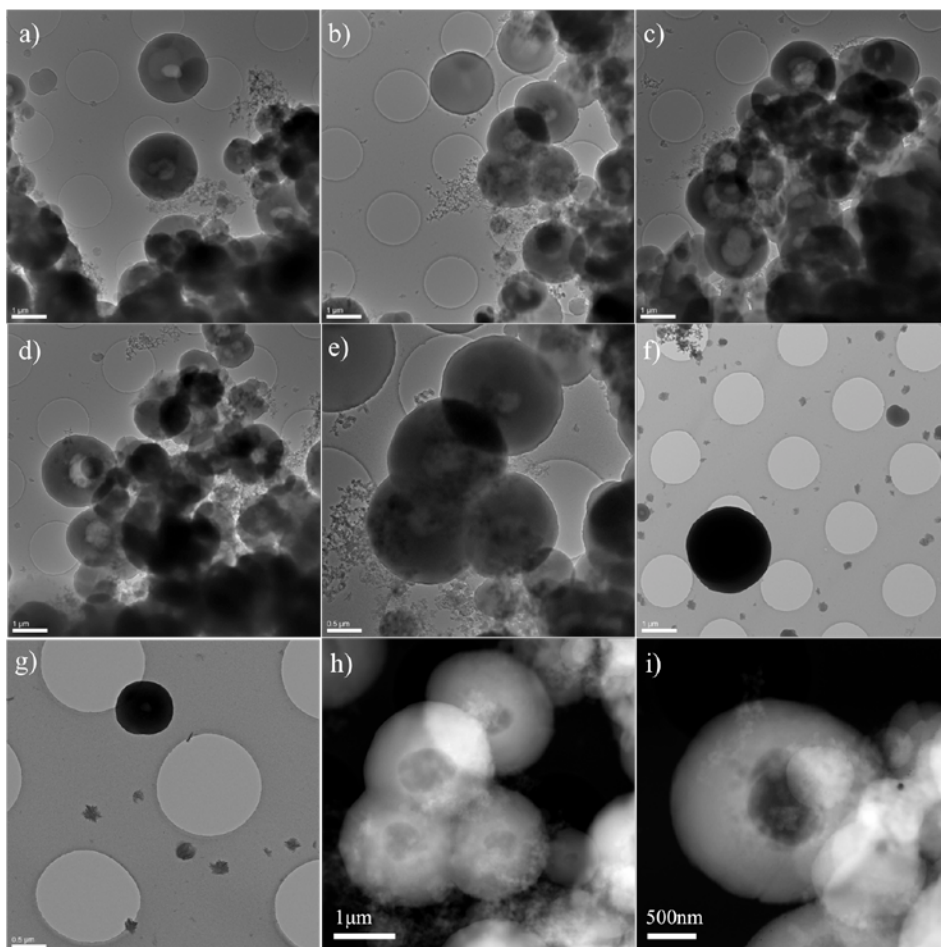*Figure 5: Discharge products formed at various locations on the TEM grid is shown using TEM images (a-g) and STEM images (d-f).*

the gold-coated TEM grids with non-coated TEM grids as substrates. Even in the non-coated TEM grid a thin layer of amorphous carbon is present. But, this carbon is believed to be non conductive or at least poorly conductive. Thus due to lack of electrical conductivity surface growth of the Li_2O_2 should be greatly reduced. Like activated carbon, Super P particles are also widely used as porous carbon electrode material in Li-O_2 battery[17,18]. Since the activated carbon particles are too thick ($\geq$10μm) to be visualized in TEM without further modification, we choose Super P particles to check whether electrode surface has any affect on the morphology of the deposited Li_2O_2. For this we dispersed small amount of Super P particles on the grids before assembling the battery.

Figure 5 shows the discharge products formed at various locations of on the non-Au coated TEM grid. One of the main differences from gold-coated TEM grid is the absence of particles at the edges of the holes, as can be seen from the TEM (Figures 5a-5g) images. Here, big sized Li_2O_2 particles (>1μm) are seen mainly in form of clusters (Figures 5a-5e; 5h-5i). Further no significant difference can be noticed between particles on the grid or on the super P particles. Based on this observation we can argue that in the gold-coated TEM grids the observed big sized particles are likely to be formed in the electrolyte and further deposited on the grid. In few areas of the uncoated TEM grid flake like Li_2O_2 can be seen (Figures 5f-g). These Li_2O_2 flakes are likely to be formed in the electrolyte during initial stage of the discharge process. The visualization of initial stage discharge products is key to the understanding of Li-O_2 battery mechanism.

4. Conclusion

Loss of details about the surroundings of the discharge products during the sample preparation is one of the key concerns, which limits the application of TEM in Li-O_2 battery research. In this study we have used conventional holey carbon TEM grids as porous cathode support and confirm the discharge products form on the TEM grid is representative of the bulk. We have seen that presence of gold forces surface growth of Li_2O_2 and distinguish the solution phase Li_2O_2 from Li_2O_2 grown on electrode surface. Further using the TEM grid initial stage discharge product is visualized. The simplistic nature of the study will ensure widespread use of TEM to understand the mechanisms of Li-O_2 battery directed towards practical realization of Li-O_2 battery.

References

1. McCloskey BD, Bethune DS, Shelby RM, Girishkumar G, Luntz AC. Solvents ' Critical Role in Nonaqueous Lithium À Oxygen Battery. *J Phys Chem Lett* (2011) **2**:1161–1166. doi:10.1021/jz200352v

2. McCloskey BD, Scheffler R, Speidel A, Girishkumar G, Luntz AC. On the mechanism of nonaqueous Li-O2 electrochemistry on C and its kinetic overpotentials: Some implications for Li-air batteries. *J Phys Chem C* (2012) **116**:23897–23905. doi:10.1021/jp306680f

3. Lee J-H, Black R, Popov G, Pomerantseva E, Nan F, Botton GA, Nazar LF. The role of vacancies and defects in Na0.44MnO2 nanowire catalysts for lithium–oxygen batteries. *Energy Environ Sci* (2012) **5**:9558. doi:10.1039/c2ee21543h

4. Peng Z, Freunberger S a., Chen Y, Bruce PG. A Reversible and Higher-Rate Li-O2 Battery. *Science (80-)* (2012) **337**:563–566. doi:10.1126/science.1223985

5. McCloskey BD, Speidel A, Scheffler R, Miller DC, Viswanathan V, Hummelshøj JS, Nørskov JK, Luntz AC. Twin problems of interfacial carbonate formation in nonaqueous Li-O   2 batteries. *J Phys Chem Lett* (2012) **3**:997–1001. doi:10.1021/jz300243r

6. Lu Y-C, Gallant BM, Kwabi DG, Harding JR, Mitchell RR, Whittingham MS, Shao-Horn Y. Lithium-oxygen batteries: bridging mechanistic understanding and battery performance. *Energy Environ Sci* (2013) **6**:750–768. doi:Doi 10.1039/C3ee23966g

7. Gowda SR, Brunet a., Wallraff GM, McCloskey BD. Implications of CO 2 Contamination in Rechargeable Nonaqueous Li–O 2 Batteries. *J Phys Chem Lett* (2013) **4**:276–279. doi:10.1021/jz301902h

8. Sun B, Munroe P, Wang G. Ruthenium nanocrystals as cathode catalysts for lithium-oxygen batteries with a superior performance. *Sci Rep* (2013) **3**:2247. doi:10.1038/srep02247

9. Lu Y-C, Xu Z, Gasteiger HA, Chen S, Hamad-Schifferli K, Shao-Horn Y. Platinum-Gold Nanoparticles : A Highly Active Bifunctional Electrocatalyst for Rechargeable Lithium-Air Batteries. *J Am Chem Soc* (2011) **132**:12170–12171.

10. Ates MN, Gunasekara I, Mukerjee S, Plichta EJ, Hendrickson MA, Abraham KM. In Situ Formed Layered-Layered Metal Oxide as Bifunctional Catalyst for Li-Air Batteries. *J Electrochem Soc* (2016) **163**:A2464–A2474. doi:10.1149/2.0111613jes

11. Lu Y-C, Crumlin EJ, Carney TJ, Baggetto L, Veith GM, Dudney NJ, Liu Z, Shao-Horn Y. Influence of Hydrocarbon and CO 2 on the Reversibility of Li–O 2 Chemistry Using In Situ Ambient Pressure X-ray Photoelectron Spectroscopy. *J Phys Chem C* (2013) **117**:25948–25954. doi:10.1021/jp409453s

12. Gittleson FS, Ryu WH, Taylor AD. Operando observation of the gold-electrolyte interface in Li-O2 batteries. *ACS Appl Mater Interfaces* (2014) **6**:19017–19025. doi:10.1021/am504900k

13. Landa-Medrano I, Olivares-Marín M, Pinedo R, Ruiz de Larramendi I, Rojo T, Tonti D. Operando UV-visible spectroscopy evidence of the reactions of iodide as redox mediator in Li–O2 batteries. *Electrochem commun* (2015) **59**:24–27. doi:10.1016/j.elecom.2015.06.019

14. Lim H, Yilmaz E, Byon HR. Real-time XRD studies of Li-O 2 electrochemical reaction in nonaqueous lithium-oxygen battery. *J Phys Chem Lett* (2012) **3**:3210–3215. doi:10.1021/jz301453t

15.   Ganapathy S, Adams BD, Stenou G, Anastasaki MS, Goubitz K, Miao X, Nazar LF, Wagemaker M. Nature of Li2O2 Oxidation in a Li − O 2 Battery Revealed by Operando. *J Am Chem Soc* (2014) **136**:16335–16344.

16.   Lu Y-C, Kwabi DG, Yao KPC, Harding JR, Zhou J, Zuin L, Shao-Horn Y. The discharge rate capability of rechargeable Li–O2 batteries. *Energy Environ Sci* (2011) **4**:2999. doi:10.1039/ c1ee01500a

17.   Guo Z, Dong X, Wang Y, Xia Y. A lithium air battery with a lithiated Al-carbon anode. *Chem Commun (Camb)* (2014) **51**:2–4. doi:10.1039/c4cc07315k

18.   Cheng H, Scott K. Carbon-supported manganese oxide nanocatalysts for rechargeable lithium-air batteries. *J Power Sources* (2010) **195**:1370–1374. doi:10.1016/ j.jpowsour. 2009.09.030

Appendix C

1. Need for the plastic separator
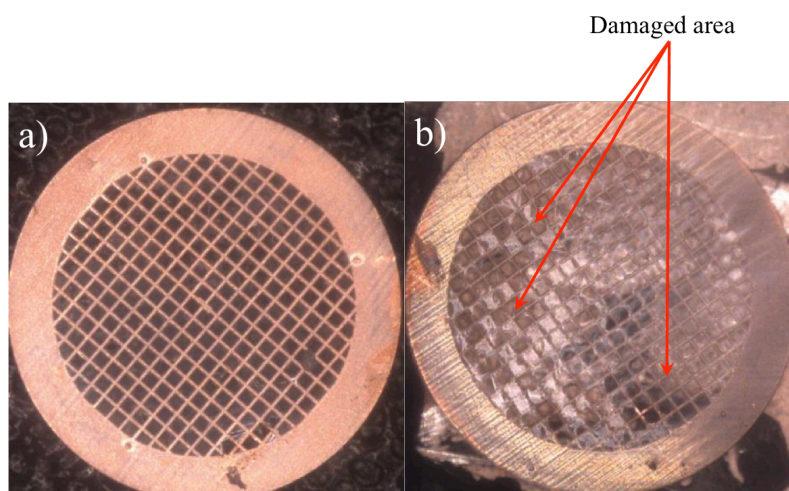
Figure 1: *Comparison of grids (a) with and (b) without a Cell Guard like separator.*

2. Pristine activated carbon surface
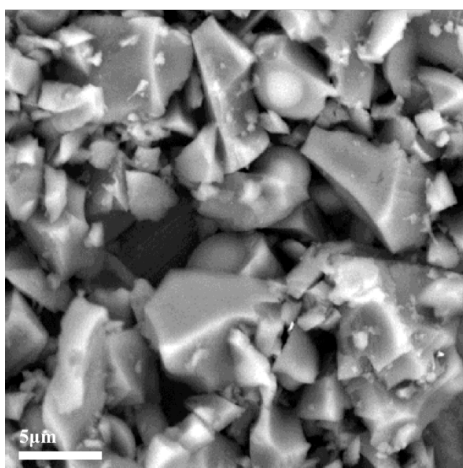
Figure 2: *Surface of pristine activated carbon.*

CHAPTER 6

FABRICATION OF MEMS DEVICES FOR OPERANDO TEM EXPERIMENTS

MEMS chips are the heart of our operando TEM setup. The success of the operando experiments dependent on the design and fabrication of MEMS devices. Four different types of chips are fabricated for different types of experiments. Nano battery chips are used to perform operando TEM battery experiments with solid electrolytes. The MEMS heater chips are used to understand the effect of annealing on the electrodes. Further heating-biasing chips is fabricated for performing of battery cycling at elevated temperature and MEMS nanoreactors are fabricated for performing operando TEM battery experiments with liquid electrolytes. In this chapter the design and fabrication of these MEMS chips are discussed in details.

MEMS based chips are the heart of our *in situ* experiment. The successful fabrication of MEMS chips involves thoughtful designing and weeks of cleanroom processing and further optimization.

Chips are designed using DesignCAD 3D Max and L-Edit software. Design file consists of the patterns that to be written on the substrate using optical or electron beam (e-beam) lithography [1,2]. For optical lithography based chips fabrication these designs are used to fabricate optical masks, which are further used for patterning the substrate. For e-beam lithography these patterns are directly used to steer the electron beam. Examples of the design files used for fabrication of the chips can be seen in figure 2 - 4.

Mainly four different types of chips are fabricated according to the requirements of the research. The nanobattery and nanoreactor chips are fabricated using e-beam lithography; MEMS heaters are prepared using optical lithography; while heating-biasing chips are prepared combining e-beam and optical lithography. All the fabrication steps are carried out in the clean room of Kavli Nanolab at TUDelft unless otherwise mentioned. MEMS heaters are used to study the crystallization process of thin film $LiFePO_4$, described in chapter 7. Chapter 8 describes the use of the nanobattery chips as a platform to assemble single particle battery and to perform operando TEM experiments with solid electrolyte. To study the battery process in TEM in conventional liquid electrolytes nanoreactor chips are fabricated. And to study the battery operation at elevated temperature MEMS heater is combined with the electrical chip. Preliminary results and future direction of research using these two chips are discussed in chapter 9.

1. Basics of chips fabrication

Fabrication of the MEMS chip can be divided into three main fabrication steps: (a) Marker preparation; (b) Preparing electrical connections and (c) preparing electron transparent window.

1.1. Preparing Markers

Since the chip preparation involves several steps of lithography, alignments between different steps are necessary. For this, a set of simple patterns are created in the beginning or during the first lithography step, known as markers. These markers are used for the relative alignment between different lithography steps. Since our chip preparation involves patterning both side of the wafer, alignment between both side's lithography steps should be considered.

There is one basic difference between the makers used in optical lithography markers and e-beam lithography. For optical lithography markers are only present at one side (topside) of the wafer. For writing the backside of the wafer, markers are visualized and aligned using the backside cameras attached in the optical lithography setup. For e-beam lithography though no such camera exists. In this case we take the advantage of precise geometry of anisotropic Si etching by KOH to extend the markers to the other side of the wafer as schematically shown in Figure 1.

1.2. Preparing electrical connections

Electrical contacts are necessary to apply electrical bias to the electrode to (dis)charge the battery. These electrical contacts connect the battery electrodes to the electrical setup, outside the TEM, via electrical TEM holder. We have used noble metals (gold or platinum) for electrical contacts, which are easily compatible with cleanroom fabrication process. A platinum coil embedded in SiN is used in the MEMS heater to locally heat the sample utilizing the Joule heating.

1.3. Preparing electron transparent window

For TEM observation samples must be placed in an electron transparent window and thus electron transparent window is integral part of the TEM MEMS chips. These windows allow visualization of evolution of nanoparticle electrode during battery cycles and/or evolution of structure during annealing process in an in-situ manner. Windows have to be contamination free, stable, and as thin as possible. We used LPCVD grown 20 to 50nm SiN as electron transparent windows for the different chips. Mechanical strength, roughness, contamination are key factors determining the quality of the SiN windows.

2. Key fabrication steps

In the following section the procedures used for fabrication the MEMS chips are discussed in brief. The fabrication procedures can be categorized as: (a) substrate cleaning; (b) lithography; (c) deposition and (d) etching [3].

2.1. Substrate Cleaning

Contamination free chips are absolute necessary for a successful *in situ* experiment. Thus the wafers/chips should be resist or contamination (organic,

inorganic) free. To achieve this following cleaning steps are used at various stages of chips fabrication.

Nitric acid cleaning. This is used for removing resist and organic contaminants from wafer and chips. Typically the wafers/chips are dipped into the fuming Nitric acid, 100% concentration, for 10 minutes at room temperature. Afterwards the wafers/chips are rinsed in abundant water and dried with N_2 gun.

Oxygen plasma cleaning. This is used for removing resist and organic contaminants from wafers. Typically the wafers/chips are placed in the PVA TePla 300, microwave plasma system with oxygen flow 200 sccm, power 500 Watt, chamber pressure 0.8 mbar for 5-10 minutes. [i]

Acetone cleaning. This is used for gently removing resist residues from wafer and chips (not as effective as oxygen plasma or nitric acid). Typically wafers/chips are dipped into hot acetone (~54°C). Cleaning time varies according to the type of resist and thickness (typically 30 minutes to 2 hours). After the cleaning the wafers/chips are immediately dipped into isopropanol alcohol (IPA) and dried with N_2 gun.

RCA cleaning. This is used for cleaning wafers/chips before SiN deposition in LPCVD. The standard RCA cleaning involves two cleaning steps: RCA-1 and RCA-2 at 70°C. RCA-1 removes organic contaminants, while RCA-2 removes metal contaminants. RCA-1 is actually a solution of NH_4OH: H_2O_2: H_2O with ratio 1: 1: 5, while RCA-2 is a solution of HCl: H_2O_2: H_2O with ratio 1: 1: 5. Typically wafers/chips are dipped into RCA-1 followed by RCA-2, in between with rinsing with water (at RT), for 10 minutes each. Finally the wafers/chips are rinsed with abundant water and dried with N_2 gun.

2.2. Lithography

As mentioned earlier two different types of lithography are used for writing the desired structure necessary for chips fabrication: Optical lithography and e-beam lithography[1]. The lithographic steps consist of (a) coating of resist, (b) exposure to the beam, and (c) developing the written structure. We have only used positive resist (developing leads to dissolution of resist in the beam exposed part) for the fabrication process. Table-1 gives the information about the used resists, typical beam dose and development details.

---

[i] Not suitable for the chips with heating coil due to inductive coupling.

Name of Resist	Used for	Process Description
PMMA (950k, 7% in anisole)	E-beam lithography for patterning markers, lines, grooves and windows.	**Coating:** spin coat ~500 nm thick resist with 5000 rpm, followed by baking of 1 hour on hotplate at 175°C. **Exposure:** e-beam exposure dose: 1000 nC/cm^2 with 100 kV e-beam. **Development:** MIBK:IPA solution with 1:3 ratios for 70 seconds followed by rinsing 50 seconds in IPA.
PMMA (950k, 3% in anisole) /**MMA** (17.5 wt.%, 8% in Ethyl Lactate)	E-beam lithography for patterning electrical contacts.	Coating: First ~300nm of MMA copolymer is spin coated with 3000 rpm, followed by baking of 10 minutes on hotplate at 175°C. Next, ~130nm of PMMA layer is spin coated with 3000 rpm, followed by baking of 20 minutes on hotplate at 175°C. **Exposure/Development:** the same as for PMMA.
AZ5214E	For all Optical lithography steps.	**Coating:** First a layer of HDMS is spin coated to improve the adhesion of the resist with 5000 rpm followed by baking 2 minutes at 180°C. Then AZ5214E is spin coated with 5000 rpm, followed by baking on hotplate for 1 minute at 90°C. Exposure: i-line(365 nm), exposure dose 150 mJ/cm^2 . Development: MF321 for 1 min followed by rinsing in deionized water for 30 seconds.
S1818	Protection during dicing	~ 5μm thick layer is spin coated with 1000 rpm followed by baking of 2 min on hotplate at 90°C. Similarly the backside of the wafer is coated.

Table 1: Details about the resist, beam dose and developing agent used for various steps of fabrication.

2.3. Deposition

We have deposited SiN, SiO_2 and metallic films (Au, Pt and Ni) at various stages of fabrication.

CVD. In a chemical vapour deposition (CVD) process gaseous species reacts on a solid surface of wafer (substrate) and the reaction produces a solid phase material. A typical CVD process comprised of four main steps. First, the reacting gaseous species is transported to the surface of the wafer. Second, the gaseous species is absorbed into the surface of the wafer. Third, the surface reaction produces desired coating. Finally the volatile by-products (gaseous reactants) need to be removed from the surface. There are different variant of CVD is available. We have used low pressure CVD (**LPCVD)** and plasma enhanced CVD (**PECVD)** for low stress SiN and SiO_2 deposition respectively.

Evaporation: Temescal 2000 e-beam evaporator is used to deposit Au and Pt while Lybolt evaporator is used to deposit Ni. A 5 nm Cr layer is deposited as adhesion layer in case of Au or Pt. E-Beam evaporation is a physical vapour deposition technique whereby an intense, electron beam is generated from a filament and steered via electric and magnetic fields to strike the source material (target) which vaporized the material. The vaporised particles in vacuum travel directly to the substrate to be deposited in solid form. Deposition rate of 0.5-2 Å/s is used to deposit the metallic films at high vacuum ($< 2\times 10^{-6}$ mbar).

2.4. Etching

Silicon, silicon nitride and silicon oxide are etched using different wet etching (KOH and HF) and dry etching (reactive ion etching) during the fabrication steps.

KOH etching. KOH etching of Si is used to prepare breaking/dicing lines, e-beam markers, grooves for lithium, and electron transparent windows. KOH etching rate depends on the crystallographic direction, Si{100} etches 400 times faster than Si{111}, results in anisotropic etching. This etching anisotropy should be taken into consideration during chip designing, which results much shorter (100) surface than the corresponding opening. The etching rate itself varies with the concentration and solution temperature. We used KOH solution (KOH: H_2O 1:2 weight ratio) at 90ºC, which results in etching rate 100μm/hour for of Si<100>. At same conditions the etching of SiN is 1-2 nm/hr. Thus SiN is used as mask and/or stopping layer.

We have varied the SiN openings and KOH etching time to fabricate different features on our chip as shown in figure 1. We used time-limited etching for preparing groove for lithium (scheme 2). Self-limited etching is used to create breaking line or dicing line. In this case four {111} intersect each other at the stopping point (scheme 1). Markers and the electron transparent window are fabricated via KOH etching through the wafer, which stops at the SiN layer (scheme 3 and 4).
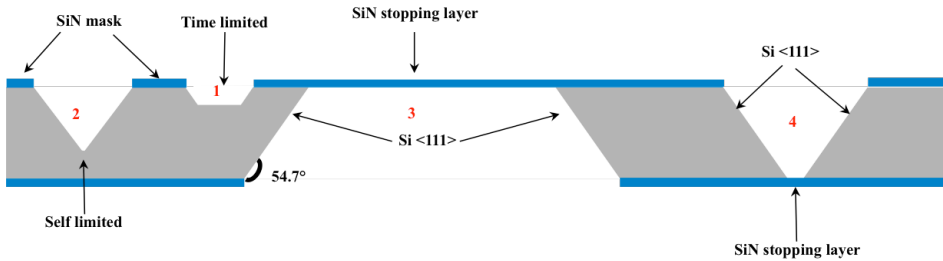

Figure 1: Schematics shows different trenches prepared on Si <100> wafer using anisotropic KOH etching.

HF etching: Diluted (7:1 with water) buffered Hydrofluoric (BHF) acid (HF is mixed with NH_4F) is used for selectively etching SiO_2 on top of Silicon. The e-beam resist (PMMA) is very stable in HF and thus can be used as mask, for selective etching of SiO_2 layer. For etching of 3μm PECVD SiO_2 substrate is dipped into BHF for 10 minutes.

Reactive ion etching. Reactive ion etching (RIE) is a directional etching process utilizing ion bombardment to remove material. We used RIE to etch SiN with Argon and CHF_3 gases (individual flow rate of 25 sccm) at 8 μbar with RF power 50 Watt in Lybolt F system. The etching rate of SiN (23±2 nm/min) is at least 3 orders higher than the etching rate PMMA or PMMA/MMA resist, which is used as etching mask.

Deep reactive-ion etching. Deep reactive-ion etching (DRIE) is a highly anisotropic etching process used to create deep trenches with high aspect ratios. Typical Bosch process, proceed by repeating of etching-deposition cycles. First, during the etching cycle highly directional etching is performed by Sulfur hexafluoride [SF_6] gas. This is followed by a deposition cycle where a passivation layer is deposited with Octafluorocyclobutane (C_4F_8) gas. The etching and deposition cycle lasts for 20 and 5 seconds respectively. During the next etching cycle highly directional etching ions that bombard the substrate, attack the passivation layer at the bottom of the trench but not along the sides. Thus the passivation layer at the bottom of the trench is removed and exposed

to the chemical etchant, but the sidewalls remain intact. After the etching cycle, deposition cycle starts again and the process continues till the desired etching is achieved. The etching rate achieved with the as mentioned operating parameters is 5-6μm/min. We used BOSCH etching to prepare the O-ring groove in the top chip of the nanoreactor. For precision on the etching depth etching rates are checked around half way through the etching by measuring the groove depth with a profilometer. The depth of the groove is set to 295μm, optimized for the leak tightness of the nanoreactor with the *Viton ®* O-rings. Since the e-beam photoresist such as PMMA or PMMA/MMA are not stable under the SF_6 plasma, 3 μm thick SiO_2 is used as mask for selective etching of Si.

Lift off. "Lift-off" is a typical method in microelectronic fabrication method for patterning deposited. For this first, the pattern is defined on a substrate using resist (PMMA/MMA) and EBL. Next the metallic film (Au/Pt/Ni) deposited all over the substrate, covering the resist as well as areas resist free (pattered) area. During the actual lifting-off process, the substrate is dipped into a hot acetone bath. The removal of resist by acetone from under the metallic film takes off the film with it. Thus only the area where the metallic film is directly deposited on the substrate remains intact. Retention and re-deposition are the main problems of lift off, especially when the metallic lines are closely spaced. Ultrasonic bath and immediate transfer of the substrate to IPA solution greatly help to prevent this. Typical lift of takes 10 minutes (for Pt) to 2 hours (for Au). The variation is due to the different stress of the Au and Pt film on SiN.

3. Fabrication of Nanobattery chips

To study the delithiation mechanism in $LiFePO_4$ inside TEM (Chapter 8) we have used simple chip consist of electrical connection and 30nm thick electron transparent SiN window. These chips are prepared using e-beam lithography. For convenient writing time 20mm×20mm substrate are used and from each substrate 9 chips with 3.4mm× 2.8mm are prepared. Figure 2 shows the design file of such fabrication. One of the important parts of this chip fabrication is to maintain the exact dimension of the chips, to ensure fitting in the TEM holder slot. Generally small chips are diced using a dicing machine, which uses a thin diamond blade (typical width of 50μm). However the thin and big windows (800μm×200μm) in these chips are prone to breakage during such dicing. To overcome this we used 'breaking lines', 150μm deep from both side of the substrate. So when the substrates are broken mechanically, to separate the chips, they always break along the desired lines, resulting in chips with exact dimensions.

Figure 2: Shows the design file for the Nanobattery chips prepared with Design CAD 3D Max for e-beam lithography. Different colours represent different layers.

Step by step fabrication process is given in table-2.

Step No.	Fabrication Step	Description
1.	Substrate preparation	➢ Start material: double side polished 400µm thick 4inch Si <100> wafer. ➢ Removal of native oxide with diluted BHF (BHF:water =1:7) cleaning. ➢ RCA cleaning to remove the organic and metallic contaminations ➢ 100nm SiN deposition in LPCVD. ➢ Coating of S1818 resist for protection from dicing. ➢ Wafer is diced in dies of 20mm×20mm dimension using Disco dicer. ➢ Resist stripping with acetone, oxygen plasma and cleaning with HNO_3.
		➢ EBL using single layer PMMA resist with the pre-designed

2.	Preparation of markers and breaking lines (topside)	➤ pattern (resolution 120nm). ➤ RIE to remove SiN from the patterned open windows using the resist as etching mask. ➤ Resist stripping in acetone. ➤ Wet Si etching in KOH 33% solution using the patterned SiN as mask and etch stop layer.
3.	Thin SiN deposition (for the electron transparent windows)	➤ Removal of the rest of SiN from the topside using RIE. ➤ RCA cleaning (extra HF cleaning needed, if it is not done immediately). ➤ Deposition of 30 nm SiN using LPCVD.
4.	Preparation of metallic electrodes	➤ EBL using double layer PMMA/MMA resist on the topside of the substrate with the predesigned pattern (resolution of 20 nm for the electrode and 120 nm for the course contact). ➤ Evaporation of 3 nm Cr / 97 nm of Au on the topside of the substrate. ➤ Liftoff of the Cr/Au metal.
5.	Preparation of windows and breaking lines (backside)	➤ EBL using single layer PMMA resist with the pre-designed pattern on the backside of the substrate (resolution 120nm). ➤ RIE to remove SiN from the patterned open area using the resist as etching mask. ➤ Resist stripping in acetone. ➤ Wet Si etching in KOH 33% solution using the patterned SiN as mask and etch stop layer.
6.	Substrate cleaving & cleaning	➤ Coating of S1818 resist to prevent any silicon particles on the chips during cleaving. ➤ Cleaving manually along the breaking lines. ➤ Resist stripping using acetone and oxygen plasma and cleaning with HNO_3.

Table 2: *Details of fabrication steps for the Nanobattery chips.*

4. Fabrication of MEMS heater

Two different types of heaters are fabricated for the operando studies. The heaters with thin SiN windows (20nm) are used for the studying the crystallization process of thin film LiFePO$_4$.
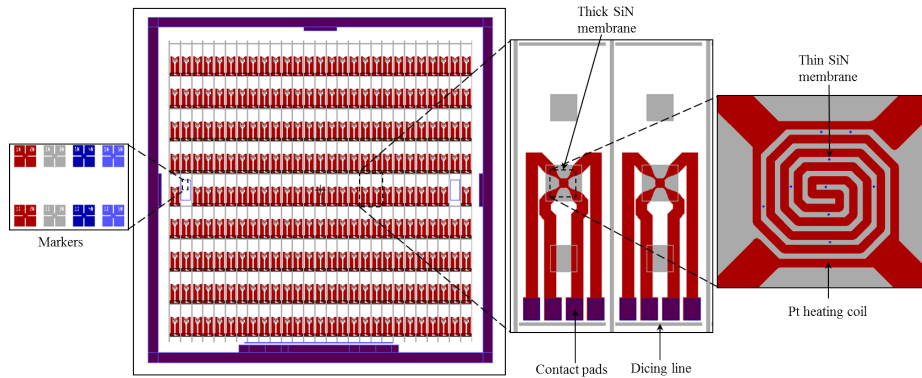
Figure 3: *Shows the design for preparing Optical lithography mask. Different layers and markers are indicated.*
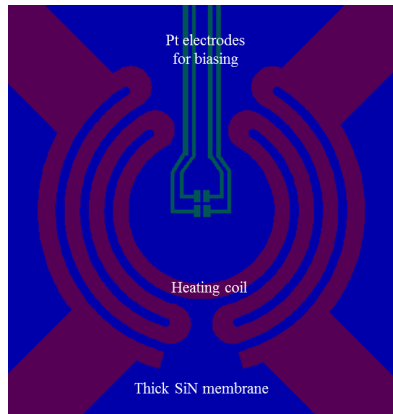
Figure 4: *Shows the design of central part of the flat-center heater, containing the Pt heating coil and Pt electrodes on thick SiN membrane.*

4.1. Fabrication of MEMS heater with thin windows

Step No.	Fabrication Step	Description
1.	SiN deposition (part 1)	➢ Starting material: single side polished 525μm thick 4inch Si <100> wafer. ➢ Removal of native oxide with HF cleaning. ➢ Removal of metallic/organic

		contamination with RCA cleaning. ➢ Deposition of 400 nm SiN with LPCVD.
2.	Preparation of heating coil[ii]	➢ Deposition of 20 nm Tantalum/ 180 nm Platinum on the front (polished) side of the wafer. ➢ Optical lithography with designed dark field mask (for heating coil) using AZ5214E resist. ➢ Etching of the patterned metal layer with ion beam milling using photoresist as mask. ➢ Resist stripping using acetone and oxygen plasma.
3.	SiN deposition (part 2)	➢ RCA cleaning. ➢ Deposition of 400nm SiN with LPCVD.
4.	Preparation of thin windows	➢ Optical lithography with designed bright field mask (for holes) using AZ5214E resist on the front side of the wafer. ➢ RIE to remove 800 nm SiN using the photoresist as mask. ➢ Resist stripping with acetone and oxygen plasma. ➢ RCA cleaning. ➢ Deposition of 20 nm SiN with LPCVD.
5.	Preparation of contact pads	➢ Optical lithography with designed bright field mask (for contact pads) using AZ5214E resist on the front side of the wafer. ➢ RIE to remove 420 nm SiN using the photoresist as mask. ➢ Resist stripping with acetone and oxygen plasma.
		➢ Optical lithography with designed bright field mask (for windows and dicing lines) using AZ5214E resist on the backside of the wafer. ➢ RIE to remove 420 nm SiN using

---

[ii] *This step is performed at MESA Institute at Twenty University, The Netherlands.*

6.	Preparation of heater membrane	the photoresist as mask. ➢ Resist stripping with acetone and oxygen plasma. ➢ Wet Si etching in KOH 33% solution using the patterned SiN as mask and etch stop layer.
7.	Dicing & cleaning	➢ Coating of S1818 resist as protection layer during dicing. ➢ Dicing the wafer into individual chips (3.4mm×10mm) using Disco dicer. ➢ Resist stripping with acetone and oxygen plasma and final cleaning with HNO_3.

Table 3: *Details of fabrication steps for the MEMS heater with thin windows.*

4.2. Fabrication of flat center MEMS heater with metal electrodes

Fabrication of flat center MEMS heater with metal electrodes can be divided into two parts: (a) fabrication of the heater, (b) fabrication of the electrodes.

Heater fabrication part is almost same as described in Table-2, but the absence of step 4 (since there is no thin window) and instead of dicing individual heaters in step 7 the wafer is diced in blocks of 20mm×20mm.

For the fabrication of the electrodes EBL is used. Fabrication of metal electrodes is same as described in the step 4 in Table-2, only Au is replaced by Pt. Sets of Pt markers, which are introduced during fabrication of the heating coil, are used for alignment. At the end, the 20mm×20mm blocks are diced into individual chips following the step 7 in Table-3.

5. Fabrication of Nanoreactors

In situ TEM allows the possibility to charge-discharge a battery composed of a single nanoparticle electrode [4–7]. However, the high vapour pressure aprotic electrolytes which are commonly used in different batteries are not high vacuum compatible and thus cannot be introduced directly in TEM like the solid-state electrolytes. Recent advances in the MEMS lead to fabrications of first liquid chips allowing insertion of high vapour pressure aprotic electrolytes inside the TEM by enclosing the liquid inside two electron transparent windows [8–10]. However, the liquid cell TEM is in its infancy and requires further improvement in terms of stability and resolution.

In our group at TUDelft, we had developed a closed 'nanoreactor' system based on top and bottom chips [11]. The nanoreactor allowed us to introduce different gases and perform heating experiments. We have used the existing nanoreactors chips as the basis for fabricating liquid cell chips for battery application. For battery cycling we need to apply electrical biasing and introduce liquid into the nanoreactor. Thus we have redesigned the existing nanoreactor chips to achieve these functionalities. The bottom chip of the nanoreactor consists of two metal electrodes to apply bias to the battery cathode/ anode. Presences of 200nm thick spacers on the bottom chip act as a liquid channel and simultaneously separate the top and bottom chip (Figure 5a). We have considered the following issues to optimize the nanoreactor design for better stability and resolution.

Window thickness. The electron transparent window has to be strong enough to sustain the pressure different between the inside (electrolyte) and outside (TEM vacuum) of the nanoreactor, this puts the lower limit on the window thickness. On the other hand, thicker window will result in a poor image resolution. Thus the required image resolution puts the upper limit on the thickness. Our nanoreactors have 50nm thick SiN window.

Window dimension. The bulging of the windows, caused by the pressure difference between the inside and outside of the nanoreactor, should be minimized. Bulging results in increased electrolyte thickness in the viewing direction and thus limits the resolution. Since the shorter window dimension mainly determines the degree of bulging [12], to optimize the field of view and bulging we fabricate nanoreactor with $10\mu m \times 200\mu m$ windows.

Biasing electrodes. During our preliminary experiments we found that gold is not stable against Li-ions insertion ($\sim 0V$ vs. Li/Li^+) and thus we choose Pt as biasing electrode.

Groove for Na or Li. In order to investigate the performance of electrode materials it is common practice to test them in a half-cell i.e., with respect to Li metal (in Li-ion battery) or Na metal (in Na-ion battery). Use of Li/Na make sure the performance of the battery is determined the performance of the electrode material under investigation. So to visualize the evolution of electrode materials during battery (dis)charging presence of Li/Na is necessary inside the nanoreactor.

Due to air sensitive nature of Li/Na it's very difficult to use any conventional TEM specimen method to prepare thin Li/Na sample. Cutting the metal using a doctor blade under an optical microscope inside a glovebox and transferring it

to the chip can be an easier alternative. However it's very difficult to limit the thickness to less than few tens of microns and thus the distance between the top and bottom chips will be determined by the thickness of the metal piece. Thus instead of the spacer, the thick Li/Na would regulate the liquid channel thickness (figure 5(b)) and will be too thick for TEM measurement. We tried to solve this issue by creating an extra groove in the chip to place Li/Na, as shown in figure 5(c).
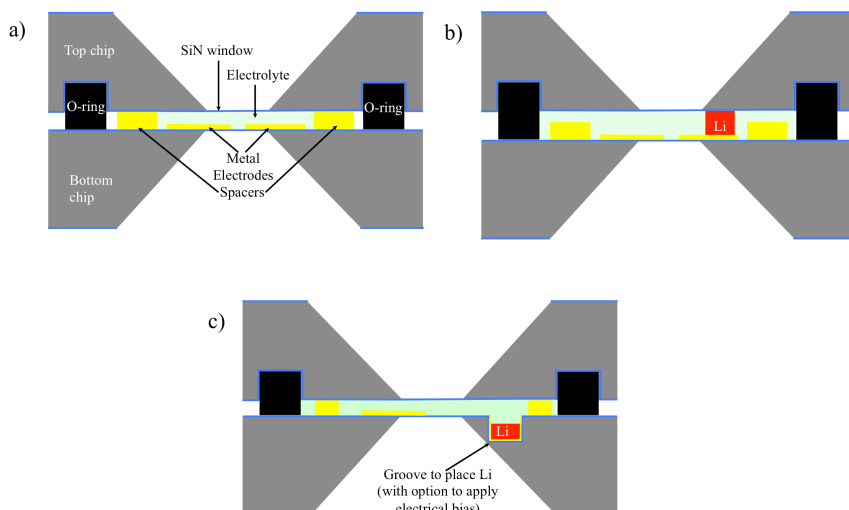
Figure 5: *Schematically shows the nanoreactor chips with liquid electrolyte: a) liquid channel thickness is controlled by the spacer; b) liquid channel thickness is determined by the presence of thick lithium foil; c) placing the lithium in the groove allows the liquid channel thickness to be controlled by the spacer. Figures are not to the scale.*
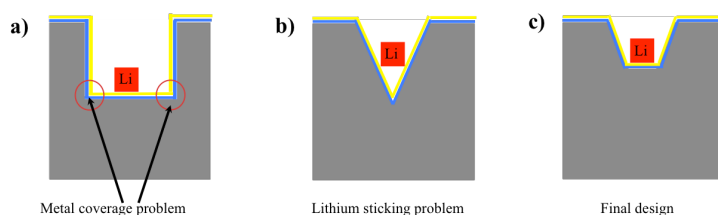
Figure 6: *Shows the different type of groove prepared for placing lithium: a) BOSCH etching leads to electrical connection problem; b) self-limited KOH etching has lithium-sticking problem; c) time-limited KOH solves the issues. Figures are not to the scale.*

Even though the idea sounds simple enough, many modifications of the groove design were necessary to reach the final one. First, the groove is prepared using BOSCH process, which gives an almost vertical groove wall. However problem came due to incomplete metal connection at the edge of the groove as depicted

in the schematic (Figure 6(a)). Next, a triangular groove was prepared with self-limited KOH etching (Figure 6(b)). This triangular groove solved the electrical disconnection problem. However, due to the smooth groove wall lithium piece started to float once electrolyte is introduced. Finally, the trapezium shaped groove is prepared using time-limited KOH etching (Figure 6(c)). It solves both issues regarding previous designs and adopted into the fabrication process.

Figure 7: Shows the design for the nanoreactor bottom chips, prepared using e-beam lithography.

Figure 8: *Design of the nanoreactor top chip, prepared using e-beam lithography.*

Figure 7 shows the design for the nanoreactor bottom chips. These chips are fabricated using e-beam lithography. The fabrication steps of the bottom chip are the same as the Nanobattery chips as described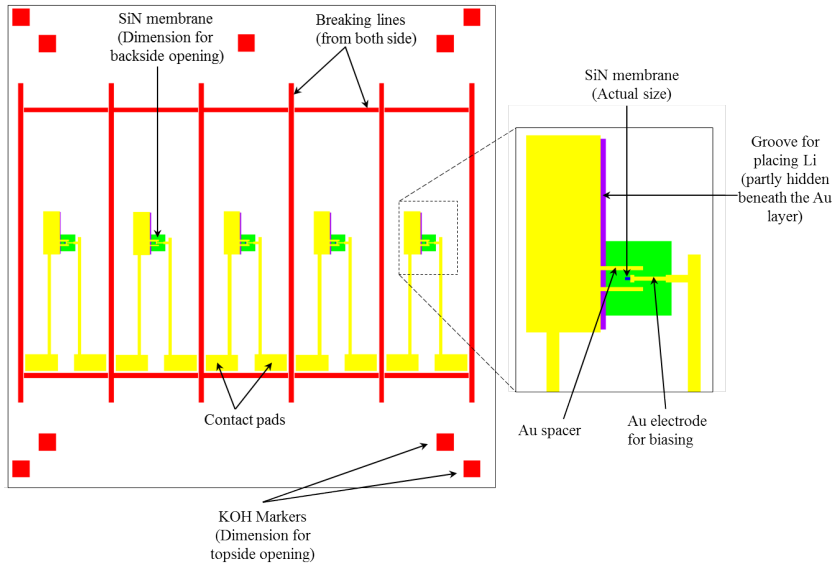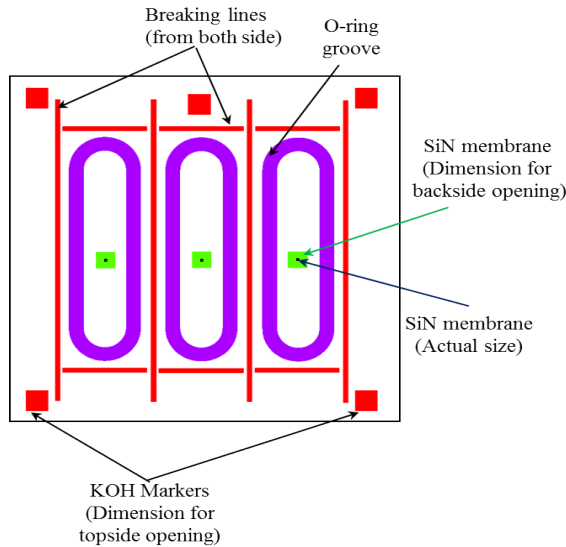 in Table-2 with the addition of the groove preparation step between step 2 and step 3 of Nanobattery chips preparation. For groove preparation EBL is used with the groove design, followed by RIE and KOH etching for 30 minutes to prepare ~ 50μm deep groove. Further, Pt is used as electrode material instead of Au.

The top chip of the nanoreactor (Figure 8) consists of a place to insert commercial O-ring, called as O-ring groove and an electron transparent window. The dimensions of the O-ring groove and the distance from the edge of the chip are optimized for durability and leak tightness of the system. Fabrication steps of the top chip are discussed below.

Step No.	Fabrication Step	Description
1.	Substrate preparation	➢ Same as Step 1 of Table-2.
2.	Preparation of O-ring groove (wafer front side)	➢ Removal of SiN from the topside of the substrate. ➢ Deposition of 3μm SiO$_2$ using PECVD. ➢ EBL using single layer PMMA resist with the pattern for O-ring grooves (resolution 120nm). ➢ Removal of SiO$_2$ using BHF from open area using the resist as mask. ➢ Resist stripping with acetone. ➢ BOSCH etching to remove 295-300μm of Si using SiO$_2$ as mask. Etching rate is estimated using profilometer. ➢ Complete removal of SiO$_2$ using BHF.
3.	Thin SiN deposition (for windows)	➢ RCA cleaning. ➢ Deposition of 50 nm SiN using LPCVD.
5.	Preparation of Windows and breaking lines (bottom side)	➢ Same as Step 5 of Table-2.
6.	Substrate cleaving & cleaning	➢ Same as Step 6 of Table-2.

Table 4: *Details of fabrication steps for the top chip of the nanoreactor.*

Reference

1.   Mack Chris. *Fundamental Principles of Optical Lithography: The Science of Microfabrication*. Wiley (2011).

2.   Tennant DM, Bleier AR. "Electron Beam Lithography of Nanostructures," in *Handbook of Nanofabrication*

3.   Adams TM, Layton RA. *Introductory MEMS: Fabrication and Applications*. (2010).

4.   McDowell MT, Lee SW, Harris JT, Korgel BA, Wang C, Nix WD, Cui Y. In situ TEM of two-phase lithiation of amorphous silicon nanospheres. *Nano Lett* (2013) **13**:758–764. doi:10.1021/nl3044508

5.   Liu XH, Zhong L, Huang S, Mao SX, Zhu T, Huang JY. Size-dependent fracture of silicon nanoparticles during lithiation. *ACS Nano* (2012) **6**:1522–1531. doi:10.1021/nn204476h

6.   Liu N, Wu H, McDowell MT, Yao Y, Wang C, Cui Y. A yolk-shell design for stabilized and scalable Li-ion battery alloy anodes. *Nano Lett* (2012) **12**:3315–3321. doi:10.1021/nl3014814

7.   Harks PPRML, Mulder FM, Notten PHL. In situ methods for Li-ion battery research: A review of recent developments. *J Power Sources* (2015) **288**:92–105. doi:10.1016/j.jpowsour.2015.04.084

8.   Wu F, Yao N. Advances in sealed liquid cells for in-situ TEM electrochemial investigation of lithium-ion battery. *Nano Energy* (2015) **11**:196–210. doi:10.1016/j.nanoen.2014.11.004

9.   Mehdi BL, Qian J, Nasybulin E, Park C, Welch DA, Faller R, Mehta H, Henderson WA, Xu W, Wang CM, et al. Observation and quantification of nanoscale processes in lithium batteries by operando electrochemical (S)TEM. *Nano Lett* (2015) **15**:2168–2173. doi:10.1021/acs.nanolett.5b00175

10.   Gu M, Parent LR, Mehdi BL, Unocic RR, McDowell MT, Sacci RL, Xu W, Connell JG, Xu P, Abellan P, et al. Demonstration of an electrochemical liquid cell for operando transmission electron microscopy observation of the lithiation/delithiation behavior of Si nanowire battery anodes. *Nano Lett* (2013) **13**:6106–6112. doi:10.1021/nl403402q

11.   Erdamar A, Malladi S, Tichelaar F, Zandbergen H. "Closed Cell Systems for In Situ TEM with Gas Environments Ranging from 0.1 to 5 Bar," in *Controlled Atmosphere Transmission Electron Microscopy*

12.   Hawkes PW ed. *Advances in Imaging and Electron Physics* (2011).

CHAPTER 7

IMPROVING THIN FILM BATTERIES USING *IN SITU* TEM STUDIES

In thin film battery research fabrication of electrodes with correct stoichiometry and crystal structure is a big challenge. Using operando TEM we probe the crystallization process of LiFePO$_4$ cathode. The acquired knowledge about the crystallization process will help improving the fabrication process. In the second part of this chapter we focus our attention towards current collectors. In thin film batteries current collectors are often subjected to high current density during fast (dis)charging. Thus it is important to evaluate the performance of the current collector under high current density. Using operando TEM the effect of high current density on Ni film is studied.

Thin film battery is a comparably new field of research but has attracted lots of attention due to recently development in wearable circuits, which have the potential to revolutionize our health monitoring system [1–3]. Add to this the ever-improving microelectronics, which also demands better thin film batteries. Thin film batteries are generally prepared via physical vapour deposition process such as sputtering, pulsed laser deposition (PLD) and evaporation[4–10]. Owing to the capability of forming conformal coatings of thin films, atomic layer deposition (ALD) has shown great potential in deposition and surface modification of electrodes and electrolytes [11–14].

Unlike fabrication of electrodes using chemical methods, fabrication of thin film electrodes with accurate stoichiometry with correct crystal structure is not trivial. The deviation from the correct stoichiometry and crystal structure leads to poor performance of the thin film batteries. Detailed knowledge about the evolution of the electrodes at different stages of fabrication is necessary to optimize the synthesis parameters and in turn improve the performance of the battery. The presence of much thinner electrodes in thin film batteries compare to bulk (in thin film battery electrodes are sub-micron thick compare to sub-millimeter thick electrodes in a typical bulk battery) results in the high (dis)charging current densities in thin film batteries. At these high current densities degradation of current collectors is also possible. So, lots of emphasis should be given in preparing electrodes with correct stoichiometry and studying the effect of high current density on the battery components. In this chapter we probe the fabrication of $LiFePO_4$ cathode and effect of high current densities on Ni current collector using *in situ* TEM.

1. Real time observation of $LiFePO_4$ crystallization

$LiFePO_4$ is one of the most promising cathode materials for Li-ion battery due to its low cost, good thermal stability, high theoretical capacity of 170mAhg^{-1} and high open circuit voltage of 3.5V (vs. Li/Li$^+$)[15–17] .

Nanosizing of $LiFePO_4$ particles prepared using different chemical route synthesis lead to near theoretical capacity, especially at low C rates [16,17]. Magnetron sputtering is commonly used to prepare thin film $LiFePO_4$. However, these thin film batteries delivers much lower capacity [18,19]. To understand the possible issues associated with the low capacity of the thin film $LiFePO_4$ fabrication steps have to be probed.

Fabrication of $LiFePO_4$ film is conducted in a two-step process. First, the thin film is sputtered on a substrate, which also acts as the current collector.

Stainless steel (SS) and Si/SiO$_2$/Pt are examples of commonly used substrates for thin film LiFePO$_4$ battery [18,20,21]. Different substrate temperatures ranging from room temperature to 500^{0}C are reported [22]. A high temperature annealing, generally at 600^{0}C-700^{0}C, follows the deposition step. While deposition at substrate temperature till 350^{0}C resulted in amorphous film, deposition at 500^{0}C resulted in impurity in the film [22]. We choose to deposit the LiFePO$_4$ film at room temperature on SS substrate and monitor the crystallization process using *in situ* TEM. *In situ* TEM studies can provide direct information on the structural, morphological and chemical evolution at high temporal and special resolution during the annealing, which in turn will illustrate optimal synthesis conditions and improve the efficiency of the process.

1.1 Materials and methods

LiFePO$_4$ thin film is deposited on the polished stainless steel (SS) substrate by RF magnetron sputtering. LiFePO$_4$ with 5wt.% carbon obtained from AJA International is used as the sputtering target. LiFePO$_4$ is sputtered in argon atmosphere with base pressure of 10^{-9} mbar at 100 W power. Prior to LiFePO$_4$ deposition the target is pre-sputtered for 30 min in order to eliminate impurities from the surface of the target.

Cross-section TEM samples (lamellas) of dimension ~ 12µm × 3µm × 100nm are prepared using FIB. The lamellas are transferred to the MEMS heater chip using ex-situ lift off process. Fabrication of the MEMS heater chip is described in Chapter 6.

1.2. Result and discussions

Figure 1 shows a typical FIB lamella placed on the thin SiN window of the MEMS heater. The thickness of the deposited film is ~700nm. The SAED pattern acquired from the film revealed that the as deposited film is amorphous.

To check the composition and compositional uniformity of the sample EDS map is obtained. Figure 2 shows the EDS mapping from a typical lamella. The uniform distribution of Fe-K, P-K and O-K signal from the LiFePO$_4$ area suggests uniform composition throughout the deposited film. From the EDS maps acquired from two different lamellas the elemental atomic % of iron, phosphorus and oxygen are found to be 16(±2), 16(±2), 68(±2) respectively. This matches relatively well with the desired Fe: P: O = 1:1:4 atomic ratio for LiFePO$_4$. Fe, Cr and Ni constitute the SS.
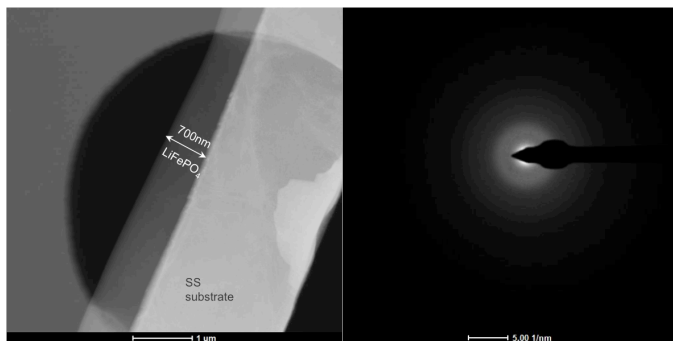
Figure 1: *(a) HAADF-STEM image of the lamella placed on a thin SiN (~20nm) showing the thickness of the LiFePO$_4$ film; (b) SAED pattern obtained from the LiFePO$_4$ shows the amorphous nature of the sample.*
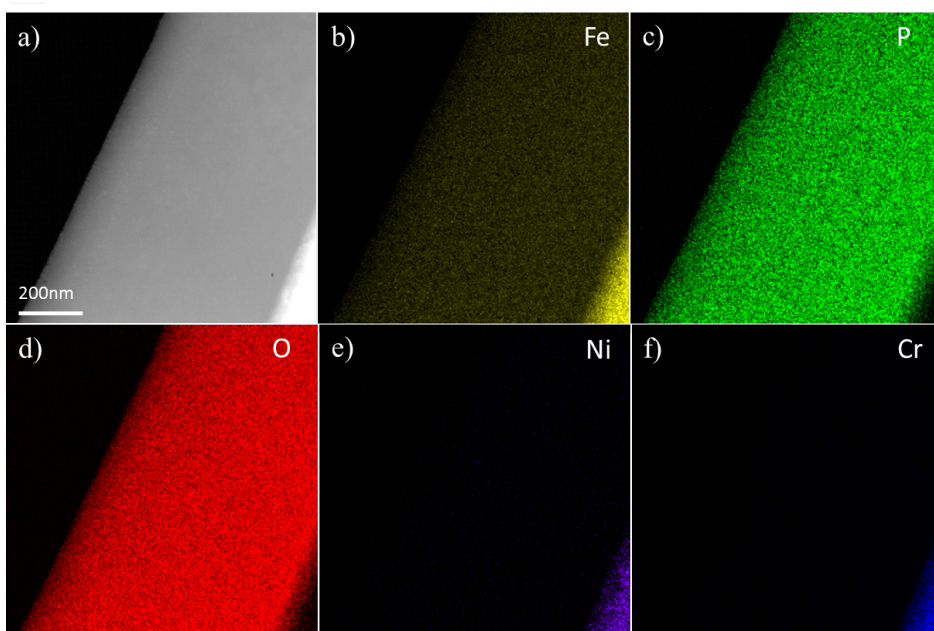
Figure 2: *EDS mapping of as prepared lamella (a) shows uniform distribution of Fe (b), P (c) and O (d) in the deposited film. Presence of Ni (e) and Cr (f) in the SS region can be seen.*

To visualize the crystallization process of LiFePO$_4$ the lamella is heated at 400°C inside TEM. Heating at 400°C initiate the crystallization process. Figure 3(a) shows the presence of 20-50nm crystallites, formed during 5 minutes heating at 400°C. To check the compositional uniformity after the initial crystallization, EDS map is obtained. During EDS mapping, to stop the crystallization process, temperature is kept at 120°C.
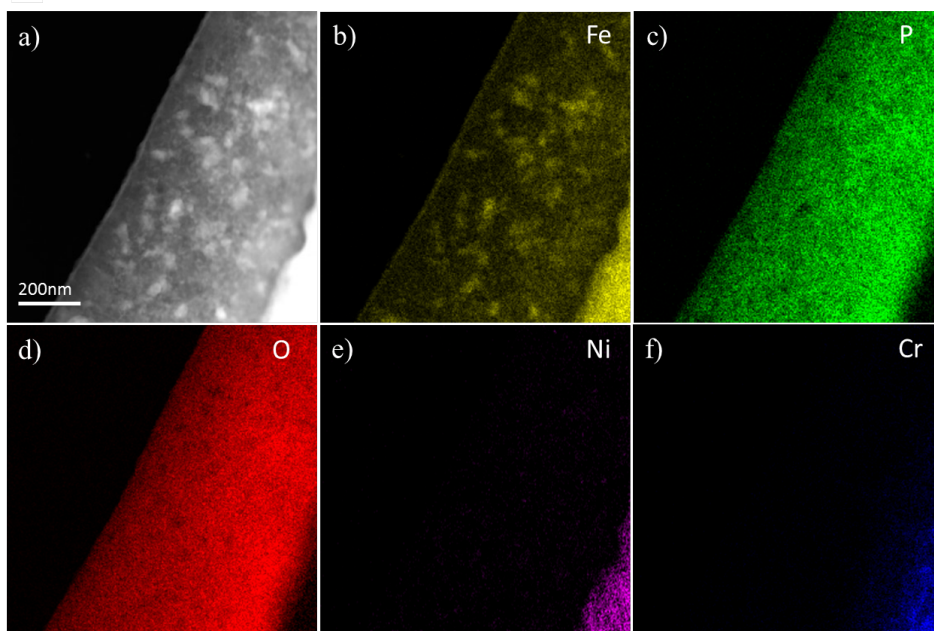
Figure 3: *EDS mapping of the lamella heated at 400°C for 5mins (a) STEM-HAADF image, elemental map of (b) Fe, (c) P, (d) O, (e) Ni and (f) Cr.*
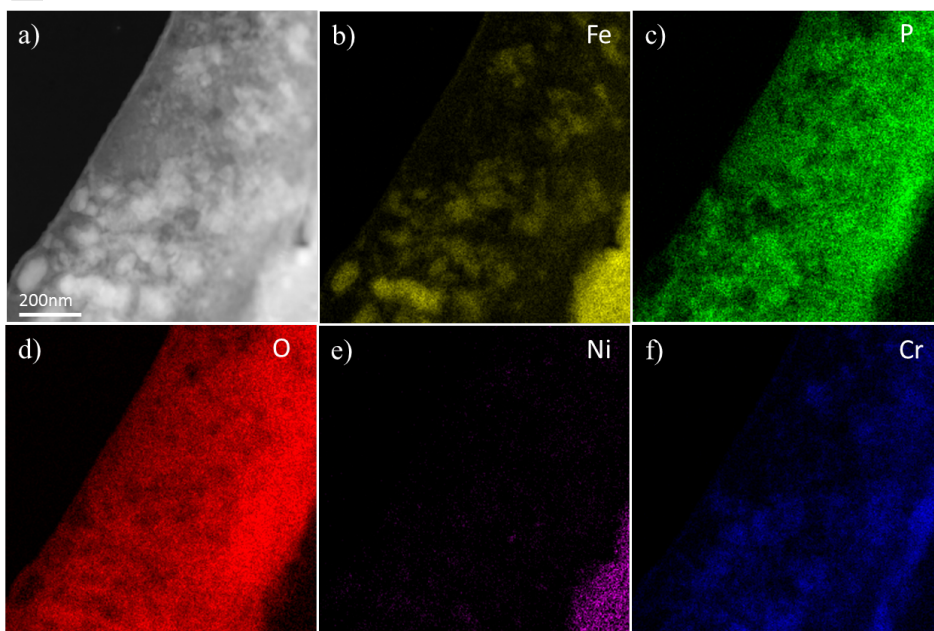
Figure 4: (a) STEM-HAADF image of the lamella after its heated at 600°C for 30mins. Elemental maps of (b) Fe, (c) P, (d) O, (e) Ni and (f) Cr are shown.

EDS mapping reveals that the crystallites have higher iron content compare to the surroundings (Fig. 3(b)-(d)). However, the average ratio of Fe: P: O over the

complete thin film remained same before and after heating. This suggests local aggregation of iron within the thin film. No appreciable present of chromium and nickel in the thin film area can be noticed. This suggests that SS remained stable during the annealing at 400°C.
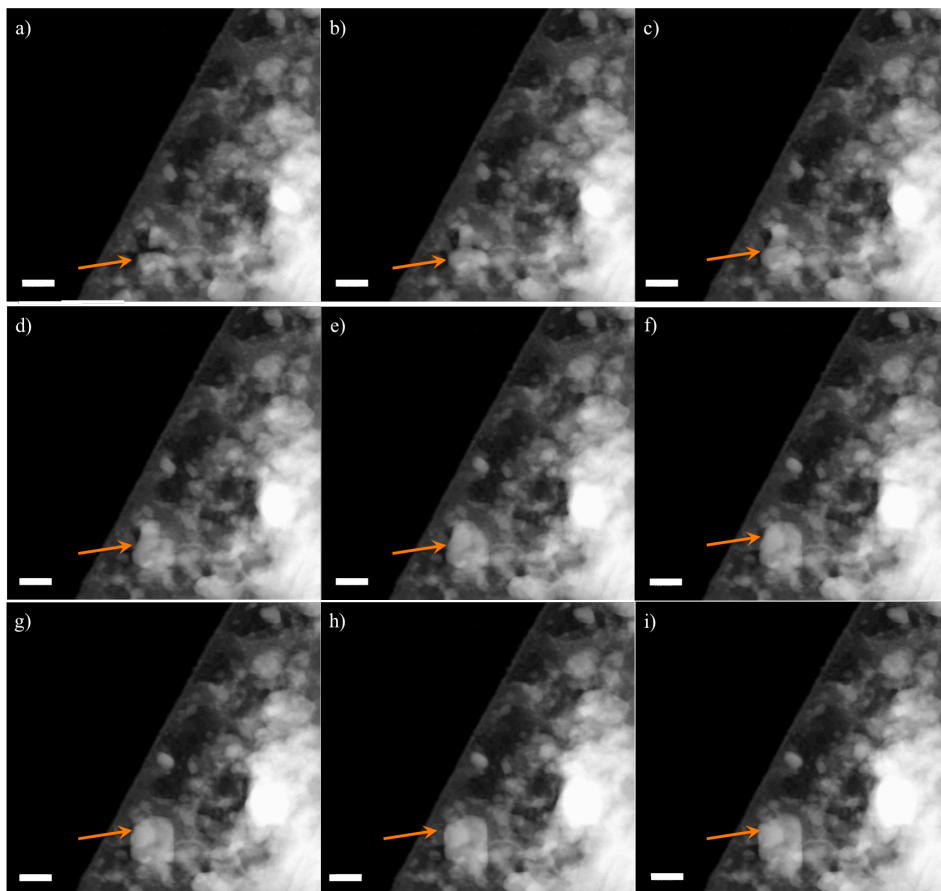
Figure 5: *HAADF-STEM images show the grain growth process during heating at 600°C. (a-i) are captured with interval of 2 seconds. The arrow highlights a typical grain growth.* Scale bar represent 100nm.

To continue the crystallization process, the lamella is further heated at 600°C. Figure 4 shows the EDS map obtained after heating the lamella at 600°C for 30 minutes. Like before during the EDS map, the temperature is decreased to 120°C. The elemental mapping clearly reveals that the crystallites have higher iron and lower phosphorus and oxygen concentration. This undoubtedly shows that crystallites don't have the stoichiometry of $LiFePO_4$. Since in general thin film $LiFePO_4$ batteries are prepared by annealing the as deposited thin film $LiFePO_4$ to temperature $\sim$ 600°C, one can attribute the low battery capacity to the deviation from the $LiFePO_4$ stoichiometry.

Typical sintering effect during annealing at 600°C can be seen from the STEM image series obtained at 2 seconds interval (Figure 5).

The *in situ* heating result is further correlated with the bulk sample. For this the bulk $LiFePO_4$/SS sample is heated to 600°C in argon atmosphere. Figure 6 shows a typical lamella prepared from the heat-treated sample. EDS map confirms the crystallites has higher iron concentration compare to the surroundings, which is similar to the observation during *in situ* heating.
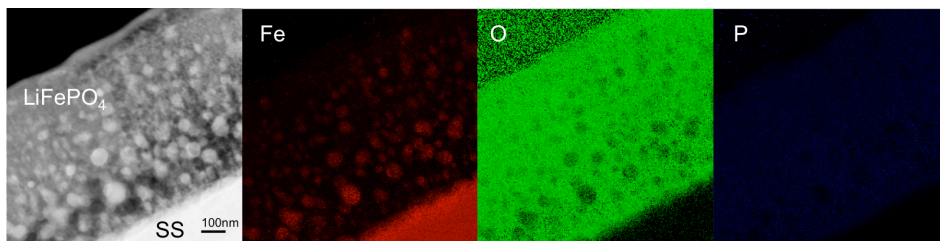
Figure 6: *FIB lamella from the heat-treated sample shows aggregation of crystallites with higher iron concentration.*

A recent Raman study showed, by heating amorphous $LiFePO_4$ sample prepared using sol-gel method, that at 500°C almost total sample constitute of impurity phase[23]. As the annealing temperature was increased to 700°C, impurity phase was reduced and stoichiometric $LiFePO_4$ phase increased. Further increase of annealing temperature to 900°C resulted in a sample almost completely free of impurity. This result suggests a possible need of higher annealing temperature for $LiFePO_4$ crystallization. However, in our case, heating at 600°C already resulted in dissolution of chromium into the film region, as can be seen from Fig. 5(f), suggesting instability of the SS at 600°C. Heating at 700°C resulted in further degradation of SS and dissolution of chromium and nickel to the thin film region.

Preparation of $LiFePO_4$ thin film on high temperature stable substrate (STO/SRO) is underway, which will allow us to study the effect of annealing at higher temperature without any effect from the substrate/current collector.

2. *In situ* TEM observation of electromigration in Ni

Current collectors are used at both sides of the electrodes to draw or supply current from or to the electrodes during the (dis)charge of the battery. Thus during a fast charging or discharging of a battery the current collectors are also subjected to high current density. In the thin film batteries, where the thicknesses of the current collectors are limited, they are subjected to even

higher current density compare to bulk batteries. If thin metallic films are subjected to a high current density, material transfer can occur which finally results in the film destruction, affecting battery performance. Thus the maximum current density that can be applied to a current collector film has to be studied.

Nickel is one of the widely used as current collector at the anode side of Li-ion battery[25,26]. Here we investigated the effect of high current densities on Ni thin film. For this a 15nm thick Ni film is produced by e-beam metal evaporation onto a 100-nm-thick freestanding silicon nitride membrane and patterned using electron beam lithography.

Figure 6(a) shows TEM image of a typical as-fabricated polycristalline Ni bridge with the average grain size of 5 nm. Figures 6(b) and (c) show TEM and STEM images of the bridge after it is exposed to air for a month, hillocks are formed at the Ni bridge. Figures 6(d)–(e) shows EELS spectra from the bridge after exposion to air. Nickel peaks can be clearly identified in both spectra taken from the areas with and without hillock, while the oxygen peak is noticable only in the spectrum taken from the hillock area. It suggests the excess of oxygen in hillock, i.e. Ni bridges oxidise with time. A possible mechanism of oxidation was proposed in article [27]: Initially, a thin oxygen layer is formed on the Ni film, then nucleation of NiO appears and the NiO partcles expand at structural defects on the surface, i.e. grain boundaries, dislocations, impurities, or dirt particles. This suggest the Ni thin flims should not be kept in ambient atmosphere.

In order to study the effect of high current density in Ni, oxidation should be prevented. For this a thin film of Al_2O_3 is deposited on top of the chip right after the main fabrication using ALD at 200°C. Thicknesses of 5 and 10 nm protective Al_2O_3 films are tried. It is found that with a 5-nm-thick protective layer the oxygen enriched hillocks still form at the bridges, while with 10-nm-thick protective layer no hillocks formation is observed even after four months sample storage in ambient atmosphere. Thus we used the 10nm Al_2O_3 coating on the Ni films for *in situ* experiments.
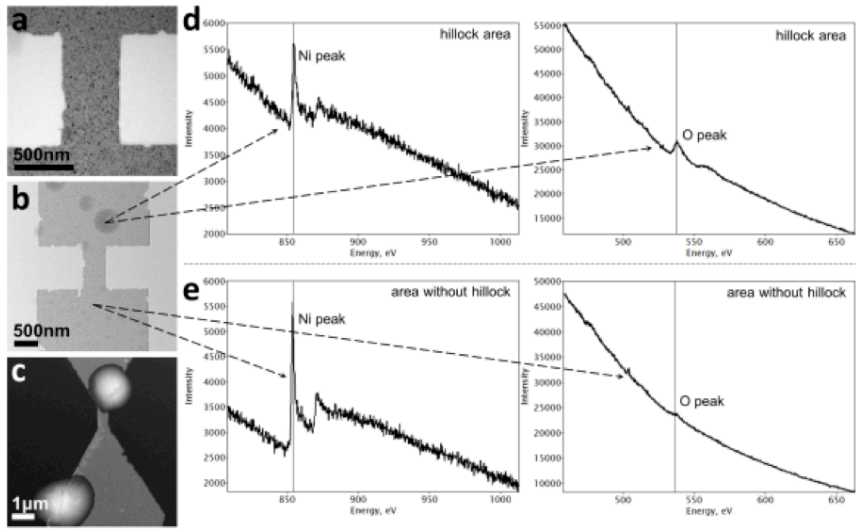
Figure 6. *(a) TEM image of as-prepared Ni nanobridge; (b)–(c) TEM and STEM images of Ni bridges after exposition to air for one month. EELS spectra from the areas with (d) and without hillock (e) taken from the bridge (b).*
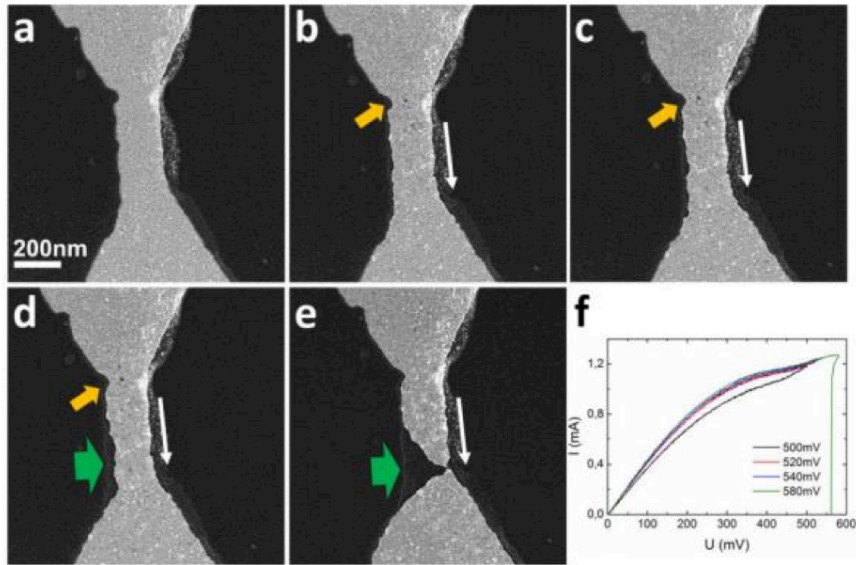
Figure 7. *STEM images of Ni nanobridge showing material transfer during electromigration at 100 K. (a) As-prepared Ni nanobridge with 10-nm-thick Al_2O_3 protective layer deposited on top. (b–d) During electromigration, voids form at the negative side (indicated with yellow arrows); white arrows indicate the direction of electrons. (d–e) At higher electrical current (approx. 1.2 mA) bridge starts to shrink near the positive side (indicated with green arrows) and eventually breaks. (f) I–V curves for four loops with gradually increased maximum voltage (shown in different colours).*

Figure 7(a)–(e) shows STEM images of Ni nanobridge with 10-nm-thick Al_2O_3 protective layer on top taken before electromigration and after each bias-ramping cycle with maximum voltages 500 mV, 520 mV, 540 mV and 580 mV (using custom made electrical setup, "IVVI rack" [28])). Figure 7(f) shows corresponding I–V curves for four voltage cycles applied in a row.

The maximum current is approx. 1.2 mA at which bridge eventually breaks. This highest current corresponds to a current density of $400\,nA/nm^2$, marks the maximum current density that can be applied to the Ni film.

References

1. Jung YH, Lee J, Qiu Y, Cho N, Cho SJ, Zhang H, Lee S, Kim TJ, Gong S, Ma Z. Stretchable Twisted-Pair Transmission Lines for Microwave Frequency Wearable Electronics. *Adv Funct Mater* (2016) **26**:4635–4642. doi:10.1002/adfm.201600856

2. Jiang H, Wang H, Liu G, Su Z, Wu J, Liu J, Zhang X, Chen Y, Zhou W. Light-weight, flexible, low-voltage electro-thermal film using graphite nanoplatelets for wearable/smart electronics and deicing devices. *J Alloys Compd* (2017) **699**:1049–1056. doi:10.1016/j.jallcom.2016.12.435

3. Ghahremani Honarvar M, Latifi M. Overview of wearable electronics and smart textiles. *J Text Inst* (2016) **5000**:1–22. doi:10.1080/00405000.2016.1177870

4. Rongbin Y, Koji O, Baba M. Electrochemical Properties of Amorphous Nb2O5 Thin Film and Its Application to Rechargeable Thin Film Lithium Ion Batteries. *ECS Trans* (2016) **73**:49–55.

5. Nowak S, Berkemeier F, Schmitz G. Ultra-thin LiPON films - Fundamental properties and application in solid state thin film model batteries. *J Power Sources* (2015) **275**:144–150. doi:10.1016/j.jpowsour.2014.10.202

6. Lobe S, Dellen C, Finsterbusch M, Gehrke HG, Sebold D, Tsai CL, Uhlenbruck S, Guillon O. Radio frequency magnetron sputtering of Li7La3Zr2O12 thin films for solid-state batteries. *J Power Sources* (2016) **307**:684–689. doi:10.1016/j.jpowsour.2015.12.054

7. Jung KT, Cho GB, Kim KW, Nam TH, Jeong HM, Huh SC, Chung HS, Noh JP. Influence of the substrate texture on the structural and electrochemical properties of sputtered LiCoO2 thin films. *Thin Solid Films* (2013) **546**:414–417. doi:10.1016/j.tsf.2013.05.135

8. West WC, Hood ZD, Adhikari SP, Liang C, Lachgar A, Motoyama M, Iriyama Y. Reduction of charge-transfer resistance at the solid electrolyte - Electrode interface by pulsed laser deposition of films from a crystalline Li2PO2N source. *J Power Sources* (2016) **312**:116–122. doi:10.1016/j.jpowsour.2016.02.034

9. Transactions ECS, Society TE. 4 4 - 4 2. (2012) **8**:50019.

10. Nakagawa A, Kuwata N, Matsuda Y, Kawamura J. Characterization of stable Solid electrolyte lithium silicate for thin film lithium battery. *J Phys Soc Japan* (2010) **79**:98–101. doi:10.1143/JPSJS.79SA.98

11. Nisula M, Karppinen M. Atomic/Molecular Layer Deposition of Lithium Terephthalate Thin Films as High Rate Capability Li-Ion Battery Anodes. *Nano Lett* (2016) **16**:1276–1281. doi:10.1021/acs.nanolett.5b04604

12. Miikkulainen V, Ruud A, Østreng E, Nilsen O, Laitinen M, Sajavaara T, Fjellvaìšg H. Atomic layer deposition of spinel lithium manganese oxide by film-body-controlled lithium incorporation for thin-film lithium-ion batteries. *J Phys Chem C* (2014) **118**:1258–1268. doi:10.1021/jp409399y

13. Liu J, Xiao B, Banis MN, Li R, Sham TK, Sun X. Atomic layer deposition of amorphous iron phosphates on carbon nanotubes as cathode materials for lithium-ion batteries. *Electrochim Acta* (2015) **162**:275–281. doi:10.1016/j.electacta.2014.12.158

14. Aaltonen T, Nilsen O, Magrasó A, Fjellvåg H. Atomic Layer Deposition of Li2O–Al2O3 Thin Films. *Chem Mater* (2011) **23**:4669–4675. doi:10.1021/cm200899k

15. Guo H, Gao Q. High-performance LiFePO4/C nanocomposites prepared from a micro-reactor based on an unusual water-oil system. *Rsc Adv* (2013) **3**:7245–7248. doi:10.1039/c3ra40577j

16. Guo H, Liu Y, Xi Y, Xu C, Lv Q. Investigation on high performance LiFePO4 nanoplates with the {010} face prominent for lithium battery cathode materials. *Solid State Ionics* (2016) **298**:44–50. doi:10.1016/j.ssi.2016.10.015

17. Doherty CM, Caruso R a., Drummond CJ. High performance LiFePO4 electrode materials: influence of colloidal particle morphology and porosity on lithium-ion battery power capability. *Energy Environ Sci* (2010) **3**:813. doi:10.1039/b922898e

18. Kucinskis G, State S, Bajars G. Kinetic Behavior of LiFePO 4 / C Thin Film Cathode Material for Lithium-Ion Batteries. (2010) **4**:53–57. doi:10.2478/v10145-010-0018-3

19. Bajars G, Kucinskis G, Smits J, Kleperis J. Physical and electrochemical properties of LiFePO4/C thin films deposited by direct current and radiofrequency magnetron sputtering. *Solid State Ionics* (2011) **188**:156–159. doi:10.1016/j.ssi.2010.10.022

20. Hong J, Wang C, Dudney NJ, Lance MJ. Characterization and Performance of LiFePO4 Thin-Film Cathodes Prepared with Radio-Frequency Magnetron-Sputter Deposition. *J Electrochem Soc* (2007) **154**:A805–A809. doi:10.1149/1.2746804

21. Chiu K-F. Optimization of Synthesis Process for Carbon-Mixed LiFePO[sub 4] Composite Thin-Film Cathodes Deposited by Bias Sputtering. *J Electrochem Soc* (2007) **154**:A129. doi:10.1149/1.2404898

22. Zhu X-J, Cheng L-B, Wang C-G, Guo Z-P, Zhang P, Du G-D, Liu H-K. Preparation and Characteristics of LiFePO 4 Thin Film by Radio Frequency Magnetron Sputtering for Lithium Microbatteries. *J Phys Chem C* (2009) **113**:14518–14522. doi:10.1021/jp902560q

23.   Ziolkowska DA, Jasinski JB, Hamankiewicz B, Korona KP, Wu SH, Czerwinski A. In Situ XRD and TEM Studies of Sol-Gel-Based Synthesis of LiFePO4. *Cryst Growth Des* (2016) **16**:5006–5013. doi:10.1021/acs.cgd.6b00575

24.   Nitta N, Wu F, Lee JT, Yushin G. Li-ion battery materials: Present and future. *Mater Today* (2015) **18**:252–264. doi:10.1016/j.mattod.2014.10.040

25.   Wang Y, Liao H, Wang J, Zhu Y, Cheng S. Effects of Current Collectors on Electrochemical Performance of FeS 2 for Li-ion Battery. *Int J Electrochem Sci* (2013) **8**:4002–4009. doi:10.1016/j.jpowsour.2011.09.014

CHAPTER 8

DESIGNING RELIABLE *IN SITU* TEM BATTERY EXPERIMENTS

The unique capability of TEM to resolve the microstructural and chemical evolution of electrode materials during battery operation at high tempo-spatial resolution makes it the method of choice for operando battery experiments. However, the existing open-cell design that uses oxidized lithium as the electrolyte does not allow Li-ions to be (de)inserted from every part of the nanoparticle, which puts restrictions on starting point of (de)intercalation. This may lead to incomplete information about the (de)lithiation mechanism of the electrode material under investigation. To overcome this, two widely applicable open-cell designs are designed for in-situ TEM battery experiments using MEMS-based TEM chip with and without graphene. A thin layer of LiPON as the electrolyte enables Li-ions to be (de)intercalated from every part of the electrode. Using LiFePO$_4$ electrodes in these setups, the importance of overlap between electrode, electrolyte and current collector for fast charging is shown. Furthermore, EFTEM imaging is used to visualize the Li-ion deintercalation process during charging.

1. Introduction

The higher gravimetric and volumetric energy density of lithium-ion batteries compared to other state-of-art rechargeable battery systems has contributed to the revolution of portable electronics over the past two decades. Lithium batteries are also being deployed in all-electric vehicles to help reduce greenhouse gas emissions. Energy and power density, recharging time and cycle life along with safety and cost are some of the major issues to be addressed in order to optimize and further improve the lithium batteries for transportation and energy storage applications [1,2]. These issues are in turn dependent on the choices of electrode and electrolyte materials. Research is being conducted throughout the world to find better alternatives to existing $LiCoO_2$ and graphite electrodes. $LiFePO_4$, $LiNi_{1/3}Mn_{1/3}Co_{1/3}O_2$, $LiNi_{0.5}Mn_{1.5}O_4$ and Si, to name a few, are already being used commercially and/or are being considered as new electrode materials. There are also a tremendous amount of research going on worldwide to design suitable electrode morphology of these materials to achieve near theoretical capacity at high (dis)charging rate [3–5].

To leverage the full potential of any electrode material, we must understand its (de)lithiation mechanisms in connection with particle size, grain–grain boundary, defects, doping, electrode degradation and the evolution of solid electrolyte interphase (SEI) [6,7]. To do so, the reaction kinetics and microstructural evolution must be examined during battery operation. TEM is the *in situ* technique of choice because it features the unique capability of resolving the microstructural evolution of electrode materials at high tempo-spatial resolution [8,9].

The main challenge performing *in situ* TEM battery experiments is the non-compatibility of organic electrolytes with high-vacuum conditions. Recent advance of TEM holders have made it possible to encapsulate thin liquid layers in a liquid cell platform to conduct battery cycling *in situ* [10,11]. However, this technique is still in its infancy, and problems with electrolyte degradation under electron-beam irradiation and the need for a very thin liquid layer to be sufficiently electron-transparent makes it difficult for researchers to conduct such experiments [10,11]. To overcome these difficulties, researchers mostly use an open-cell design to study electrode evolution during battery cycling [8,9]. For this, oxidized Li (Li_2O) is used as the electrolyte, which is stable in TEM vacuum. Figure 1 shows the schematic of such a design. However, owing to the inherent design of this system, Li-ions can only be inserted or extracted via the edge of the electrode that is connected to the Li_2O[8,9]. In other words,

this prevents Li-ions (de)insertion through every part of the electrode surface. Thus, the information obtained about electrode's (de)lithiation process can be incomplete. Moreover, the low ionic conductivity of the Li_2O introduces additional resistance in the battery, leading to high overpotential, and thus Li-ion (de)insertion kinetics may be different from the practical situation[12].
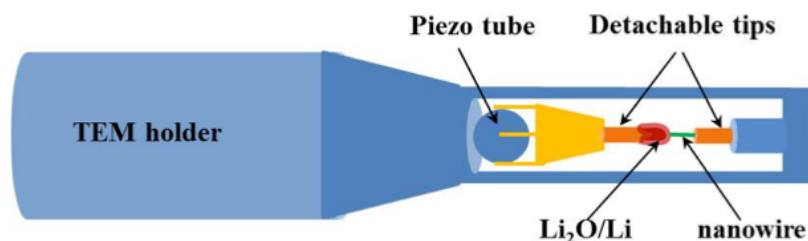

Figure 1: Schematic of STM-TEM holder with detachable tips, widely used for in-situ TEM battery experiments.

Using MEMS-based chips two broadly applicable open-cell designs are developed to solve the above issues by allowing Li-ions to (de)intercalate from every part of the electrodes using a practical solid-state electrolyte. Our 'nanowire battery setup' is suitable for nanowire-like electrodes. TEM lamellas prepared from bulk electrodes can also be studied (Figure 2). Our 'nanoparticle battery setup' is primarily suitable for smaller nanoparticles (Figure 4a).

$LiFePO_4$ is arguably one of the best cathodes for Li-ion batteries owing to its theoretical capacity of $170\ \mathrm{mAh\ g^{-1}}$, which is achievable especially at low current densities (low C rates) [13,14]. However, at higher current densities (high C rates), which are especially required for powering electrical vehicles, the achievable capacities are much lower than the theoretical ones [15]. Detailed knowledge of the (de)lithiation mechanism in $LiFePO_4$ may enable us to prepare the perfect nanoparticles for fast charging. Different models (core-shell, directional core-shell, domino-cascade and spinodal) have been proposed to explain the (de)lithiation mechanism [16–19]. Even though each model explains the (de)lithiation mechanism differently, every model suggest that Li-ion (de)intercalation inside $LiFePO_4$ occurs along b crystallographic direction. This led fabrication of platelets like nanostructures, with narrow b dimensions, as the best morphology to achieve fast kinetics. However, recently Li *et al.* found unexpectedly excellent electrochemical performance of 12-nm-thick $\langle 100 \rangle$-oriented $LiFePO_4$ nanoflakes compared to $\langle 010 \rangle$ platelets [20]. This prompted us to revisit the charge–discharge mechanism of the well-studied $LiFePO_4$, which is why we chose use $LiFePO_4$ to test our nanobattery setups.

2. Nanowire battery setup

Figure 2 illustrates the basic idea of our nanowire battery setup. MEMS chips are used as a platform to assemble the nanobattery. Electrical bias is applied to the electrode nanoparticle(s) via the gold pads—which also act as current collectors—and the thin solid electrolyte deposited on top of the chip, connects the two electrodes electrochemically. As the electrolyte covers the entire top surface of the electrodes, Li-ions can be (de)intercalated from any part of the electrode. Thus the (de)insertion of Li-ions actually depends on the inherent material properties of the electrode rather than on the experimental design. The small thickness of the electrolyte also allows us to perform accurate spectroscopic measurements of the electrodes during the (dis)charge process inside a TEM.
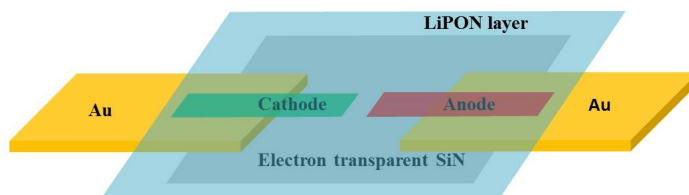
Figure 2: *Schematic shows the basic idea behind our in-situ TEM battery setup. MEMS-based TEM chip act as a platform for assembling the nanobattery with a single-particle cathode, anode and thin solid-state electrolyte.*

A single crystal of $LiFePO_4$ grown in an optical floating-zone furnace is used to test the nanowire battery setup, details synthesis procedure can be found in Ref.[21]. After conventional mechanical polishing, TEM samples (lamellas) are prepared using a dual beam (SEM-FIB) as shown in Figure 3a. The as-prepared lamella measuring ~15 µm × 5 µm × 100 nm is placed on to the gold pads of the MEMS chip using a glass needle. To ensure good electrical contact between the $LiFePO_4$ lamella and the gold pads, Pt is deposited using ion-beam-induced deposition (IBID) (Figure 3b).

Lithium phosphorus oxynitride (LiPON) is used as the electrolyte. It is the most commonly used solid electrolyte for thin-film Li-ion batteries because of its wide stability window (0–5 V vs. Li^+/Li) and reasonable ionic conductivity $(10^{-6}\,S\,cm^{-1})$[22,23]. A 30-nm-thick layer of LiPON is deposited on the chip by magnetron sputtering from a Li_3PO_4 target in a N_2 environment. The electrolyte coverage ensures that Li-ions can be (de)intercalated from every part of the lamella. Like most of the Li-ion battery electrolytes, LiPON is sensitive to moisture. Therefore, a custom-made vacuum transfer electrical TEM holder

(Chapter 2) is used for these experiments to avoid any air exposure to the electrolyte.

To delithiate $LiFePO_4$ ($LiFePO_4 \rightarrow Li^+ + e^- + FePO_4$) inside the TEM, a bias of 3.5 V is applied, shown schematically in the inset of Figure 3c. Owing to the applied bias, Li-ions travel from the lamella through the electrolyte and are deposited on the negatively biased gold. Thus, the negatively biased gold in this experiment acts as a pseudo-anode.

Li-ions (de)intercalating in and out of the electrode, thus filling and emptying the valence bands, changes the electronic structure. These changes can be recorded using Valence EELS (VEELS) with sub-nanometer resolution. Appearance of a peak at 5 eV for $FePO_4$, which is not present for $LiFePO_4$ distinguishes between the lithiation states of these VEELS is used to track the delithiation of $LiFePO_4$ during these experiments[24].
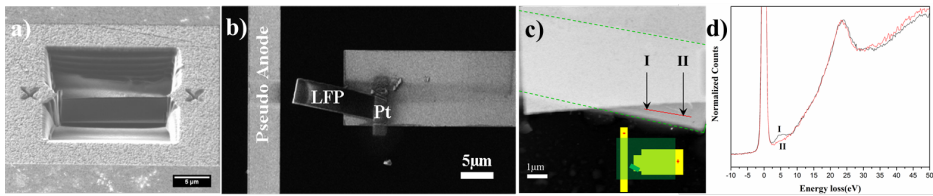
Figure 3: *(a) Prepared $LiFePO_4$ lamella using FIB. (b) The as-prepared lamella (LFP) is transferred to the MEMS chip using a micromanipulator [i]. Pt is deposited via IBID to ensure good electrical contact between the lamella and the gold pad. (c) STEM image of the lamella after initial charging. The green dotted line is added for easy visualization of the lamella. The inset schematic shows the configuration of the experiment. The yellow rectangles represent the gold pad. The green rectangle represents the TEM lamella and the LiPON is represented by semi-transparent green. The positive and negative signs represent the applied bias. The red line of the lamella indicates the location where EELS line scan is performed. (d) EELS spectra from positions I and II of the lamella. The peak in the EEL spectra for position I reveals the transformation of $LiFePO_4$ into $FePO_4$ at that position.*

Figure 3d shows the VEELS from positions I and II of the lamella (indicated in Figure 3c) after bias has been applied for 10 minutes. The occurrence of a peak at 5 eV for position I and the absence for position II, indicates that $LiFePO_4$ has transformed into $FePO_4$ at position I but not at position II. During charging of $LiFePO_4$, both Li-ions and electrons travel out of the lamella in opposite directions. As LiPON completely covers the top surface of the lamella, Li-ions have equal probability to deintercalate from the lamella from positions I and II.

---

[i] *The lamella is placed such that it lies very close to the pseudo-anode (gold pad) but is not in contact with it. The distance between the lamella and the vertical gold pad is typically about 1 μm.*

However, considering the intrinsically low electronic conductivity of LiFePO$_4$, electron transfer from position I is more favourable than from position II. Thus, the initiation point of delithiation is determined by the electronic conductivity of the sample. This also prompts the need for a better electrode–electrolyte–current collector connection.

In this experiment, owing to the low electronic conductivity of the sample, the LiFePO$_4$ lamella could only be delithiated from the area closest to the current collector. It should be noted that, owing to the lack of electrolyte coverage throughout the electrode, such an observation would not be possible in battery experiments conducted with the widely used STM-TEM holder. This result demonstrates the effectiveness of our nanowire battery setup.

3. Nanoparticle battery setup

Figure 4 illustrates the basic concept of our nanoparticle battery setup. Addition of an extra electron-transparent conductive layer connected to the gold pads allows (dis)charging of electrode nanoparticles along with *in situ* TEM measurements.
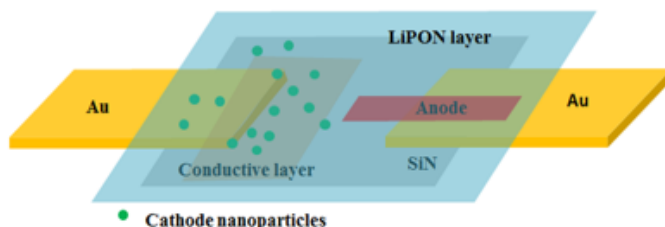
Figure 4: Schematic shows the basic idea behind of the nanoparticle battery setup.

For this setup, multilayers (3-5) of graphene flakes are first transferred to the gold pads on the TEM chips via the wedge transfer method, see Figure 5a. Next, the chip is heated to 300°C inside an argon glovebox to make good electrical contact between the graphene and the gold pads. The graphene flakes act as the extended current collector. When a suspension of electrode nanoparticles is drop-casted onto the MEMS chip, some of the nanoparticles are dispersed on the graphene flakes and become attached to the graphene as the solvent evaporates. One of the advantages of this setup compared to that of the nanowire battery is that no platinum need be deposited to make electrical contact between the electrode nanoparticles and the current collector. This also ensures the absence of a Pt halo, which is an excess of Pt around the intended

area deposited during IBID, making it easy to visualize the electrochemical (de)lithiation process of small nanoparticles [25].
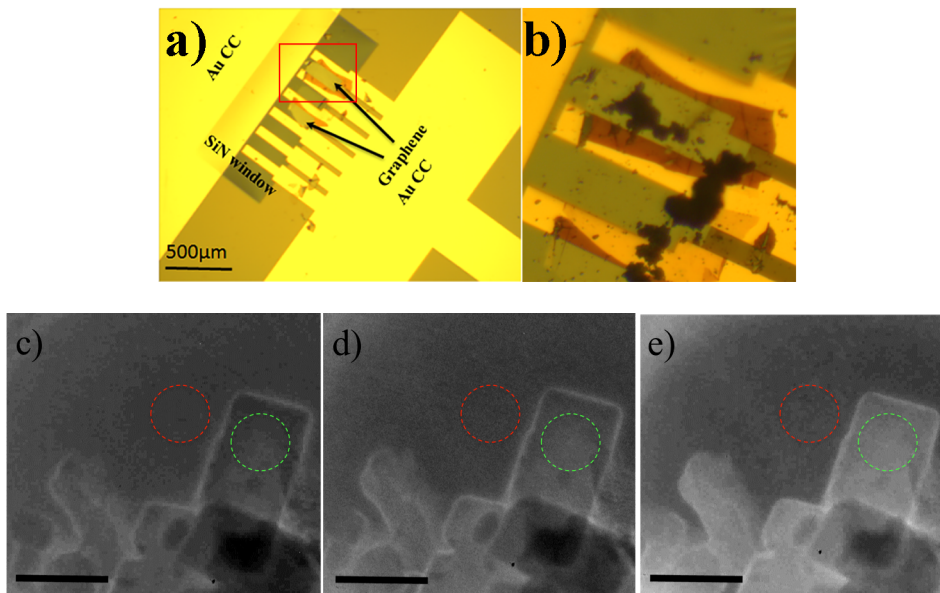
Figure 5: *(a) Optical image shows the graphene flakes on the electron transparent area of the chip. (b) Optical image shows the dispersed LiFePO₄ nanoflakes around the graphene after LiPON deposition. (c-e) EFTEM images of the LiFePO₄ nanoflakes during different stages of charging, acquired with a 5eV slit at 5 eV; (c) before applying bias, (d) after 5 minutes of charging and (e) after 10 of charging. The scale bar is 200 nm. The indicated area is used to measure the intensity variations on and off the LiFePO₄ particles during charging, listed in Table 1.*

As mentioned above, Li *et al.* recently reported the unexpectedly good performance of [100]-oriented carbon-coated LiFePO₄ nanoflakes [20]. This contradicts the general belief that LiFePO₄ platelets with narrow *b* dimension is the best morphology to achieve for fast kinetics of this battery system. Li *et al.* explained that such exceptional results originate from decreased $\Delta\mu_b$ associated with facilitating the single-phase transformation. Here [100]-oriented LiFePO₄ particles are used to gain insight into the (de)lithiation behaviour using our new *in situ* chips. Details about synthesizing the nanoflakes can be found in Ref [20]. A suspension of the as-prepared sample is created in ethanol and drop-cast onto the chip. Then, a 30-nm-thick layer of LiPON is deposited using magnetron sputtering, as done in the nanowire battery setup. Some of these nanoflakes appear as agglomerates on top of the graphene and are thus electrically connected to the gold pads, meaning that they can be charged, see

Figure 5b. Those nanoflakes, which are dispersed outside of graphene sheet, are not electrically connected to the gold electrodes and thus cannot be charged. In this case, the negatively biased gold electrodes also act as a pseudo-anode.

As can be seen in Figure 3d, a fingerprint peak occurs at 5 eV in the $FePO_4$ but is absent in the $LiFePO_4$, which helps us identify the lithiation state of $LiFePO_4$. Thus, using a slit at 5 eV of 5 eV width, EFTEM imaging can be used to visualize the (de)lithiation state of $LiFePO_4$[26]. Delithiated $LiFePO_4$ (Li_xFePO_4) will appear brighter than $LiFePO_4$ in the EFTEM images at 5 eV with a 5-eV slit. However, one must bear in mind that carbon also shows VEELS peak at 5 eV. Thus, the presence of carbon will also make the area brighter. Figures 5c–e are snapshots of $LiFePO_4$ nanoflakes acquired during charging. Before charging, at 0 minutes, the nanoflakes appear darker and the brighter edges presence the carbon. As charging progresses, the nanoflakes become brighter. Average intensities of the marked regions show the intensity variations on and off the $LiFePO_4$ particles, see Table 1. Increase intensity of the surrounding area of the particles over time can be attributed to the carbon contamination deposited during the experiment. Therefore, this experiment demonstrates the transformation of $LiFePO_4$ into $FePO_4$ during charging. Furthermore, it appears that these nanoflakes delithiated uniformly throughout the particle rather than following any particular crystallographic direction.

Charging time (minutes)	Average intensity of the surrounding area (Abr. unit)	Average intensity of the $LiFePO_4$ particle (Abr. unit)
0	56	62
5	58	78
10	69	116

Table 1: Average intensity of the areas marked in Figure 5, obtained using Imagej software.

4. Conclusion

In summary, two new designs are developed for *in situ* TEM battery experiments using MEMS chips, which act as the substrate for assembling the nanobattery. Deposition of the thin solid electrolyte (LiPON) allows Li-ions (de)intercalation from every part of nanoparticle surface. Thus, this design provides a true and complete understanding of the (de)intercalation mechanism of the electrode nanoparticles because it is configured such that the Li-ions can (de)intercalate depending on the intrinsic properties of the electrode rather than the experimental limitation.

Using these setups, we have demonstrated the importance of the interconnections between electrode, electrolyte and current collector. Furthermore, we have used EFTEM imaging to show how [100]-oriented LiFePO$_4$ nanoflakes delithiate in real time.

References

1.   Li H, Wang Z, Chen L, Huang X. Research on advanced materials for Li-ion batteries. *Adv Mater* (2009) **21**:4593–4607. doi:10.1002/adma.200901710

2.   Kiani MA, Mousavi MF, Rahmanifar MS. Synthesis of nano- and micro-particles of LiMn2O4: Electrochemical investigation and assessment as a cathode in li battery. *Int J Electrochem Sci* (2011) **6**:2581–2595. doi:10.1039/c1ee01598b

3.   Lin X, Salari M, Mohana L, Arava R, Ajayan PM, Grinstaff MW. High temperature electrical energy storage : advances, challenges, and frontiers. *Chem Soc Rev* (2016) **45**:Advance Article. doi:10.1039/C6CS00012F

4.   Ozanam F, Rosso M. Silicon as anode material for Li-ion batteries. *Mater Sci Eng B* (2016) **213**:2–11. doi:10.1016/j.mseb.2016.04.016

5.   Kim JH, Pieczonka NPW, Yang L. Challenges and approaches for high-voltage spinel lithium-ion batteries. *ChemPhysChem* (2014) **15**:1940–1954. doi:10.1002/cphc.201400052

6.   Gauthier M, Carney TJ, Grimaud A, Giordano L, Pour N, Chang H-H, Fenning DP, Lux SF, Paschos O, Bauer C, et al. The Electrode-Electrolyte Interface in Li-ion Batteries: Current Understanding and New Insights. *J Phys Chem Lett* (2015)acs.jpclett.5b01727. doi:10.1021/acs.jpclett.5b01727

7.   Verma P, Maire P, Novák P. A review of the features and analyses of the solid electrolyte interphase in Li-ion batteries. *Electrochim Acta* (2010) **55**:6332–6341. doi:10.1016/j.electacta.2010.05.072

8.   Liu XH, Liu Y, Kushima A, Zhang S, Zhu T, Li J, Huang JY. In situ TEM experiments of electrochemical lithiation and delithiation of individual nanostructures.*AdvEnergyMater*(2012)**2**:722–741.doi:10.1002/aenm.201200024

9.   Liu XH, Huang JY. In situ TEM electrochemistry of anode materials in lithium ion batteries. *Energy Environ Sci* (2011) **4**:3844. doi:10.1039/c1ee01918j

10.   Wu F, Yao N. Advances in sealed liquid cells for in-situ TEM electrochemial investigation of lithium-ion battery. *Nano Energy* (2015) **11**:196–210. doi:10.1016/j.nanoen.2014.11.004

11.   Wang C-M. In situ transmission electron microscopy and spectroscopy studies of rechargeable batteries under dynamic operating conditions: A retrospective and perspective view. *J Mater Res* (2015) **30**:326–339. doi:10.1557/jmr.2014.281

12.   Wakihara M, Yamamoto O eds. *Lithium ion batteries: fundamentals and performance*. Wiley-VCH (1998).

13.   Huang H, Yin S-C, Nazar LF. Approaching Theoretical Capacity of LiFePO at Room

Temperature at High Rates. *Electrochem Solid-State Lett* (2001) **4**:A170–A172. doi:10.1149/1.1396695

14. Yamada A, Chung SC, Hinokuma K. Optimized LiFePO4 for lithium battery cathodes. *J Electrochem Soc* (2001) **148**:A224–A229. doi:10.1149/1.1348257

15. Yuan L-X, Wang Z-H, Zhang W-X, Hu X-L, Chen J-T, Huang Y-H, Goodenough JB. Development and challenges of LiFePO $_4$ cathode material for lithium-ion batteries. *Energy Environ Sci* (2011) **4**:269–284. doi:10.1039/C0EE00029A

16. Andersson AS, Kalska B, Haggstrom L, Thomas JO. Lithium extraction/insertion in LiFePO4: An X-ray diffraction and Mössbauer spectroscopy study. *Solid State Ionics* (2000) **130**:41–52. doi:10.1016/S0167-2738(00)00311-8

17. Laffont L, Delacourt C, Gibot P, Wu MY, Kooyman P, Masquelier C, Tarascon JM. Study of the LiFePO4/FePO4 Two-Phase System by High-Resolution Electron Energy Loss Spectroscopy. *Chem Mater* (2006) **18**:5520–5529. doi:10.1021/cm0617182

18. Burch D, Bazant MZ. Size-dependent spinodal and miscibility gaps for intercalation in nanoparticles. *Nano Lett* (2009) **9**:3795–3800. doi:10.1021/nl9019787

19. Delmas C, Maccario M, Croguennec L, Le Cras F, Weill F. Lithium deintercalation in LiFePO4 nanoparticles via a domino-cascade model. *Nat Mater* (2008) **7**:665–71. doi:10.1038/nmat2230

20. Li Z, Peng Z, Zhang H, Hu T, Hu M, Zhu K, Wang X. [100]-Oriented LiFePO4 Nanoflakes toward High Rate Li-Ion Battery Cathode. *Nano Lett* (2016) **16**:795–799. doi:10.1021/acs.nanolett.5b04855

21. Chen DP, Maljuk A, Lin CT. Floating zone growth of lithium iron (II) phosphate single crystals. *J Cryst Growth* (2005) **284**:86–90. doi:10.1016/j.jcrysgro.2005.06.024

22. Choi CH, Cho WI, Cho BW, Kim HS, Yoon YS, Tak YS. Radio-Frequency Magnetron Sputtering Power Effect on the Ionic Conductivities of Lipon Films. *Electrochem Solid-State Lett* (2002) **5**:A14. doi:10.1149/1.1420926

23. Kovalenko L, V O, Belous A. Effect of Deposition Conditions On Microstructure of LiPON Films Obtained by RF Magnetron Sputtering. (2014)126–130.

24. Kaiser MKK and PA and MW-M and PM and FB and U. Origin of valence and core excitations in LiFePO 4 and FePO 4. *J Phys Condens Matter* (2010) **22**:275501. doi:10.1088/0953-8984/22/27/275501

25. Da Silva MM, Vaz a. R, Moshkalev S a., Swart JW. Electrical Characterization of Platinum Thin Films Deposited by Focused Ion Beam. *ECS Trans* (2007) **9**:235–241. doi:10.1149/1.2766894

26. Holtz ME, Yu Y, Gunceler D, Gao J, Sundararaman R, Schwarz KA, Arias TA, Abruña HD, Muller DA. Nanoscale imaging of lithium ion distribution during in situ operation of battery electrode and electrolyte. *Nano Lett* (2014) **14**:1453–1459. doi:10.1021/nl404577c

CHAPTER 9

FUTURE WORK

The knowledge acquired during the experiments described in previous chapters, formulates the pathway for the future studies. In this concluding chapter the future experiments are briefly discussed. This includes in-situ TEM holography using thin film battery; use of nanoreactor to study the role of SEI layer in Si anode performance, the initial stages of Li_2O_2 formation and dissolution; optimizing TEM parameters to study Ni-O_2 discharge products.

1. Observation of charge distribution evolution in Solid-State battery

The dynamics of local charge distribution governs the ion insertion/extraction process and ultimately determines the battery performance. Detailed knowledge of this dynamics will help in better understanding of the electrochemical processes in a battery and thus will contribute in building better batteries for the future. In-situ TEM holography offers the opportunity to directly visualize the charge distribution up to sub-nanometer resolution[1–3]. Thus it can be utilized in visualizing dynamics of charge distribution across electrode as well as electrode-electrolyte interface during (dis)charge of a battery[4].

A solid-state thin film is battery prepared using PLD and magnetron sputtering. The deposition parameters are optimized to prepare electrodes and electrolyte with correct stoichiometry and crystal structure. First, 200 nm thick $LiCoO_2$ is deposited as cathode on top of platinum foil, acting as current collector, using PLD at 600°C [i]. Since high temperature deposition led to lower lithium concentration, compare to the target composition, an extra 10 wt.% Li_2O is added during the target preparation to compensate for the lithium loss. Following $LiCoO_2$ deposition 1 μm thick LiPON is deposited using RF magnetron sputtering, as electrolyte, from a LiP_3O_4 target (Goodfellow) with 100W power in a base pressure of 10^{-9} mbar in N_2 atmosphere.

Before LiPON deposition, the surface of $LiCoO_2$ is etched slightly (2-5nm) using argon plasma to remove the possible Li_2CO_3 formed on $LiCoO_2$ surface due to air exposure [5]. Directly after the LiPON deposition, a 200nm thick film of Si as anode and 1.5 μm thick Cu film as current collector are deposited inside the same sputtering chamber in argon atmosphere.

Cross-sectional FIB lamellas are prepared from the thin film battery and are transferred to a MEMS micro heater chips with Pt electrodes for biasing. Fabrication of these MEMS chips, Fig. 1(a), is described in Chapter 6. Figure 1(b) shows SEM image of typical lamella transferred and connected to the Pt electrodes using IBID-Pt. Further cuts are made in the lamellas to prevent short circuit during biasing. The basic idea behind incorporating the possibility to heat the nanobattery is threefold. Firstly, heating to a moderate temperature (80-120°C) will allow replicating the condition battery material faces during the thermal runaway. Thus we can learn insides of battery process during thermal runaway. Secondly, most of the solid electrolytes used in thin film battery have

---

[i] *PLD deposition is done by Dr. D.P.Singh at University of Twente, Netherlands.*

1. Observation of charge distribution evolution in Solid-State battery
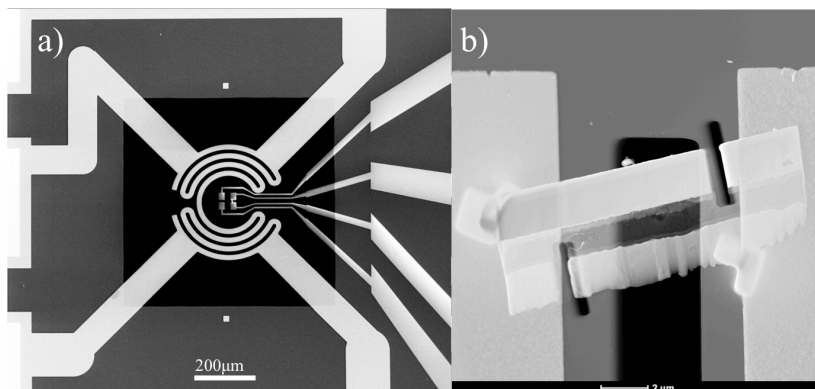
Figure 1: *(a) SEM image shows the MEMS heating chip with the circular heating coils and electrical contacts. (b) HAADF-STEM image shows the connection of the FIB lamella.*
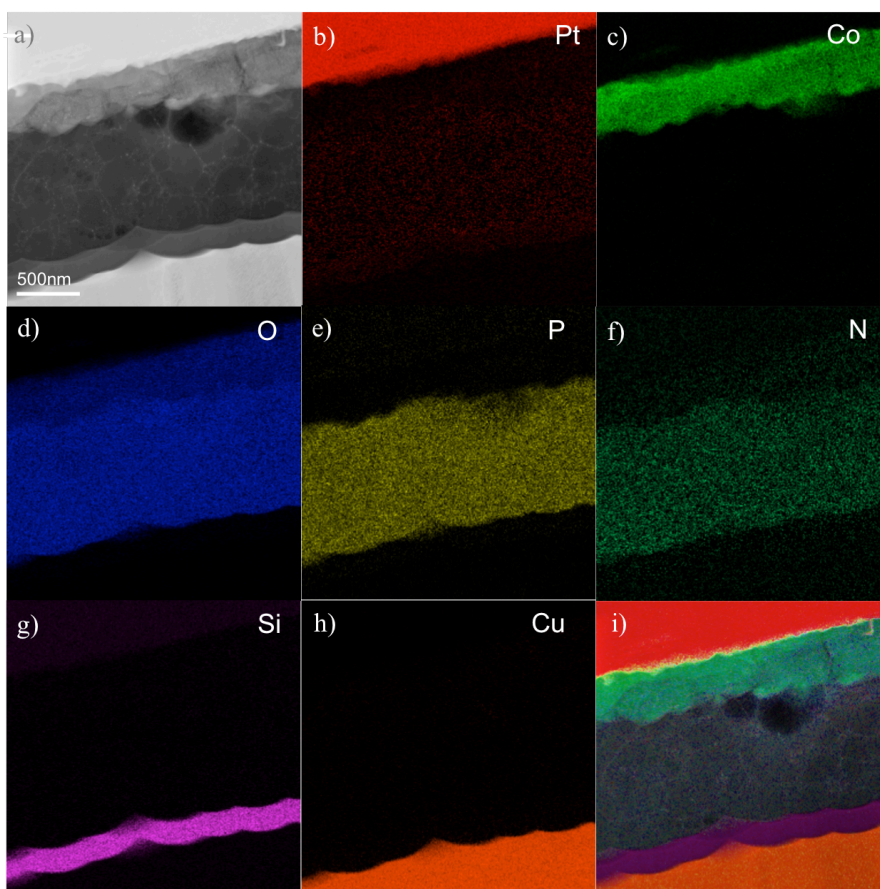
Figure 2: *(a) HAADF-STEM image of the lamella. (b-f) elemental map showing distribution of (b)Pt, (c) Co, (d) O, (e) P, (f) N, (g) Si, (h) Cu and (i) overlay.*

low ionic conductivity, which improves by a factor or two at higher temperature[6,7]. Allowing battery cycling at different temperatures we will be

able switch between electrically limited to ionically limited (dis)charge regime. Thirdly, at a temperature above 100°C, carbon contamination reduces drastically, allowing reliable TEM analysis.

The STEM image in Figure 2a shows a typical cross sectional sample (lamella) prepared using FIB operating at 30kV from the thin film battery. Figures 2b-2i show the EDS mapping of the lamella. The estimated phosphorous, oxygen and nitrogen atomic percentage are 22, 70 and 8 % respectively in LiPON. The problem of Pt re-deposition, as can be seen in Figure 2b, can be overcome by adding an extra thinning step at the end of lamella preparation with lower current, acceleration voltage [8]. *In situ* charge distribution dynamics can be studied using these lamellas.

2. Liquid cell in-situ TEM battery

In Chapter 6, fabrications of nanoreactor chips are described. The uses of the nanoreactors allow introducing liquid electrolytes inside high vacuum TEM environment. The nanoreactors are well suited for the following studies.

2.1. Understanding the role of SEI layer on battery performance

The SEI layer is typically formed at the negative electrode during charging of a battery. Even though the SEI layer formation leads to capacity fading in the initial battery cycles, the SEI layer also protects the electrode from direct contact to the electrolyte and thus protect against further solvent decomposition [9,10]. The behavior of SEI layer becomes even more important in terms of battery performance for alloy anode materials, which are subjects to drastic volume changes during the battery cycles. Even after lots of research the formation and evolution of the SEI layer is considered as a "grey area" of the battery research[10]. The use of nanoreactor will help direct monitoring of the formation and growth of SEI layer during battery cycles inside TEM, which will lead to in depth understanding of SEI formation mechanism.

2.2. Visualizing the formation and dissolution of Li$_2$O$_2$

Long term cycling issue is hampering the tremendous potential of Li-O$_2$ battery. To overcome this formation and decomposition mechanisms of the discharge product, especially at the early stages, have to be understood in details. The nanoreactors facilitate visualization of the formation and dissolution of Li$_2$O$_2$ at the early stages.

3. Revealing mechanism of Na-O$_2$ battery

Global lithium resource is estimated as 30–40 metric tons, which may prove to be insufficient to meet future demands of energy storage, especially considering a lithium-recycling rate (less than 1%) [11]. On the other hand, sodium (Na) is one of the most abundant elements in the earth's crust ($\approx$2.6%) and available in virtually unlimited amounts in seawater. Due to this reason Na-O$_2$ battery started to receive renewed interest.

Initial results from the Na-O$_2$ battery demonstrate lower discharge-charge overpotential compare to Li-O$_2$ battery [12-14]. The detailed mechanisms of discharge and charge steps and the reaction products formed during cycling are still under debate; NaO$_2$, Na$_2$O$_2$, and Na$_2$O$_2$-H$_2$O as the discharge product has shown in different studies, but further research are required to understand parameters influencing the nature of the discharge product [15,16]. TEM can be extensively used to understand the detailed chemical and structure of the Na-O$_2$ battery discharge product in relation with the used current density and electrolytes to unveil the underneath chemistry of the Na-O$_2$ battery.

Similar to Li-O$_2$ battery, the discharge product is air sensitive and presumably electron beam sensitive. Thus first a protocol has to be made for stopping any degradation of the sample till and during the TEM study. Following the pathway of Li-O$_2$ study as discussed in Chapter 4, the sufficient and necessary condition for TEM characterization of the discharge products can be devised.

To understand how Na-O$_2$ battery discharge products are distributed on the surface of cathode, and how the cathode components (including catalysts) can affect the morphology and composition of the reaction products, transfer of area specific information to the TEM is absolutely necessary. In Chapter 5, we have shown that use of standard holey carbon TEM grids on the Li-O$_2$ battery cathode support propose an easy way to keep the direct correlation between the cathode area and the formed discharge product for TEM study. This novel procedure to perform TEM investigation can be extended to study the reaction products of the Na-O$_2$ battery. Further, inserting sodium metal into the groove of the nanoreactor chip (Chapter 6), formation and growth of NiO$_2$ and Na$_2$O$_2$ can also be studied in an operando manner.

These TEM studies will help revealing the relation between morphology, structure, chemical composition of the Na-O$_2$ discharge product and current density, electrolyte, cathode support material (including catalyst), creating a better understanding on this challenging battery system.

References

1.   Yao Y, Li C, Huo Z, Liu M, Zhu C, Gu C, Duan X, Wang Y, Gu L, Yu R. In situ electron holography study of charge distribution in high-κ charge-trapping memory. *Nat Comm* (2013) **4**:2764. doi:10.1038/ncomms3764

2.   Tavabi AH, Arai S, Muto S, Tanji T, Dunin-Borkowski RE. In situ transmission electron microscopy of ionic conductivity and reaction mechanisms in ultrathin solid oxide fuel cells. *Microsc Microanal* (2014) **20**:1817–25. doi:10.1017/S143192761401349X

3.   Börrnert F, Riedel T, Müller H, Linck M, Büchner B, Lichte H. A Dedicated In-situ Off-axis Electron Holography (S)TEM: Concept and Electron-Optical Performance. *Microsc Microanal* (2014) **20**:1650–1651. doi:10.1017/S1431927614009982

4.   Yamamoto K., Iriyama Y., Hirayama T. Visualization of electrochemical reactions in all-solid-state li-ion batteries by spatially resolved electron energy-loss spectroscopy and electronholography. *Mater Trans* (2015) **56**:617–624. doi:10.2320/matertrans.M2015014

5.   Kovalenko L., V'yunov O., Belous A., Transactions ECS, Society TE. Effect of CO2 on Layered Li. (2008) **11**:7–13.

6.   Kovalenko L, V O, Belous A. Effect of Deposition Conditions On Microstructure of LiPON Films Obtained by RF Magnetron Sputtering. (2014)126–130.

7.   Choi CH, Cho WI, Cho BW, Kim HS, Yoon YS, Tak YS. Radio-Frequency Magnetron Sputtering Power Effect on the Ionic Conductivities of Lipon Films. *Electrochem Solid-State Lett* (2002) **5**:A14. doi:10.1149/1.1420926

8.   Schaffer M, Schaffer B, Ramasse Q. Sample preparation for atomic-resolution STEM at low voltages by FIB. *Ultramicroscopy* (2012) **114**:62–71. doi:10.1016/j.ultramic.2012.01.005

9.   Pinson MB, Bazant MZ. Theory of SEI Formation in Rechargeable Batteries: Capacity Fade, Accelerated Aging and Lifetime Prediction. *J Electrochem Soc* (2013) **160**:A243–A250. doi:10.1149/2.044302jes

10.   Goriparti S, Miele E, De Angelis F, Di Fabrizio E, Proietti Zaccaria R, Capiglia C. Review on recent progress of nanostructured anode materials for Li-ion batteries. *J Power Sources* (2014) **257**:421–443. doi:10.1016/j.jpowsour.2013.11.103

11.   Vikström H, Davidsson S, Höök M. Lithium availability and future production outlooks. *Appl Energy* (2013) **110**:252–266. doi:10.1016/j.apenergy.2013.04.005

12.   Hartmann, P.; Bender, C. L.; Vračar, M.; Dürr, A. K.; Garsuch, A.; Janek, J.; Adelhelm, P. A Rechargeable Room-Temperature Sodium Superoxide (NaO_2) Battery. *Nat. Mater.* **2013**, *12* (3), 228–232. doi:10.1038/nmat3486

13.   Xia, C.; Black, R.; Fernandes, R.; Adams, B.; Nazar, L. F. The Critical Role of Phase-Transfer Catalysis in Aprotic Sodium Oxygen Batteries. *Nat. Chem.* **2015**, *7* (6), 496–501. doi:10.1038/nchem.2260

14.   McCloskey, B. D.; Garcia, J. M.; Luntz, A. C. Chemical and Electrochemical Differences in Nonaqueous $Li–O_2$ and $Na–O_2$ Batteries. *J. Phys. Chem. Lett.* **2014**, *5* (7), 1230–1235. doi: 10.1021/jz500494s

15. Bender, C. L.; Schröder, D.; Pinedo, R.; Adelhelm, P.; Janek, J. One- or Two-Electron Transfer? The Ambiguous Nature of the Discharge Products in Sodium-Oxygen Batteries. *Angew. Chemie Int. Ed.* **2016**, *55* (15), 4640–4649. doi: 10.1002/anie.201510856

16. Pinedo, R.; Weber, D. A.; Bergner, B.; Schröder, D.; Adelhelm, P.; Janek, J. Insights into the Chemical Nature and Formation Mechanisms of Discharge Products in Na–O2 Batteries by Means of Operando X-Ray Diffraction. *J. Phys. Chem. C* **2016**, *120* (16), 8472–8481. doi: 10.1021/acs.jpcc.6b00903

Summary

With the focus in automobile industry to switch from petroleum-based vehicles to all electric vehicles, the increasing demand on harvesting energy from renewable sources for a safer and greener future and the ever-increasing demand of the portable electronics systems, the need for better batteries is eminent. The ultimate aim of battery research is to develop a low cost, light and small battery that can deliver high-capacity and/or high power. Lithium and sodium batteries are the frontrunners in achieving this ultimate battery.

A macro battery is composed of thousands of millions of nanoparticles. Thus, to prepare a better battery we must determine the respective effects of electrode nanoparticle size, shape, structure, grain–grain boundary, defects and doping on the battery performance. To do so electrode nanoparticles need to be probed at the nano-scale to find out the correlation between their morphology, structure and chemical properties and their evolution due to the battery charging-discharging with battery performance. In this thesis we have utilized the unique capability of electron microscope to resolve the microstructural and chemical information at the (sub)nanometer scale to probe the electrode nanoparticles for making better batteries.

In this thesis first noble electrode, electrolyte fabrication strategies to improve Li-ion, Na-ion, Li-S and Li-O_2 battery performance are explored. Scanning electron microscopy (SEM) and transmission electron microscopy (TEM) studies are utilized to identify the key factors that determine battery performance (Chapter 3).

Especially for Li-O_2 battery TEM analysis is hindered by the degradation of the samples upon air exposure and electron-beam irradiation. Therefore, preservation of the native details of the discharge products at nanometer scale during the sample preparation pose challenges for reliable TEM analysis. In Chapter 4, electron beam conditions are evaluated to reduce electron-beam degradation and methods to deal with air sensitivity are presented. Sample's air sensitivity can be addressed by using a vacuum transfer TEM holder. While the electron-beam degradation can be delayed by the use of low electron beam dose rate at moderate acceleration voltage, as discharge product (Li_2O_2) is found to degrade 4–5 times faster at 80 kV compared to 200 kV and the decomposition is completely dose-dependent. Further it is demonstrate that a "graphene cell", which encapsulates the sample between graphene sheets, can protect Li_2O_2 against damage due to air and e-beam exposure. In Chapter 5, the use of conventional holey carbon TEM grids in a Li-O_2 battery to unveil complex mechanisms of Li-O_2 battery by preserving the native environment of the discharges is presented.

The second half of the thesis demonstrates the role of *in situ* TEM studies in preparing better batteries, utilizing the unique capability of TEM to resolve the microstructural and chemical evolution at high tempo-spatial resolution. MEMS chips are the heart of our *in situ* TEM battery experiments. In Chapter 6, fabrication insights of different chips are discussed. Chips with electrical biasing, heating, biasing and heating capability are fabricated.

In Chapter 7, the role of *in situ* TEM in improving thin film battery is shown. *In situ* heating is utilized to unveil the crystallization process of thin film $LiFePO_4$ and effect of high current densities in Ni current collector is studied.

In situ TEM has already contributed a great deal especially to the Li-ion battery technology. However, the existing open-cell design that uses oxidized lithium as the electrolyte does not allow Li-ions to be (de)inserted from every part of the nanoparticle, which restricts (de)intercalation. This may lead to incomplete information about the (de)lithiation mechanism of the electrode material under investigation. To overcome this we have designed widely applicable open-cell MEMS-based chips and a thin layer of LiPON as the electrolyte to enable Li-ion (de)intercalation from every part of the electrode. Using $LiFePO_4$ electrodes in these setups, we have shown the importance of overlap between electrode, electrolyte and current collector for fast charging. Furthermore, we use EFTEM imaging to visualize the Li-ion deintercalation process during charging (Chapter 8).

In Chapter 9, the role of "nanoreactor" setup in performing *in situ* TEM battery experiments with liquid electrolytes and role of heating-biasing chips in performing battery operation at elevated temperature are discussed.

Samenvatting

Met het doel van de autoindustrie om over te gaan van voertuigen met een verbrandingsmotor naar geheel elektrisch aangedreven voertuigen, de groeiende vraag om energie op te wekken uit duurzame bronnen voor een veiligere en groenere toekomst en de altijd groeiende vraag naar draagbare elektronische apparaten is de noodzaak om beter batterijen te maken overduidelijk. Het uiteindelijke doel van batterijenonderzoek is het ontwikkelen van een goedkope, lichte en kleine batterij, die een hoge capaciteit en/of een hoog vermogen kan leveren. Lithium- en natriumbatterijen zijn de belangrijkste kandidaten voor zo'n optimale battterij.

Een macro-batterij bestaat uit duizenden of miljoenen nanodeeltjes. Dus, om een betere batterij te maken, moeten we bepalen wat voor effect de grootte, vorm, structuur, korrelgrootte, defecten en doping van de nanodeeltjes in de elektroden hebben op de prestaties van de batterij. Om dit te doen is het noodzakelijk om de nanodeeltjes van de elektroden te bekijken op nanoschaal om de correlatie te vinden tussen de prestaties van de batterij en hun morfologie, structuur en chemische eigenschappen en hun verandering ten gevolge van (ont)lading van de batterij. In dit proefschrift wordt de unieke kracht van de elektronenmicroscoop gebruikt om de microstructuur en chemische samenstelling van de nanodeeltjes in de elektroden op nanoschaal vast te stellen, teneinde te komen tot betere batterijen.

In dit proefschrift worden eerst edelmetalen elektrode-, elektroliet-fabricagestrategieen om Li-ionen-, Na-ionen-, Li-S- en Li-O$_2$ batterijen te verbeteren onderzocht met betrekking tot hun prestaties. Onderzoek met Scanning-ElectronenMicroscopie (SEM) en Transmissie-ElelektronenMicroscopie (TEM) is uitgevoerd om de belangrijkste factoren te bepalen voor de prestaties van de batterijen (hoofdstuk 3).

In het bijzonder voor Li-O$_2$ batterijen wordt de TEM analyse bemoeilijkt door de degeneratie van de monsters door blootstelling aan lucht en bestraling met de elektronenbundel. Daarom is het behoud van de originele details van de ontladingsproducten op een nanometer-schaal bij de monsterbereiding de grote uitdaging voor betrouwbare TEM-analyse. In hoofdstuk 4 worden de instellingen van de elektronenbundel geëvalueerd die degeneratie onder de elektronenbundel reduceren. Voorts worden er methoden aangedragen om het effect van luchtgevoeligheid te minimaliseren. Gevolgen van luchtgevoeligheid van de monsters kan verholpen worden door gebruik te maken van een vaccuum-tranferhouder voor de TEM. De degeneratie ten gevolge van de elektronenbundel

kan vertraagd worden door gebruik te maken van een elektronenbundel met een lage dosessnelheid en met een lage versnelspanning. Voor het ontladingsproduct (Li_2O_2) is gevonden dat het 4 tot 5 keer sneller degradeerd bij 80kV dan bij 200kV en de ontbinding is geheel dosis afhankelijk. Voorts is aangetoond dat een "grafeencel", die het monster opsluit tussen twee grafeenlagen, Li_2O_2 kan beschermen tegen schade door blootstelling aan lucht en door bestraling met de elektronenbundel. In hoofdstuk 5 wordt het gebruik van conventionele koolstof TEMgrids met gaten voor een Li-O_2 batterij gepresenteerd om complexe mechanismen van de Li-O_2 batterij te ontrafelen terwijl de originele omgeving van de ontladers behouden blijft.

De tweede helft van het proefschrift beschrijft de rol van *in situ* TEM studies om betere batterijen te maken, gebruik makend van de unieke eigenschap van TEM om de microstructurele en chemische veranderingen met een hoog tijds- en ruimtelijk-oplossendvermogen te kunnen bepalen. MEMS-chips zijn het hart van onze *in situ* TEM-experimenten aan batterijen. In hoofdstuk 6 worden de details van de fabricage van verschillende chips besproken. Chips met elektrische voorspanning-, verwarmings- en voorspanning samen met verwarmings-mogelijkheden werden gefabriceerd.

In hoofdstuk 7 wordt de rol van *in situ* TEM om batterijen bestaande uit dunne film te verbeteren beschreven. *In situ* verwarming wordt gebruikt om het kristallisatie proces van een dunne $LiFePO_4$ film te ontrafelen. Tevens werd het effect van hoge stroomdichtheden in Ni stroom-collectoren bestudeerd.

In situ TEM heeft al een grote bijdrage geleverd met name aan de Li-ionen-batterijtechniek. Echter, het open-celontwerp, dat gebruik maakt van geoxideerd lithium als elektroliet, staat niet toe dat Li-ionen (in/uit)gevoegd worden in elk deel van het nano-deeltje, hetgeen de (de)intercalatie beperkt. Dit kan leiden tot incomplete informatie over het (de)lithificatiemechanisme van het elektrodemateriaal dat onderzocht wordt. Als oplossing voor dit probleem hebben we een algemeen toepasbare open-cel-chip ontworpen gebaseerd op MEMS-technieken en gebruiken we een dunne laag LiPON als elektroliet om het mogelijk te maken dat de Li-ionen-(de)intercalatie kan plaatsvinden in alle delen van de elektrode. Daarbij gebruik makend van $LiFePO_4$ elektroden, hebben we het belang aangetoond van de overlap tussen de elektroden, elektroliet en stroomcollector voor het snel opladen van de batterij. Verder hebben we EFTEM gebruikt om de Li-ionen-deintercalatie te visualiseren (hoofdstuk 8).

In hoofdstuk 9 wordt de rol besproken van het "nanoreactor" ontwerp ten aanzien van het uitvoeren van *in situ* TEM-batterijexperimenten met vloeibare elektrolieten

en de rol van verwarmingschips met voorspanning in de prestatie van de batterij op verhoogde temperatuur.

Curriculum Vitae

Shibabrata BASAK

19-09-1984	Born in Kolkata, India
2002 – 2005	Bachelor of Science in Physics University of Calcutta, India
2005 – 2007	Master of Science in Physics Sikkim Manipal University, India *Thesis:* "Fabrication of Optical Fibre Sensors" *Promotor:* Dr. Rajesh Kumar
2008 – 2010	Master of Technology in Solid State Technology Indian Institute of Technology Kharagpur, India *Thesis:* "ZnO Nanostructures: Optoelectronics, Biophotonic and sensor Applications" *Promotor:* Dr. Partha Roy Chaudhuri
2010 – 2011	Assistance Professor Haldia Institute of Technology, India
2011 – 2016	Ph.D. in Applied Physics Delft University of Technology, the Netherlands *Thesis:* "Making Better Batteries: Following Electrochemistry at the Nano Scale with Electron Microscopy" *Promotor:* Prof. Henny W. Zandbergen
2017 – Present	Application Scientist DENS Solutions Delft, the Netherlands

Publications

(Relevant to the thesis)

1. **S. Basak**, Y. Kabiri, J. Jansen, H. W. Zandbergen, *Optimization of experimental parameters for reliable TEM investigation of Li-O$_2$ battery*, to be submitted.
2. **S. Basak**, S. Bajaj, S. Ganapathy, M. Wagemaker, H. W. Zandbergen, *Unveiling Mechanisms Of Li-O$_2$ Batteries Using TEM Grids*, to be submitted.
3. **S. Basak**, S. R. K. Malladi, S. Ganapathy, Z. Li, M. Wagemaker, X. Wang, H. W. Zandbergen, *Designing reliable in situ TEM battery experiments with thin LiPON and graphene*, to be submitted.
4. **S. Basak**, H. Schreuders, B. Dam, H. W. Zandbergen, *In situ* TEM observation of LiFePO$_4$ crystallization process, in preparation.
5. T. Kozlova, **S. Basak**, S. R. K. Malladi, H. W. Zandbergen, *In situ* TEM observation of electromigration in Ni nanobridges, to be submitted.
6. S. Ganapathy, **S. Basak**, A. Lefering, E. Rogers, H. W. Zandbergen, M. Wagemaker, *Improving Reversible Capacities of High-Surface Lithium Insertion Materials—The Case of Amorphous TiO$_2$*, Frontiers in Energy Research, 2, 1-8 (2014).
7. Y. Xu, E. Swaans, **S. Basak**, H. W. Zandbergen, D. Borsa, F. Mulder, *Reversible Na-ion uptake in Si nanoparticles,* Adv. Energy Mater. 2016, 6, 1501436.
8. D.P. Singh, N. Soin, S. Sharma, **S. Basak**, S. Sachdeva, P. Gonugunta, S.S. Roy, H.W. Zandbergen, J.A. McLaughlin, M. Huijben, M. Wagemaker, 3-D Vertically Aligned Few Layer Graphene – Partially Reduced Graphene Oxide/Sulfur Electrodes for High Performance Li-Sulfur Batteries, Advanced Materials Interfaces (Submitted).
9. Y. Xu, E. Swaans, S. Chen, **S. Basak**, P. P. R. M. L. Harks, B. Peng, D. Borsa, H. W. Zandbergen, F. M. Mulder, *A High-performance Li-ion Anode from Direct Deposition of Si Nanoparticles,* Nano Energy (Submitted).
10. C. Yu, S. Ganapathy, E. R. H. Eck, **S. Basak**, H. W. Zandbergen, M. Wagemaker, Revealing the annealing effects on Li-ion mobility in Li$_6$PS$_5$Br solid electrolyte synthesized by mechanical milling route, in preparation.

Acknowledgements

In the final pages of this thesis I would like to express my gratitude to the people who contributed through out my PhD journey. Without them this book wouldn't be completed.

First of all, I am grateful to Prof. dr. Henny Zandbergen for giving me this wonderful opportunity to pursue my PhD in field of *in situ* TEM. I can never forget the warm welcome when I first came to Delft. He has been the best promotor that I can imagine, allowing me to explore all my research ideas, guiding me through my research and standing beside me in my tough times, both personal and research wise. His enthusiasm in doing any experiment is unparalleled to any. Hopefully, I can retain the inspiration and enthusiasm he conferred in me. Thank you Henny for your support, it has been a great experience!

Next, I want to thank Dr. ir. Frans Tichelaar, my daily supervisor. He not only taught me how to use TEM, explaining step by step how things are working from the first session in CM30T, but also helped me when I got "stuck" during the project with numerous discussions.

During my PhD I had an opportunity to be a visiting scholar in the group of Prof. Paul Alivisatos at University of California Berkeley. I would like to thank him for giving me this opportunity and the informative discussions on my research and advice. I would like to thank all of his the group members of for making the visit enjoyable. My special thanks goes to Xingchen for showing me synthesis of Au NPs and the late night TEM sessions, Qian for teaching me how to prepare graphene liquid cell, Son, Karthis, for numerous discussions. I really enjoyed working with you. I like to thank Toshi for joining me on trips around US.

In situ TEM battery project is truly interdisciplinary subject and thus requires lots of collaboration. I like to thank all the group members of Dr. Marnix Wagemaker, Prof. Fokko Mulder and Prof. Bernard Dam for their help in sample preparation and newer insights into the vast area of electrochemistry, especially to Herman, for all those long depositions, Zhaolong, Yaolin, Peter-Paul, Chuang (Yu), Violetta and Deepak. Special thanks to Swapna, who was also the postdoc in the project, for spending so much time in this project, I hope someday in near future we will have the perfect battery sample for *in situ* TEM experiment.

Big part of my PhD project is devoted to the fabrication of MEMS chips. Fabrication of these chips wouldn't be possible without the help from Charles, Marco, Mark, Ewan, Gregory, Roel, Anja and Arnold. All those scientific and

casual discussion made clean room working enjoyable. A big thank to Hozanna, for her spontaneous support whenever I encountered any issue with TEM sample preparation using FIB.

Great thanks to Raymond and Ruud for building the electrical measurements setup for the *in situ* experiment. I would also like to acknowledge the people from DEMO, especially Eef, Danny, Leon who helped solving any problem with the TEM holders whenever needed.

I want to thank all my colleagues from our HREM group for all the help during my PhD. During my PhD I have tried numerous research ideas. That also meant I needed numerous type of custom made devices and programs. These experiments wouldn't be possible without the help from Tom and Jouk. Tom, thank you so much for preparing all those devices in fast possible pace and Jouk, thank you for all the custom made programs that you have prepared for me and also for the Dutch translations of the thesis summary and propositions. I would also like to acknowledge the help from Ulrike and Vasili. Thanks a lot to Marijke for your help in taking care of all the legal procedures and your efficiency in arranging meetings, appointments. I want to thank all the previous and current Postdocs, PhDs and Bachelor students Marijn, Meng-Yue, Qiang, Maria, Bo, Ganesh, Sairam, Anil, Tatiana, Chao, Dieter, Masha, Chenggang, Leo, Jelle, Ahmet, Yoones, Majid and Zahra. Thank you for being such nice colleagues, I am very lucky to work with you. Special thanks to my bachelor students, Felix and Siemen, who had devoted long hours working with me.

Tatiana, I am glad that we have started PhD on same day and became good friends. You are a very positive person - always have a nice solution for every problem. I cannot thank you enough for our lunches, BBQ, movies, Prague trip and those long chats. Hugo, thanks a lot my friend for all your help with the nanorobot during my PhDs. The warmth in your welcome always remains the same even in the coldest situation and that gave me belief that next time it will be all right. Thanks a lot to you two for being my paranymphs.

From January 2017, I have started working in DENS Solutions as an application scientist. I like to thank Ben Borman for giving me this wonderful opportunity to work with the amazing team - Qiang, Eric, Sander, Marina, Hugo, Gin, Ronald, RJ, Rene, Diederik, Mariya, Jeff, Merijn, Ton, Tijn, Martijn, I would like to thank each of you for your help.

Staying in Netherlands will not be pleasant without being surrounded by friends. Sairam, you are the first person I met in Netherlands. Even though you didn't knew me you were there in the Airport to pick me up. Not only that you had arranged for the SIM card and dinner for me. That was the beginning of our friendship. After that no matter whether it was a discussion regarding the experiment, problem related TEM, some occasion at home, any kind of

problem, small or big, you were always there for me. No matter how hard I try I can't thank you enough. I wish you are here during my PhD defence but I am very happy that you have started your professional carrier in IIT Hyderabad. I also like to thank Padma, for taking best care of you. You two make a great couple. I wish you all the very best in life. I am fortunate great a friend circle and especially friends like Kollol, Chayan, Anirban, Koel, Girish, Venkatesh (Seshan), Ankit, Bedashrita (Beda), Ananya (Any), Anirban (kaka), Amit, Chandra. Our trips, weekend parties gave me enough oxygen to finish my PhD. Thank you each and one of you to be there for me at all times. Thanks to the affectionate and welcoming families of Tandradi and Bimanda; Prangadi and Biswada for all those wonderful evenings. I would also like to thank all my friends and relatives back in India for all their support throughout. Especially I like to thank Shantanu-da, who is also an adjunct Professor in TUDelft, for recommending me to start my PhD at TUDelft.

I am glad to have such nice brother-in-law (Sourav), who also helped me in designing the thesis cover, brother-in-law's wife (Pom) and their loving baby (Nemo); mother- and father-in-laws. Thank you very much for your support. My PhD journey was not a smooth ride; I have lost two dearest persons in this world. Baba, I wish you are here beside me. Ariyan, you would have been almost 3 years by now. My heart will remain empty forever without you two. But I know, wherever you are, you will be happy that I am finishing my PhD. Mamoni, thank you so much for bringing me up the way you did, the sacrifices you made and love you have given me. Sarmila, my loving wife, I don't know how I can thank you. Without you, I couldn't even start my PhD, thank you so much for you support, scarifies and love. I can't finish this thesis without mentioning Parjan (Dhun)-our 7 months old baby. You have already brought so much joy in our life. I am looking forward to our journey together.

I consider myself extremely fortunate to have the company of all the wonderful people mentioned here.

Shibabrata Basak
Delft, March 2017